Summer 8-2020

Extratropical Cyclones and Associated Climate Impacts in the Northeastern United States

Julia Simonson
University of Maine, julia.simonson@maine.edu

EXTRATROPICAL CYCLONES AND ASSOCIATED CLIMATE IMPACTS IN THE NORTHEASTERN UNITED STATES

By

Julia Simonson

B.S. University of North Dakota, 2014

M.S. University of Nebraska-Lincoln, 2016

A DISSERTATION

Submitted in Partial Fulfillment of the

Requirements for the Degree of

Doctor of Philosophy

(in Earth and Climate Sciences)

The Graduate School

The University of Maine

August 2020

Advisory Committee:

Sean D. Birkel, Research Assistant Professor of Earth and Climate Sciences, Climate Change Institute, Advisor

Kirk A. Maasch, Professor of Earth and Climate Sciences, Climate Change Institute

Paul A. Mayewski, Professor of Earth and Climate Sciences, Climate Change Institute (Director)

Bradfield Lyon, Associate Research Professor of Earth and Climate Sciences, Climate Change Institute

Andrew M. Carleton, Professor of Geography, Pennsylvania State University

EXTRATROPICAL CYCLONES AND ASSOCIATED CLIMATE IMPACTS IN THE NORTHEASTERN UNITED STATES

By Julia Simonson

Dissertation Advisor: Dr. Sean D. Birkel

An Abstract of the Dissertation Presented
in Partial Fulfillment of the Requirements for the
Degree of Doctor of Philosophy
(in Earth and Climate Sciences)
August 2020

There is growing concern that some aspects of severe weather could become more frequent and extreme across the northeastern United States (USNE) as a consequence of climate change. Extratropical cyclones and frontal systems are a common factor in a variety of severe weather hazards in the region. This dissertation examines three types of meteorological events impacting the USNE – ice storms, heavy rainfall, and high-wind events. The first research topic utilizes the Weather Research and Forecasting (WRF) model in a case study of the December 2013 New England ice storm. In this analysis, a series of tests are conducted to examine how choice of planetary boundary layer physics and other factors affect the model skill in comparison to observations. The results show that near-surface variables are highly sensitive to model setup, highlighting the need for careful testing prior to use. The second research topic explores large-scale teleconnections associated with the documented increase in summer precipitation across the USNE over the past two decades. It is shown that the precipitation surplus occurs in likely teleconnection with increased frequency of high pressure blocking over Greenland. As the current generation of climate models do not correctly depict seasonal patterns or trends in precipitation for the USNE, identifying the association between Greenland blocking and recent precipitation changes across the USNE is crucial for understanding the shortcomings

for climate projections for the region. The third research topic is an analysis of the frequency and intensity of mid-autumn wind storms in New England. Fall season storms can have dominant cold-season characteristics, while also being fueled by warm-season moisture sources or the result of an extratropical transition. While the results show an increase in storm total precipitation, there are no significant trends in overall wind storm frequency or intensity with respect to central pressure or surface wind speeds. Nevertheless, storm severity is only one factor that contributes to damage from high wind events. As a whole, this dissertation provides insights to how precipitation and storms are changing across the USNE, while highlighting some of the challenges of weather and climate prediction at regional scales.

ACKNOWLEDGEMENTS

This research is supported by a University of Maine Signature and Emerging Area of Excellence Graduate Fellowship to the Climate Change Institute. High-performance computing support from Cheyenne and Yellowstone was provided by NCAR's Computational and Information Systems Laboratory, sponsored by the National Science Foundation.

TABLE OF CONTENTS

LIST OF TABLES

LIST OF FIGURES

CHAPTER 1

INTRODUCTION

In the northeastern United States (USNE), extratropical cyclones and their associated fronts are responsible for a wide range of weather-related hazards. They are the most common cause of extreme precipitation (Agel et al., 2019, 2018, 2015; Dowdy and Catto, 2017; Kunkel et al., 2012), as well as high-wind events (Ashley and Black, 2008; Booth et al., 2015). During the cold season, extratropical cyclones (particularly coastal storms, or "nor'easters") bring precipitation in the form of rain, freezing rain, sleet, and snow, and can undergo rapid intensification. The effects of these severe weather events can range from short term (risk to life, infrastructure damage, disruption of commerce) to long term (shifts in forest composition following an ice storm or high-wind event). There is considerable uncertainty in how extratropical cyclones and the consequences of extreme precipitation events will change in a warming world.

This dissertation explores three meteorological events associated with extratropical cyclones that have climatic implications for the USNE – ice storms, heavy rainfall, and high-wind events. These research topics were chosen due to their applicability to weather and climate forecasting techniques, as well as their relevance to civilian, industrial, and legislative stakeholders in the USNE. This dissertation is organized into five chapters as follows, where Chapters 2–4 are formatted as research papers for peer-review publication.

Chapter 2 is an assessment of the sensitivity of a commonly used numerical weather prediction (NWP) model, the Weather Research and Forecasting (WRF) model, to various setup configurations for an ice storm case study. In an attempt to improve storm response and minimize costs, energy companies have supported the development of ice accretion forecasting techniques utilizing meteorological output from NWP models. However, analyses of modeled case study storms tend to provide little verification of output fidelity (e.g., Musilek et al., 2009; Pytlak et al., 2010; Zarnani et al., 2012. As the classification of

freezing rain and sleet is highly sensitive to NWP model uncertainty, it is important to verify the accuracy of model output against observations. The primary goal of this chapter is to provide further insight into the sensitivity of NWP model output, which could adversely affect the development of ice accretion forecasting systems if model-based biases are not sufficiently minimized.

Chapter 3 explores the contribution of shifts in large-scale circulation across the North Atlantic to recent increases in summer extreme precipitation over the USNE. While previous work has discussed the contribution to increased extreme precipitation from tropical cyclones since the early 2000s (Howarth et al., 2019; Huang et al., 2018), the large-scale driver of summer precipitation increases in the extra-tropics has received little attention. It is proposed that increased incidence of high latitude blocking over Greenland and the subsequent shifts in the upper-tropospheric wave pattern over the North Atlantic promotes increased southwesterly moisture transport into the Northeast, resulting in more heavy rainfall events. Clarifying the teleconnection between Greenland blocking and recent precipitation changes across the USNE may help to explicate the limitations of climate projections of summer season rainfall for the latter region, as climate models are currently unable to reproduce the observed tendency towards increased atmospheric blocking over Greenland.

Chapter 4 examines the frequency and intensity of mid-autumn wind storms (high-wind events associated with extratropical cyclones) across New England. In recent years, New England has seen a number of wind storms that have produced extensive infrastructure damage, raising concerns that these events may become more common in a changing climate. Storms developing during this time of year are unique in that they can have dominant cold-season characteristics, while also being fueled by warm-season moisture sources (such as the remnants of tropical cyclones) or the result of a tropical cyclone undergoing extratropical transition. In providing insights on the behavior of such storms,

we can better evaluate how climate change could impact the risk of damage from wind storms.

In Chapter 5, the main findings and contributions of this work are summarized.

CHAPTER 2

WRF SIMULATION, MODEL SENSITIVITY, AND ANALYSIS OF THE DECEMBER 2013 NEW ENGLAND ICE STORM

2.1 Chapter Introduction

While harsh winters are common in northern New England, damaging ice storms that impart significant cost to civil infrastructure and the regional economy are relatively rare. The most impactful ice storm in the region in recent history occurred 5-10 January 1998, resulting in over $1.4 billion in damage in the U.S. and southeastern Canada (Lott and Ross, 2006). Another significant ice storm swept across the region on 21-23 December 2013. This more recent ice event was less severe than its 1998 counterpart, but nonetheless imparted costly damage to the regional electric grid: storm damage exceeded $1.9 million in Maine (Brogan, 2014) and nearly $6.5 million in Vermont (NOAA/NCEI, 2014). The potential for extensive infrastructure damage, and uncertainty related to how climate change will affect the frequency and intensity of ice storms, warrants close inspection of how well numerical forecast models are able to depict and predict these events.

Most ice storm case studies focus primarily on the development of ice accretion modeling and forecasting methods. In these existing studies, forecast or reanalysis output is downscaled using a numerical weather prediction model (NWP), such as the Weather Research and Forecasting (WRF) model (Skamarock et al., 2008), which provides meteorological input for an ice accretion model. This approach has been utilized for predicting ice accretion on power lines (Arnold, 2009; DeGaetano et al., 2008; Hosek et al., 2011; Musilek et al., 2009; Pytlak et al., 2010; Pytlak, 2012; Zarnani et al., 2012), as well as in-cloud icing on wind turbines (Davis et al., 2013) and on other ground based structures in mountainous terrain (Nygaard et al., 2011). Outside of energy production and distribution industries, WRF has also been utilized to examine the role of sea surface

temperatures in the Gulf of Mexico on ice-storm severity in the U.S. southern Great Plains (Mullens et al., 2016).

Despite the ubiquitous application of WRF for developing and validating ice forecasting systems, relatively few ice storm case studies are found in the literature compared to other modeled weather events. Those that are available concentrate on the ice forecast component, with limited consideration for the realism of the driving atmospheric model. Documentation of WRF output validation for ice storm case studies, if included at all, is generally restricted to spatially and temporally averaged statistical analyses of surface variables, as in Musilek et al. (2009) and Pytlak et al. (2010). Sensitivity tests are not typically reported, except with regards to ice-accretion modeling applications for a select number of physics parameterizations. For example, Nygaard et al. (2011) compared the performance of three cloud microphysics parameterization schemes for predicting supercooled cloud liquid water content and diagnosing median volume droplet diameter, two necessary input variables for ice accretion models. Eight WRF simulations centered on Mount Ylläs in northern Finland were evaluated using twice daily soundings from a meteorological observatory located 100 km east of the mountain. Modeled sounding profiles were considered representative of the atmospheric conditions during the simulations, with the overall mean absolute error of modeled temperatures at 1.6°C. However, in one instance where WRF was unable to resolve a strong surface-based temperature inversion, modeled surface temperatures were overestimated by 5°C. Davis et al. (2013) also produced an icing study with sensitivity tests, wherein WRF was used to provide meteorological conditions at a Swedish wind farm for a wind turbine ice accumulation model. The sensitivity tests included three planetary boundary layer (PBL) schemes and three cloud microphysics schemes. General model performance was validated against 2-meter temperature and 10-meter wind speed observations from three surface stations, as well as temperature and wind speed observations at 80 meters at the wind farm. It was noted that while observed and modeled temperatures at the wind farm were

in good agreement for temperatures above 0.5°C, large cold biases occurred when simulated temperatures were below freezing. The largest deviations in temperature occurred below -10°C, although this would not have a large impact on the ice model due to the particles freezing before contact with the turbine blades. These two studies provide more robust descriptions of model performance compared to other ice model studies, but nevertheless the evaluation of WRF output is brief and secondary to the desired model application.

This lack of model validation is in stark contrast to operational weather forecasting centered icing studies. Ikeda et al. (2013, 2017) used surface and sounding observations to assess the High-Resolution Rapid Refresh (HRRR) model in identifying surface precipitation phase for several case study ice storms effecting the central and eastern US. The HRRR is an operational NWP model that is built upon the WRF model and includes a postprocessing routine that identifies the type of precipitation at the surface. The authors found that the size and organization of weather systems is a factor in the forecast skill for precipitation extent and phase, with greater skill for larger, more organized systems compared to smaller events. For most events, the simulated near-surface temperatures had biases of less than 2°C, while several smaller events associated with cold-air damming on the eastern size of the Appalachian Mountains either did not have a subfreezing surface layer, or exhibited significant warm biases of up to 4°C within the layer. Overall, the study found that simulated locations and spatial extents of freezing rain were reasonable, but not nearly as robust as simulated depictions of rain and snow.

The sparse documentation on relevant WRF performance and sensitivity presents challenges for those interested in simulating ice storms with the greatest accuracy possible. Conditions are conducive for freezing rain when the atmosphere is highly stratified: a warm (above freezing) and moisture-laden air mass overruns a colder, subfreezing surface layer of air. Previous studies have determined that precipitation type is largely dependent on the maximum temperature of the warm layer, which is proportional to layer depth (Stewart and King, 1987; Zerr, 1997). Warm layers with maximum temperatures > 3°C allow for

complete melting of snowflakes that fall through the layer, while lower temperatures allow partial or very little melting. The depth of the cold layer, which usually only extends 300-1200 m above the surface (Young, 1978), is also crucial. Underestimating the depth of the cold layer would result in rain that would not freeze on contact, while overestimating the depth could result in the identification of sleet or ice pellets, as the rain refreezes before reaching the ground (Forbes et al., 1987). Considering that changes in temperature as low as 0.5°C can alter precipitation type (Reeves et al., 2014; Thériault et al., 2010), sensitivity testing is a crucial first step when using NWP models for research and development purposes in order to minimize the contribution of model-based uncertainty to icing forecasts.

This study reports a suite of WRF sensitivity experiments designed to investigate the variability of model output to model configuration for the specific case of the December 2013 New England ice storm. The experiments test the impact of a variety of configuration options including the choice of PBL physics parameterization, reanalysis forcing, use of grid nudging, and the number of vertical levels. For lateral boundary forcing we utilize the reanalysis models ECMWF ERA-Interim, ECMWF ERA5, and the NCEP North American Regional Reanalysis. Because ice accretion models utilize simulated values of air temperature, precipitation rate, and wind speed, we validate these simulated variables against surface and radiosonde observations. The tests reported here provide further insight into the sensitivity of WRF output to changes in model setup, thus providing general guidance for future WRF-based numerical simulations of ice storms.

This paper is structured as follows. The December 2013 New England ice storm is summarized in Section 2.2, with the data and model setup used described in Section 2.3. The results are described and discussed in Sections 2.4 and 2.5. A summary of our major conclusions is presented in Section 2.6.

2.2 December 2013 New England Ice Storm Case Study

The December 2013 New England ice storm was part of a larger storm system that brought freezing rain and heavy snow to the Midwest and Northeast, and tornadoes in the Southeast U.S. from 19 December through 23 December (NCDC, 2014). This storm exhibited many of the same large-scale features present in the 1998 ice storm, as detailed by Gyakum and Roebber (2001) and Roebber and Gyakum (2003): a cold anticyclone in Canada, an anticyclone in the southwestern North Atlantic, and an inverted trough stretching from the Gulf of Mexico towards the Great Lakes (Fig. 2.1). A quasai-stationary front extended from east Texas through the Ohio Valley into New England, parallel to the southwesterly flow aloft. The air mass ahead of the front was unseasonably warm and moist for the time of year, with precipitable water values greater than 30 mm and a temperature gradient of more than 25°F (14°C) across the front. Strong low-level convergence and frontogenetic forcing ahead of a surface low resulted in heavy rain and tornadoes ahead of the front during 21 and 22 December, while behind the front fell heavy snow and freezing rain. Ice storm warning criteria ($>$ 0.25 in ice accumulation) were met for counties in Texas, Oklahoma, Kansas, Iowa, Illinois, Michigan, New York, Vermont, and Maine during the storm.

In northern New York and New England, precipitation developed in two separate waves, with the location of the quasi-stationary front a key factor in the type of precipitation (Fig. 2.2). The first wave of precipitation lasted from approximately 1200 UTC 21 December until 1800 UTC 22 December. At this time, the front was largely stationary over northern New York, Vermont, and New Hampshire through the southeastern (or "Downeast") coast of Maine, running parallel to the southwestern flow aloft. The front was partially obscured due to topographical features, with southwesterly flow over the White Mountains of New Hampshire and northeasterly flow to the east of the Longfellow Mountains in Maine. Several weak areas of low pressure tracked along the stationary front, with precipitation falling as rain over the Adirondacks and the White Mountains, freezing rain to the

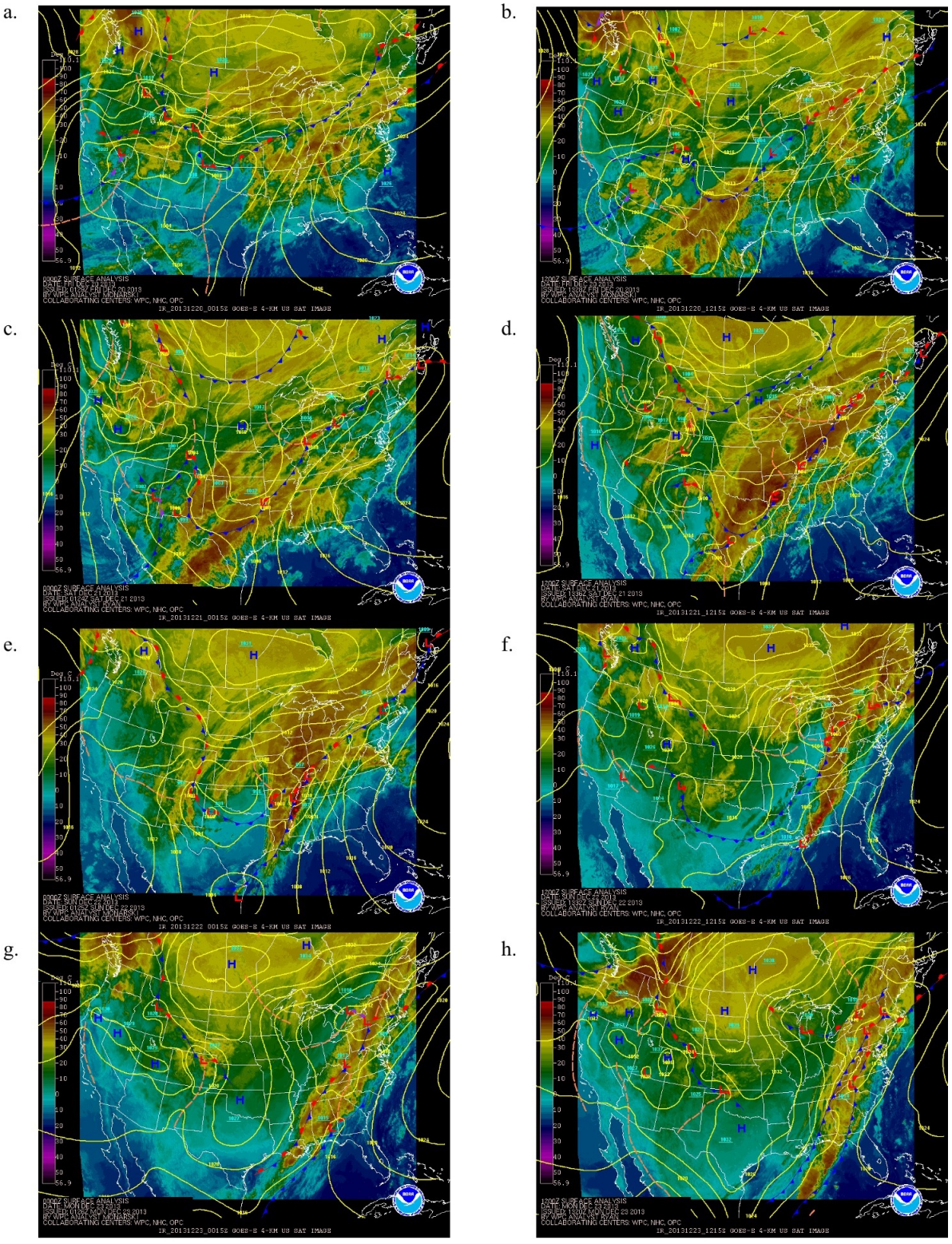

Figure 2.1: Surface analysis/infrared satellite composites for 0000 UTC (a) 20, (c) 21, (e) 22, and (g) 23 Dec 2013 and 1200 UTC (b) 20, (d) 21, (f) 22, and (h) 23 Dec 2013 from NOAA (2018).

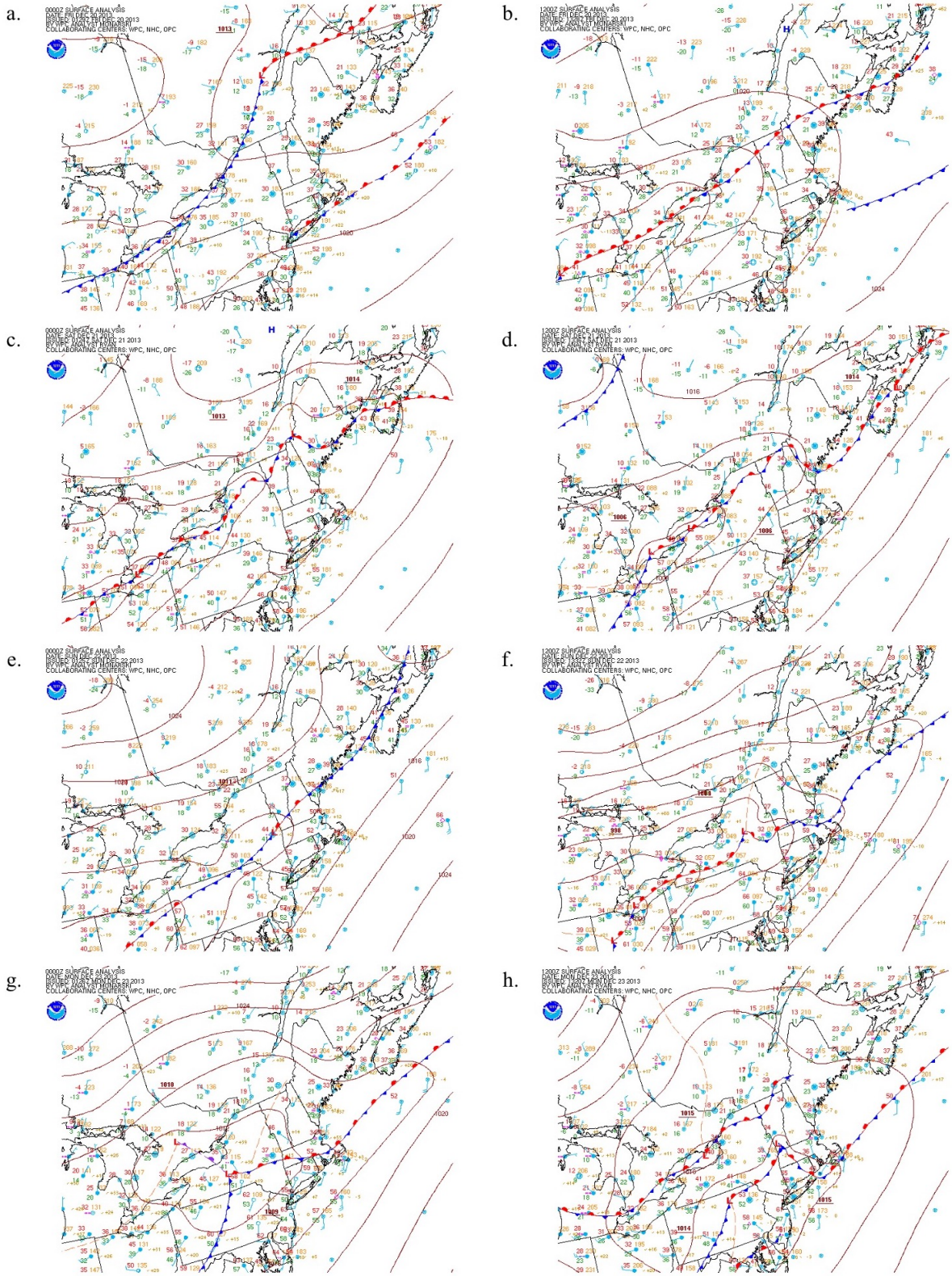

Figure 2.2: Regional surface analyses same as Fig. 2.1.

southeastern St Lawrence Valley and the northern Champlain Valley as well as Downeast Maine, mixing with sleet into central Maine and transitioning to snow to the north. The heaviest precipitation accumulations occurred during the latter half of this period, coinciding with a period of strong frontogenesis aloft ahead of the approach of a stronger low pressure system (Fig. 2.3a). The second wave of precipitation lasted from approximately 0000 UTC 23 December to 0000 UTC 24 December, during which the front drifted southward over eastern Massachusetts and Rhode Island and the low tracked across the Gulf of Maine. High temperatures on the 23rd range from -9°C (16°F) along the U.S-Canadian border to near 20°C (68°F) in parts of southern New England. This system brought rainfall to southern New England and additional freezing rain to the Downeast coast associated with moderate frontogenetic forcing aloft (Fig. 2.3b). Storm total ice accumulations as high as 32 mm (1.25 in) were reported in New York and Vermont and 25 mm (1.0 in) in Maine (Fig. 2.4). More than 75,000 customers in Vermont and 170,000 in Maine, as well as 66,000 in New York, lost electric service as a result of wire icing and downed trees, in some places for more than a week (NCDC, 2014; NOAA/NCEI, 2014). Recovery efforts were hampered by extended extreme cold conditions and subsequent winter storms in the weeks following the ice storm, resulting in additional power outages.

2.3 Data and Model Setup

Simulations of the December 2013 New England ice storm were conducted using WRF version 3.9. Two one-way nested domains were used with grid spacings of 9 km and 3 km (Fig. 2.5). The simulations were initialized at 0000 UTC 20 December 2013 and ended at 0000 UTC 25 December 2013, with the first 24 hours used for model spinup. The model top was set to 50 hPa. Base physics options used for all sensitivity tests included the WRF single-moment 6-class microphysics scheme (Hong and Lim, 2006), the Rapid Radiative Transfer Model for general circulation models (RRTMG) longwave radiation scheme (Iacono et al., 2008), the Goddard shortwave radiation scheme (Chou and Suarez, 1999),

a.

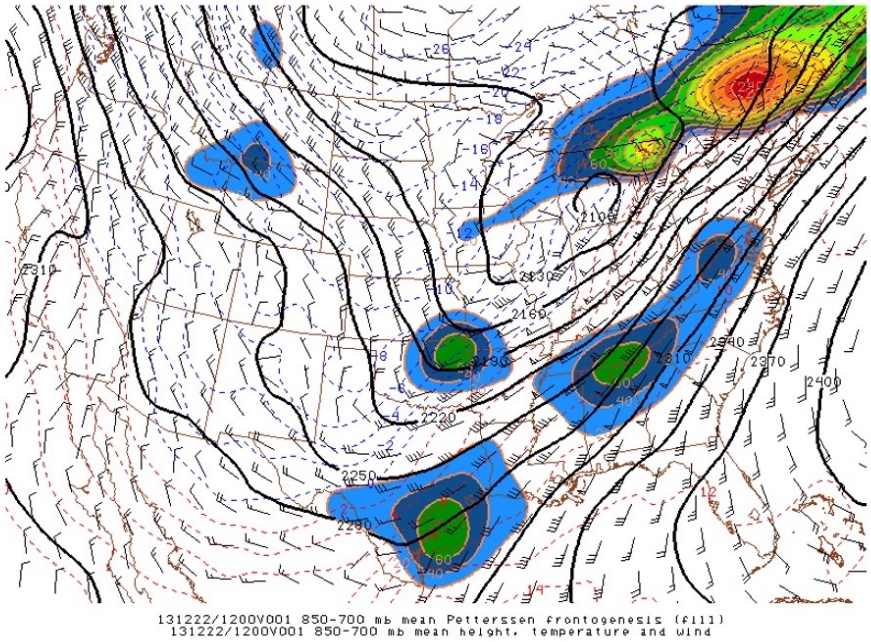

b.

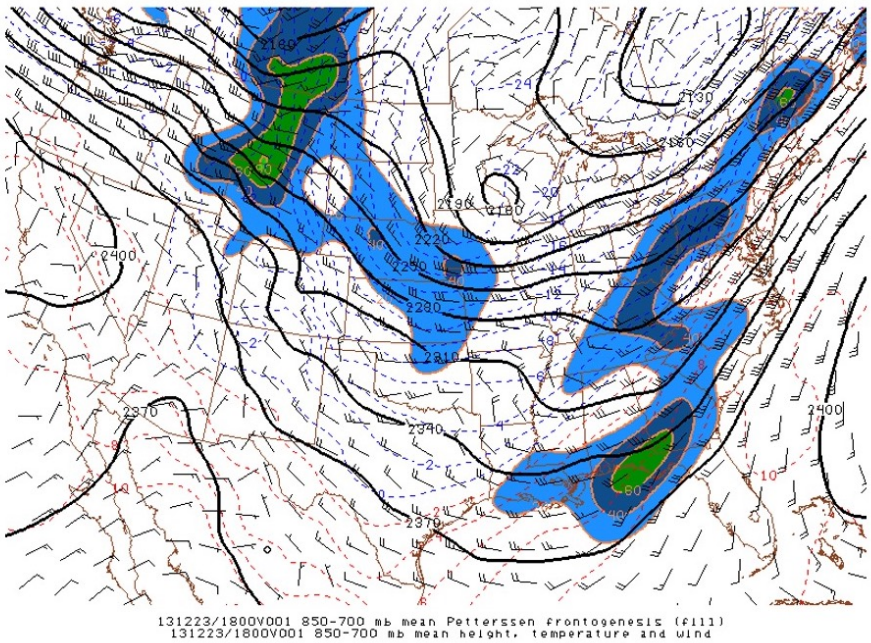

Figure 2.3: Mesoscale analysis of 850-700 hPa mean Petterssen frontogenesis, mean height, temperature, and wind for (a) 1200 UTC 22 Dec and (b) 1800 UTC 23 Dec from NOAA (2019a).

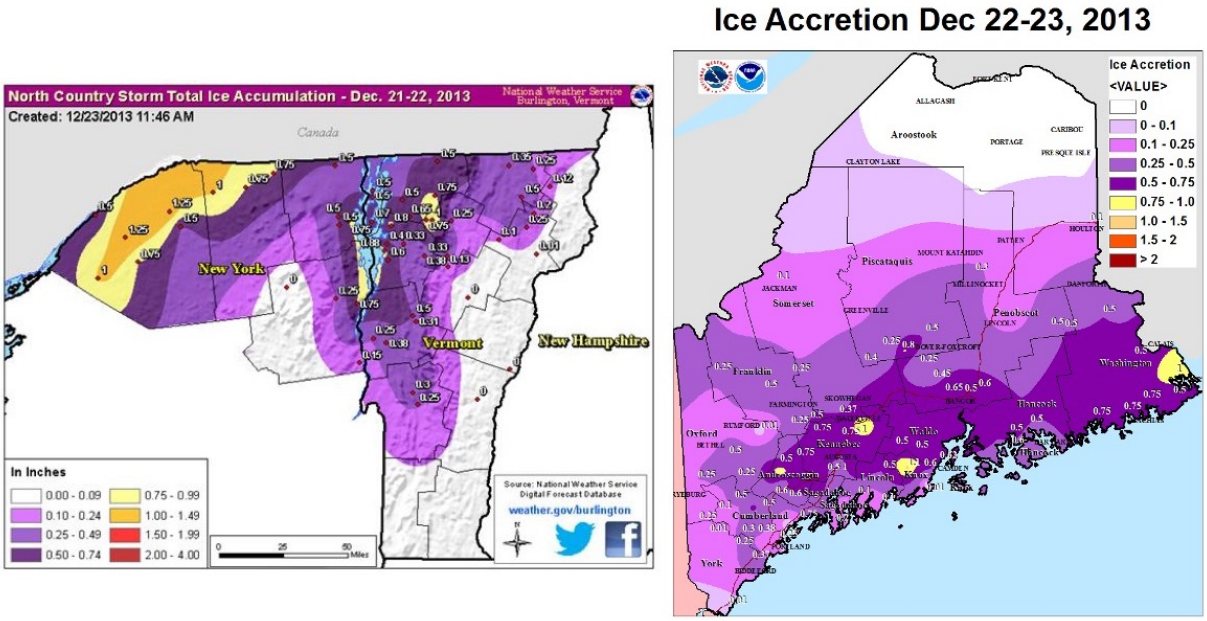

Figure 2.4: Storm total ice accumulation maps from (left) Taber (2015) and (right) NOAA (2019b).

the Kain-Fritsch cumulus scheme (Kain, 2004) for the outer domain, and the Noah land surface model (Tewari et al., 2004). Preliminary simulations were run on the NCAR Yellowstone (Computational And Information Systems Laboratory, 2016) supercomputer using 64 cores prior to its decommissioning. All sensitivity simulations reported here were conducted on the NCAR Cheyenne (Computational And Information Systems Laboratory, 2017) supercomputer using 72 cores.

The model sensitivity tests consist of two groups with the configurations listed in Table 2.1. The first experiment group tests the WRF model sensitivity to choice of PBL scheme and the respective surface layer. We tested eight WRF PBL schemes, of which five of the eight PBL schemes utilize the Eta (Janić, 2001) and Revised MM5 (Jiménez et al., 2011) surface layer schemes, while the remaining PBL schemes were paired with their respective surface layer scheme. The two main components in which the schemes differ are in the order of closure and the extent of vertical mixing. The YSU and ACM2 schemes are first order closure schemes, in which higher order terms in the decomposed equations of motion are represented in terms of the mean. The remaining PBL schemes are 1.5 order, which

Table 2.1: Summary of model simulations used in this study.

Short Name	Reanalysis	PBL Scheme	Surface Layer	Nudging (Y/N)	Vertical Levels
YSU	ERAI	Yonsei University	Revised MM5 Similarity	Y	36
ACM2	ERAI	Asymmetric Convective Model Version 2	Revised MM5 Similarity	Y	36
MYJ	ERAI	Mellor-Yamada-Janjic	Eta Similarity	Y	36
QNSE	ERAI	Quasi-Normal Scale Elimination	QNSE	Y	36
MYNN2	ERAI	Mellor-Yamada-Nakanishi-Niino Level 2.5	MYNN	Y	36
BouLac	ERAI	Bougeault-Lacarrere	Revised MM5 Similarity	Y	36
UW	ERAI	University of Washington	Revised MM5 Similarity	Y	36
TEMF	ERAI	Total Energy-Mass Flux	TEMF	Y	36
ERAI 36	ERAI	Mellor-Yamada-Janjic	Eta Similarity	N	36
ERAI 46N	ERAI	Mellor-Yamada-Janjic	Eta Similarity	Y	46
ERAI 46	ERAI	Mellor-Yamada-Janjic	Eta Similarity	N	46
ERA5 36N	ERA5	Mellor-Yamada-Janjic	Eta Similarity	Y	36
ERA5 36	ERA5	Mellor-Yamada-Janjic	Eta Similarity	N	36
NARR 36N	NARR	Mellor-Yamada-Janjic	Eta Similarity	Y	36
NARR 36	NARR	Mellor-Yamada-Janjic	Eta Similarity	N	36

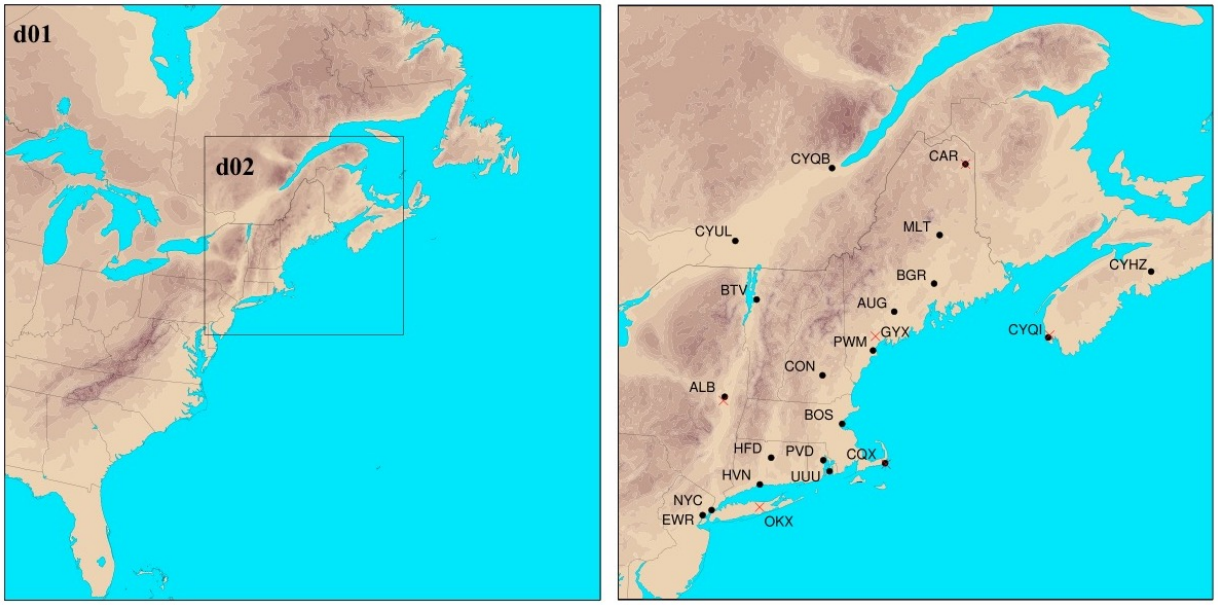

Figure 2.5: WRF model domains (left) and locations of ASOS and radiosonde stations (right). Surface stations include Albany, NY (ALB), Augusta, ME (AUG), Bangor, ME (BGR), Boston, MA (BOS), Burlington, VT (BTV), Caribou, ME (CAR), Concord, NH (CON), Chatham, MA (CQX), Newark, NJ (EWR), Hartford, CT (HFD), New Haven, CT (HVN), Millinocket, ME (MLT), New York City, NY, (NYC), Providence, RI (PVD), Portland, ME (PWM), Newport, RI (UUU), Halifax, NS (CYHZ), Quebec City, QC (CYQB), Yarmouth, NS (CYQI), and Montreal, QC (CYUL). Sounding stations include Gray, ME (GYX) and Brookhaven, NY (OKX), as well as sites collocated with the Albany, Caribou, Chatham, and Yarmouth surface stations.

predict higher order variables such as turbulent kinetic energy (TKE) by diagnosing second order (variance) moments for specific variables. Local mixing schemes allow only adjacent levels to influence variables at a given location, while non-local schemes include multiple levels. Most of the tested PBL schemes use local mixing, with two hybrid schemes (ACM2 and TEMF) utilizing either non-local or local mixing depending on the atmospheric stability, and YSU as the sole nonlocal scheme. PBL schemes also differ in relation to specific formulations, such as the incorporation of countergradient correction terms. More detailed descriptions of the PBL schemes tested in this study are found in Cohen et al. (2015) and Banks et al. (2016). For these simulations, initial and boundary conditions were supplied by the ERA-Interim reanalysis (ERAI; Dee et al., 2011) obtained from the NCAR Research Data Archive (ECMWF, 2009), grid nudging (Stauffer and Seaman, 1994) was

applied to all levels for the outer domain with the nudging coefficients set to 3 x 10^{-4}, and 36 vertical levels were utilized.

The second experiment group tests the WRF model sensitivity to choice of several setup options using the MYJ PBL simulation as the "control". Three simulations test the use of grid nudging and the number of vertical levels. The lowest eta levels for the simulations using 36 vertical levels are 1.0, 0.993, 0.983, 0.97, 0.954, 0.934, 0.909, 0.880, 0.842, and 0.804, and the lowest eta levels for the simulations using 46 vertical levels are 1.0, 0.998, 0.995, 0.993, 0.988, 0.984, 0.98, 0.975, 0.97, 0.962, 0.954, 0.944, 0.934, 0.922, 0.909, 0.895, 0.88, 0.861, 0.842, and 0.804. Four simulations were run using the North American Regional Reanalysis (NARR; Mesinger et al., 2006) and ERA5 (Hersbach et al., 2020) datasets from the NCAR Research Data Archive (ECMWF, 2017; NCEP, 2005), both with and without grid nudging. Compared to ERAI, a global reanalysis dataset available at 6 hourly intervals with 80 km grid spacing and 60 vertical levels, NARR has both a higher horizontal and temporal resolution (32 km and 3 hour, respectively), but fewer model levels (45). ERA5, the successor of ERAI, is a fifth-generation reanalysis produced by the ECMWF, with 31 km grid spacing, 137 vertical levels, and hourly output fields.

WRF model output was validated against surface station observations and tropospheric sounding data over 21-23 December 2013, when conditions were conducive for freezing rain. Hourly surface observations from 20 Automated Surface Observing System (ASOS) sites were obtained from the Iowa Environmental Mesonet website (https://mesonet.agron.iastate.edu/request/download.phtml), and sounding data were obtained from the NOAA/ESRL Radiosonde Database (https://ruc.noaa.gov/raobs/) for 6 sites (Fig. 2.5). Surface station and sounding sites within and without the ice storm extent were chosen to compare PBL scheme and overall WRF performance for icing and non-icing conditions. The statistical analysis was generally modeled after Musilek et al. (2009) and Pytlak et al. (2010), which included domain-wide metrics of hourly 2-meter temperature and 10-meter wind speed, as well as 6-hour accumulated precipitation. Statistical metrics

from these two studies were used on the innermost domain over 21-23 December and include the mean error (bias), mean absolute error (MAE), and linear correlation coefficient (R). Statistics were also calculated for hourly 10-meter wind direction, as well as values of temperature, wind speed and direction from soundings at 0000 UTC, 0600 UTC (when available), and 1200 UTC. For the sounding variables, the WRF values were interpolated to the mandatory and observed significant levels below 700 hPa. The associated equations are as follow:

$$Bias = \frac{1}{N}\sum_{i=1}^{N}\theta_i$$

$$MAE = \frac{1}{N}\sum_{i=1}^{N}|\theta_i|$$

$$R = \frac{\sum_{i=1}^{N}[(O_i - \overline{O})(M_i - \overline{M})]}{(N-1)(\sigma_O \sigma_M)}$$

where

$$\theta_i = M_i - O_i$$

represents the deviation between the modeled and observed values of a particular variable, θ, with $\overline{M}$ and $\overline{O}$ representing the modeled and observed 3-day averages (respectively), and N is the number of model-observation value pairs. Because wind direction is a circular variable and the absolute deviation cannot exceed 180, the difference between the modeled and observed wind direction is given following Carvalho et al. (2012):

$$\theta_i = (M_i - O_i)(\frac{1-360}{|M_i - O_i|}), if|M_i - O_i| > 180^\circ$$

A positive (negative) bias represents a clockwise (counter-clockwise) deviation in modeled wind direction compared to the observed values. Domain-wide statistics for each PBL scheme simulation include modeled and observed values from all surface or sounding stations. To determine whether the simulations are significantly different from one another, a two-tailed paired t-test (Wilks, 2011) was performed against every variable of each simulation within the two groups. The statistical metrics detailed above, as well as the figures in the following section, were produced using the NCAR Command Language (NCL) version 6.4.0 (NCAR, 2017).

2.4 Results

2.4.1 Assessment of Large-Scale Features

Before validating WRF performance compared to surface observations as in previous ice storm studies, it is crucial to first assess the ability of the model to replicate the large-scale conditions of the storm. This consists of two parts: evaluating the fields provided by the reanalysis used for the "control" simulation (i.e., ERAI) – such as the large-scale circulation as well as the mid- and low-level temperature and moisture fields – then examining how WRF depicts the depth and intensity of the air masses across the front. If ERAI does not sufficiently replicate the broader conditions during the event, then the ability of WRF to resolve local-scale features has to be called into question. Furthermore, understanding how WRF depicts the movement of the warm and cold air masses will lend itself to assessing the model's sensitivity to configuration choices.

At the synoptic scale, ERAI is representative of the atmospheric circulation during the event, including reproducing key surface features such as the highs over Canada and the western Atlantic and the inverted trough. ERAI also reproduces the enhanced surface temperature gradient throughout the southeastern US and the location of the freezing line, as well as ample moisture ahead of the front. The 850 and 925 hPa temperature fields are also consistent between upper air observations and the reanalysis, with the freezing line

and the location of the front parallel to the prevailing southeasterly flow. Equivalent potential temperatures at 850 hPa, the approximate level of maximum temperatures in the warm air mass, of over 287 K (5°C) are present over New England and are reflected in the fields of the outer WRF domain (Fig. 2.6). This temperature configuration in the lower troposphere is characteristic of large scale ice storms, favoring the gradual transition from rain to freezing rain/sleet instead of a direct change over to snow. From this assessment, we conclude that the fields provided by ERAI sufficiently represent the synoptic-scale features of the storm.

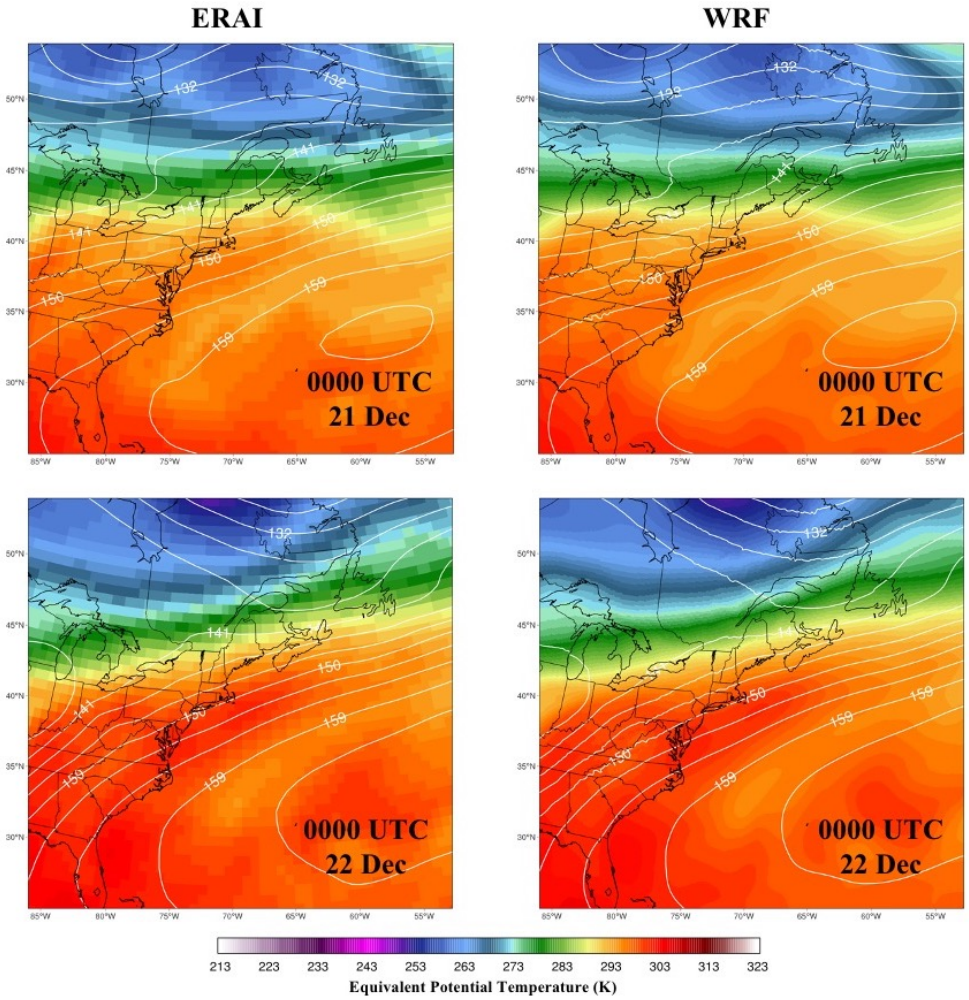

Figure 2.6: Comparison of 850 hPa equivalent potential temperature (K) and geopotential height (dm) contours at 0000 UTC 21 Dec (top) and 0000 UTC 22 Dec (bottom) from ERAI (left) and the WRF outer domain for the MYJ PBL simulation (right).

In the following paragraphs we examine the WRF model representation of critical factors associated with the ice storm, including the depth and intensity of the warm and cold air masses. For this examination we utilize vertical cross sections, oriented roughly perpendicular to the movement of the front, and utilize several sounding stations for verification. The end points of the cross sections are located at the approximate locations of the Caribou and Brookhaven sounding stations. Individual cross section plots in Figure 2.7 and Figure 2.8 are based on the MYJ PBL simulation. In further assessing WRF realism for the ice storm, the modeled 2-meter temperature fields are compared against fields from the Real-Time Mesoscale Analysis (RTMA; NOAA/NCEI, 2019a), a dataset used by forecasters at the National Weather Service for producing and verifying weather forecasts.

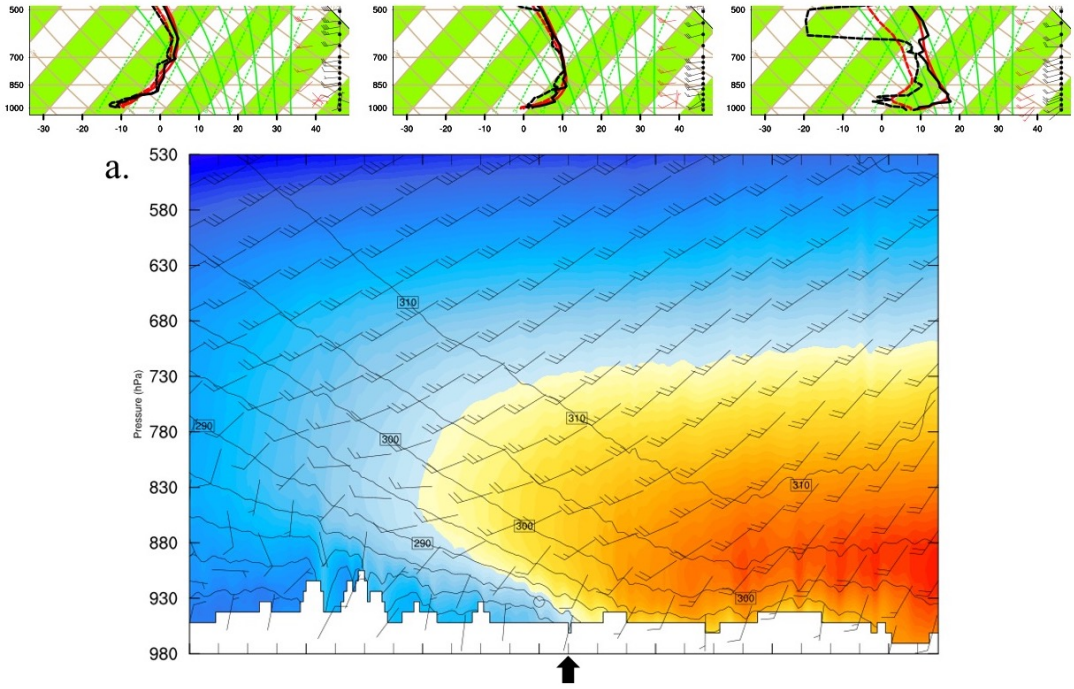

Figure 2.7: Cross sections of temperature (°C), equivalent potential temperature (K), and winds at (a) 0000 UTC and (b) 1200 UTC 21 Dec, and (c) 0000 UTC 22 Dec for the MYJ PBL simulation. Observed (black) and WRF modeled (red) soundings for the Caribou (left), Gray (center), and the Brookhaven (right) stations are above each cross section. The start and end points correspond with the locations of the Caribou and Brookhaven stations, and the approximate location of the Gray station is designated by the black arrow. Temperature profile (solid) is plotted to the right of dewpoint profile (dashed), and winds are in ms^{-1}.

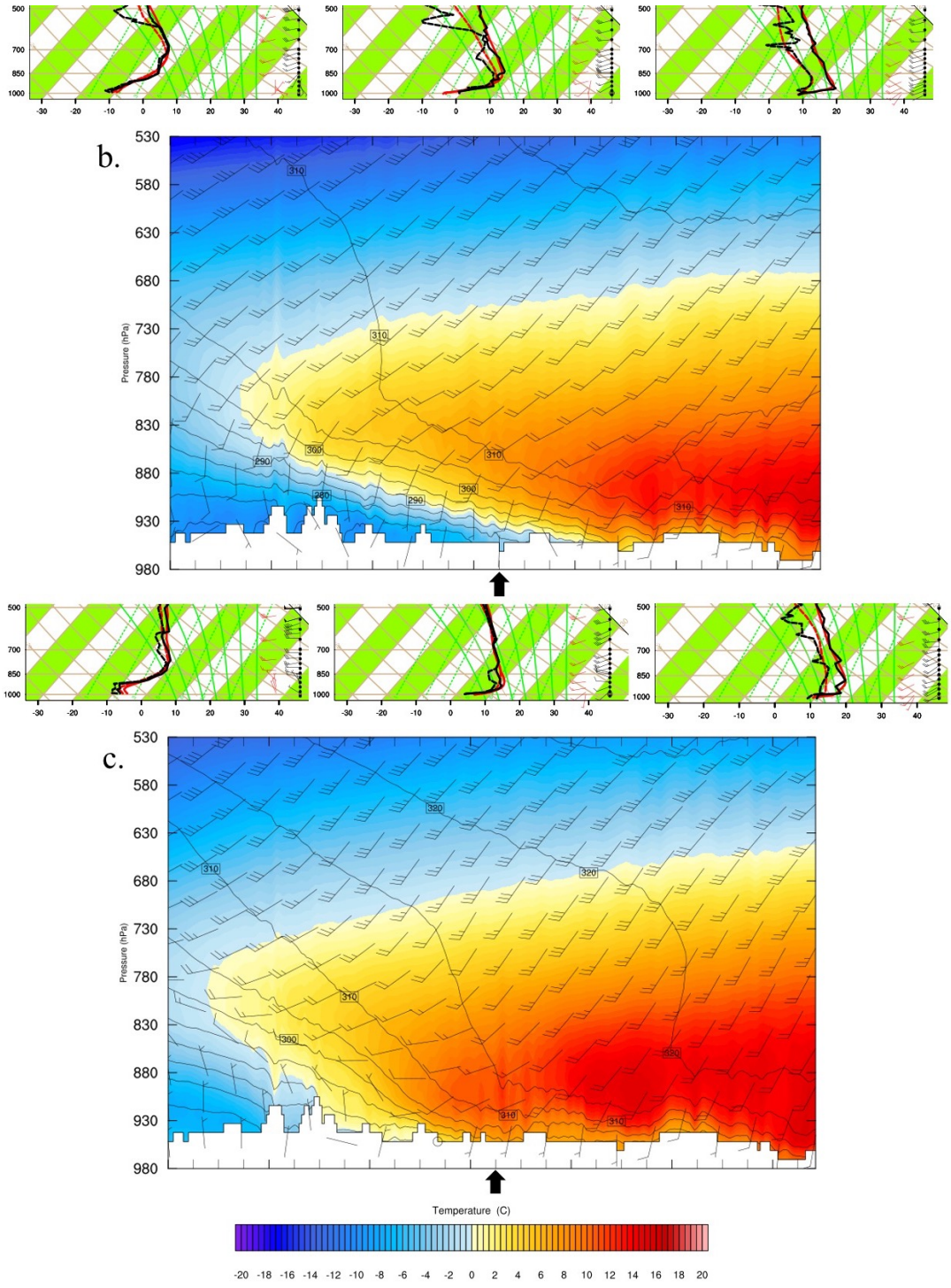

Figure 2.7: Continued.

The December 2013 ice storm can be characterized as two separate episodes, however the time frame differs with that of the two precipitation waves as discussed at the beginning of Section 2.2. The first episode of the ice storm begins around 1800 UTC 20 December with the formation of a wedge of subfreezing air near the surface (Fig. 2.7a). The cold wedge advances southward as warmer air aloft is advected northward (Fig. 2.7b), then from 1200 UTC to 2100 UTC 21 December the cold air retreats northward (Fig. 2.7c). Although minimal precipitation is observed during this period, freezing rain was observed in central Maine. Station observations also note that mist and fog is present throughout Maine and into New Hampshire. The second episode begins as the cold wedge redevelops and quickly intensifies from 2100 UTC 21 December to 1400 UTC 22 December. This period is characterized by enhanced frontogenesis in advance of a low pressure system (Fig. 2.3a) and a steep frontal slope (Fig. 2.8a), followed by a re-invigorated overrunning above the cold air wedge (Fig. 2.8b). The highest hourly rate of precipitation accumulation in northern New England occurs during this time frame (Fig. 2.9a,b). The second wave of

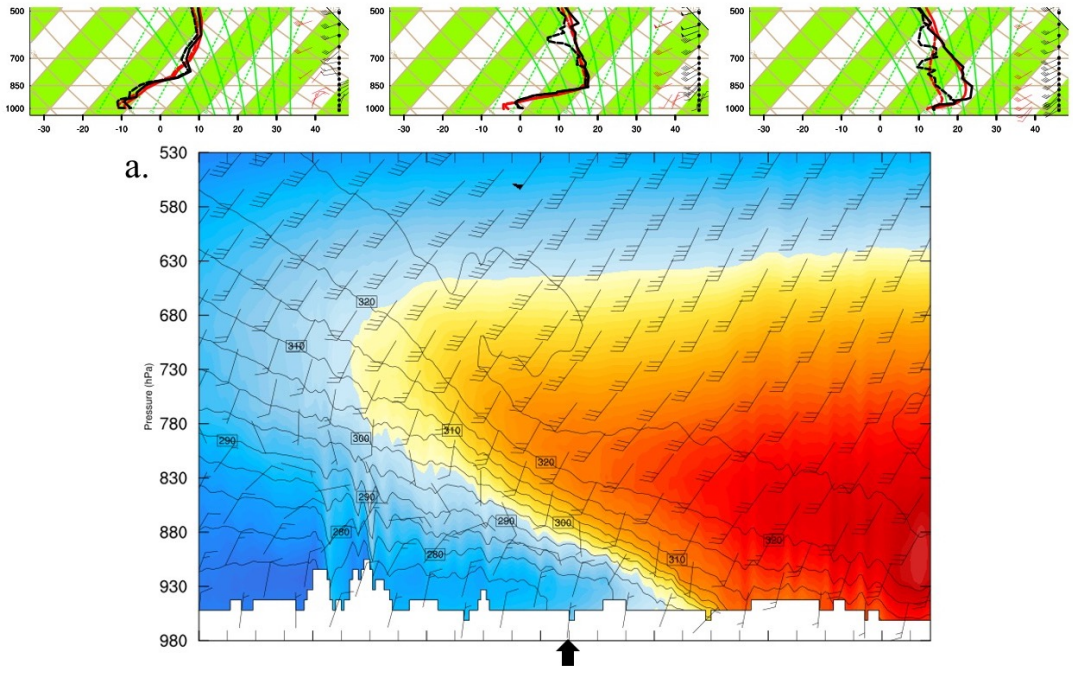

Figure 2.8: As in Fig. 2.7, except cross sections and soundings at (a) 1200 UTC 22 Dec, (b) 0000 UTC and (c) 1200 UTC 23 Dec for the MYJ PBL simulation.

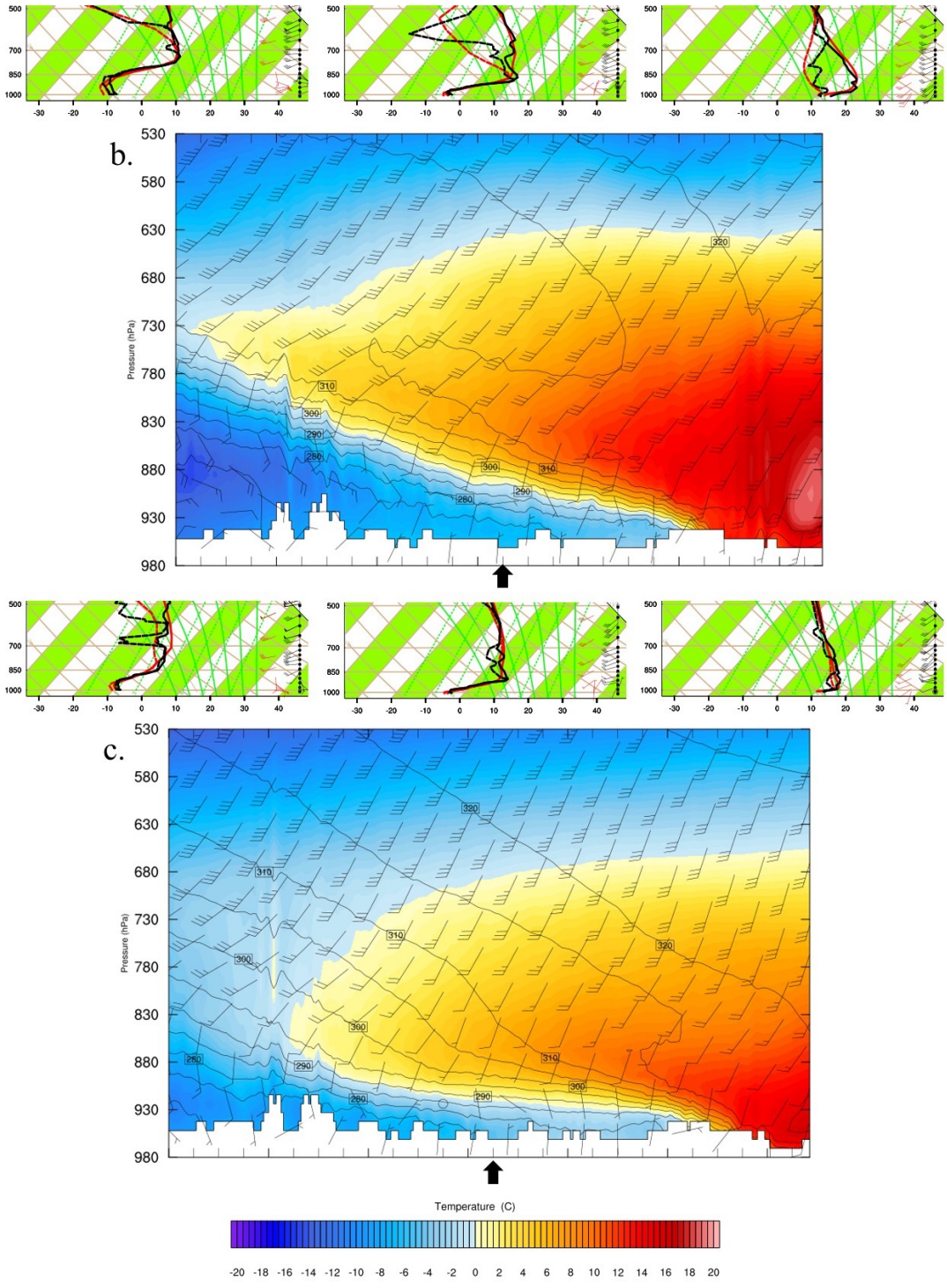

Figure 2.8: Continued.

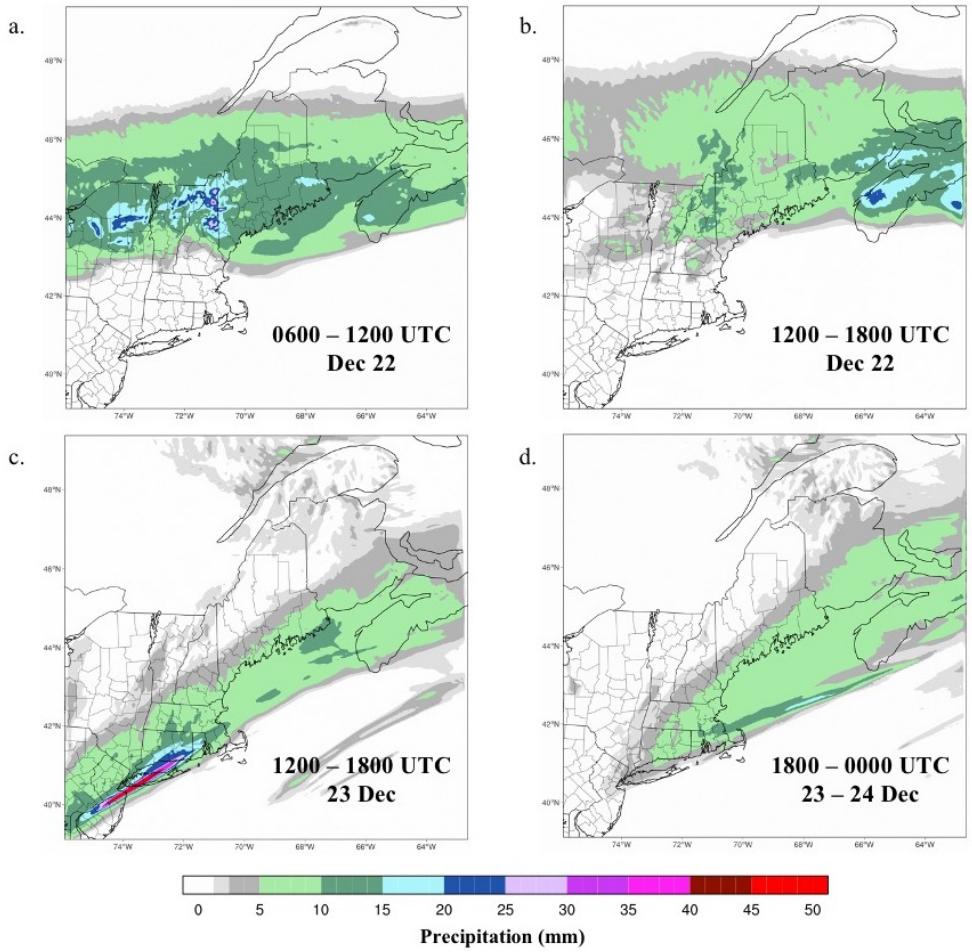

Figure 2.9: Six-hour accumulated precipitation (mm) from (a) 0600 UTC to 1200 UTC, (b) 1200 to 1800 UTC 22 Dec, (c) 1200 UTC to 1800 UTC 23 Dec, and (d) 1800 UTC 23 Dec to 0000 UTC 24 Dec for the MYJ PBL simulation.

precipitation, as shown in Figure 2.9c and 2.9d, occurs as the subfreezing surface layer is thinned (Fig. 2.8c) and ends as surface winds shift to the northwest and temperatures drop below freezing. Reports of freezing rain during this period are concentrated over southern Maine and southeastern New Hampshire.

Overall, WRF is able to sufficiently depict the depth and intensity of the elevated warm layer for the MYJ PBL simulation. Modeled maximum temperatures within the warm air mass are over 4°C in southeastern Maine during the waves of precipitation, which reflect the maximum temperatures of sounding observations. This indicates that temperatures within the warm airmass are sufficient for falling hydrometeors in this layer to melt completely.

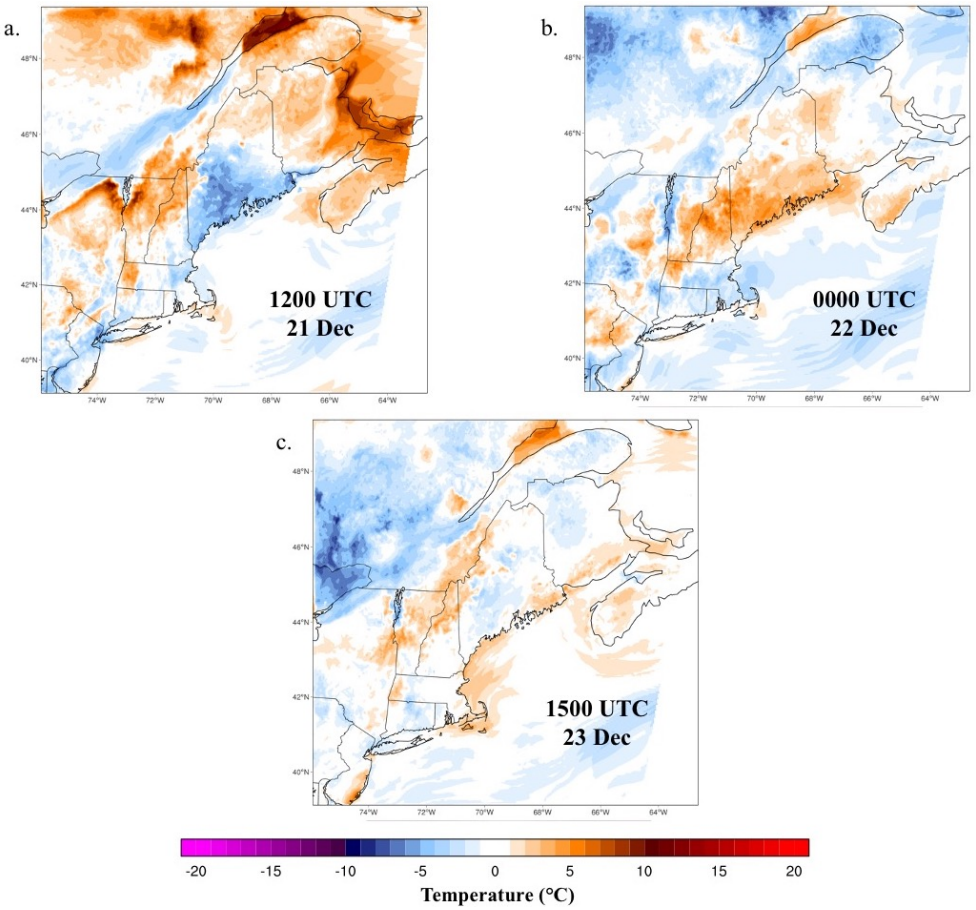

Figure 2.10: Difference in 2-meter temperature (°C) between RTMA and MYJ PBL simulation at (a) 1200 UTC 21 Dec, (b) 0000 UTC 22 Dec, and (c) 1500 UTC 23 Dec.

However, temperature biases near the surface are evident as surface air masses transition in northern New England. Cold biases are prevalent at 0000 and 1200 UTC 21 December and at 1200 UTC 22, while a warm bias is present at 0000 UTC 22 December (Fig. 2.10). Modeled surface temperatures are more consistent with observations for 23 December, as temperature biases are less prevalent than the prior two days. The modeled profiles for the endpoints of the cross section at the Caribou and Brookhaven stations (Fig. 2.7 and Fig. 2.8) are representative of the observed conditions for the duration of the storm.

Based on the cross sections and near-surface temperature maps, the vertical temperature profile and tropospheric winds appear to be well represented overall by WRF. The modeled temperature profiles closely follow observations within the elevated warm

layer, then model performance generally decreases downward, with the largest temperature departures at or just above the surface.

2.4.2 Sensitivity to PBL Scheme

In this section we assess the sensitivity of the model to the chosen PBL scheme. This is done through comparing domain-wide statistical analyses as used by previous ice storm modeling studies and investigating the spatial and temporal variability of PBL performance using surface time series, soundings, and cross sections.

The results of the 3-day domain-wide sensitivity analysis of modeled 2-meter temperature, 10-meter wind speed and direction, and 6-hour precipitation are shown in Table 2.2 and sounding error statistics for the surface to 700 hPa in Table 2.3. Overall, the bias metric indicates that the model tends to overestimate wind speed (at the surface and up to 700 hPa) and precipitation, while near-surface temperature was generally underestimated in five of the eight PBL simulations and overestimated above the surface for all. The variability in MAE values across PBL schemes is minimal, with the exception of temperature and precipitation from the TEMF scheme. Error values for modeled sounding temperatures are approximately 0.75°C lower compared to surface values and nearly half for wind direction. Wind speed errors are 1 ms^{-1} greater from modeled sounding profiles than at the surface, although the increased magnitude of wind speeds above the surface largely accounts for the difference. Linear correlations between modeled and observed surface values are high for temperature and precipitation (0.8 to 0.9), and less for wind speed and direction (0.5 to 0.7). The r-values for sounding variables are greater for all three sounding variables compared to the corresponding surface variables, further indicating that the modeled conditions are more in line with lower tropospheric sounding observations than at the surface. From the paired t-tests, the values of 2-meter temperature and 10-meter wind speed among the PBL simulations are significantly different ($p<0.01$) except for three pairs of simulations (BouLac-TEMF for 2-meter

Table 2.2: Statistical metrics of hourly 2-meter temperature (T2, N = 11,472), 10-meter wind speed (WS10, N = 11,416) and wind direction (WD10, N = 9,608), and 6-hour precipitation (PRE, N = 1,520) by PBL scheme simulation, averaged over all stations for 21-23 December. Precipitation metrics include U.S. stations only.

Variable	Scheme	Bias	MAE	R
T2 (°C)	YSU	-0.02	1.93	0.95
	ACM2	-0.52	1.85	0.96
	MYJ	-1.18	1.89	0.97
	QNSE	-1.10	1.87	0.97
	MYNN2	0.33	2.06	0.95
	BouLac	1.00	2.12	0.95
	UW	-0.29	2.15	0.95
	TEMF	1.14	3.14	0.92
WS10 (ms^{-1})	YSU	0.49	1.70	0.57
	ACM2	0.58	1.67	0.60
	MYJ	0.83	1.52	0.72
	QNSE	0.70	1.53	0.70
	MYNN2	0.02	1.61	0.56
	BouLac	0.98	1.90	0.61
	UW	0.42	1.64	0.58
	TEMF	0.89	1.93	0.48
WD10 (degrees)	YSU	4.69	28.57	0.52
	ACM2	5.00	24.25	0.51
	MYJ	4.05	22.42	0.57
	QNSE	0.46	23.48	0.55
	MYNN2	5.48	28.96	0.48
	BouLac	6.83	31.30	0.46
	UW	2.38	26.28	0.47
	TEMF	-0.29	28.48	0.48
PRE (mm)	YSU	0.50	1.00	0.80
	ACM2	0.58	0.99	0.81
	MYJ	0.46	0.99	0.80
	QNSE	0.47	0.99	0.80
	MYNN2	0.49	1.00	0.80
	BouLac	0.42	0.98	0.81
	UW	0.48	1.01	0.79
	TEMF	2.78	3.11	0.53

Table 2.3: Statistics of sounding temperature (T, N = 4,880), wind speed (WSP, N = 3,869), and wind direction (WDR, N = 3,869) for each PBL scheme simulation at mandatory and significant levels from the surface to 700 hPa, averaged over all stations.

Variable	Scheme	Bias	MAE	R
T ($^{\circ}C$)	YSU	0.40	1.24	0.98
	ACM2	0.26	1.22	0.98
	MYJ	0.17	1.21	0.98
	QNSE	0.17	1.27	0.97
	MYNN2	0.45	1.25	0.97
	BouLac	0.58	1.39	0.97
	UW	0.48	1.31	0.97
	TEMF	1.16	1.83	0.95
WSP (ms^{-1})	YSU	-0.15	2.86	0.91
	ACM2	0.02	2.68	0.92
	MYJ	0.02	2.83	0.91
	QNSE	0.14	2.93	0.90
	MYNN2	0.01	2.92	0.91
	BouLac	-0.44	2.69	0.92
	UW	0.12	2.84	0.91
	TEMF	0.71	3.36	0.87
WDR (degrees)	YSU	0.93	10.41	0.66
	ACM2	1.14	10.15	0.60
	MYJ	0.78	10.10	0.66
	QNSE	0.06	10.32	0.65
	MYNN2	1.11	10.29	0.71
	BouLac	0.12	10.05	0.69
	UW	0.85	10.16	0.65
	TEMF	-1.16	12.00	0.61

temperature, MYJ-TEMF and BouLac-TEMF for 10-meter wind speed). For the values of 10-meter wind direction, 20 of the 28 pairs of simulations are significantly different, as well as all of pairs with the TEMF simulation for 6-hour precipitation. The modeled values of sounding temperatures and wind speeds are also significantly different among the simulations, with the exception of two pairs of simulations (MYJ-QNSE and MYNN2-UW) for temperature, eight pairs of simulations (ACM2-MYJ, ACM2-QNSE, ACM2-MYNN2, ACM2-UW, MYJ-MYNN2, QNSE-MYNN2, QNSE-UW, MYNN2-UW) for wind speed. In contrast, modeled values of wind direction are significantly different for only 4 pairs of simulations (YSU-MYJ, YSU-BouLac, MYJ-MYNN2, and MYNN2-BouLac).

In comparing cross sections and surface time series for the PBL simulations, we find that the schemes generally exhibit the same systematic biases near the frontal boundary. Figure 2.11 shows time series of 2-meter temperature and 10-meter winds for Portland, ME; the closest surface station to the Gray sounding location. Overall, the MYJ, QNSE, and ACM2 simulations tend to result in lower surface temperatures than the other PBL schemes, with more pronounced cold biases and lesser warm biases. Similarly, the BouLac simulation tends to have the largest warm biases. However, in all of the simulations WRF tends to underestimate surface temperatures at 1200 UTC 21 December and 1200 UTC 22 December, and overestimate surface temperatures at 0000 UTC 22 December. Where the

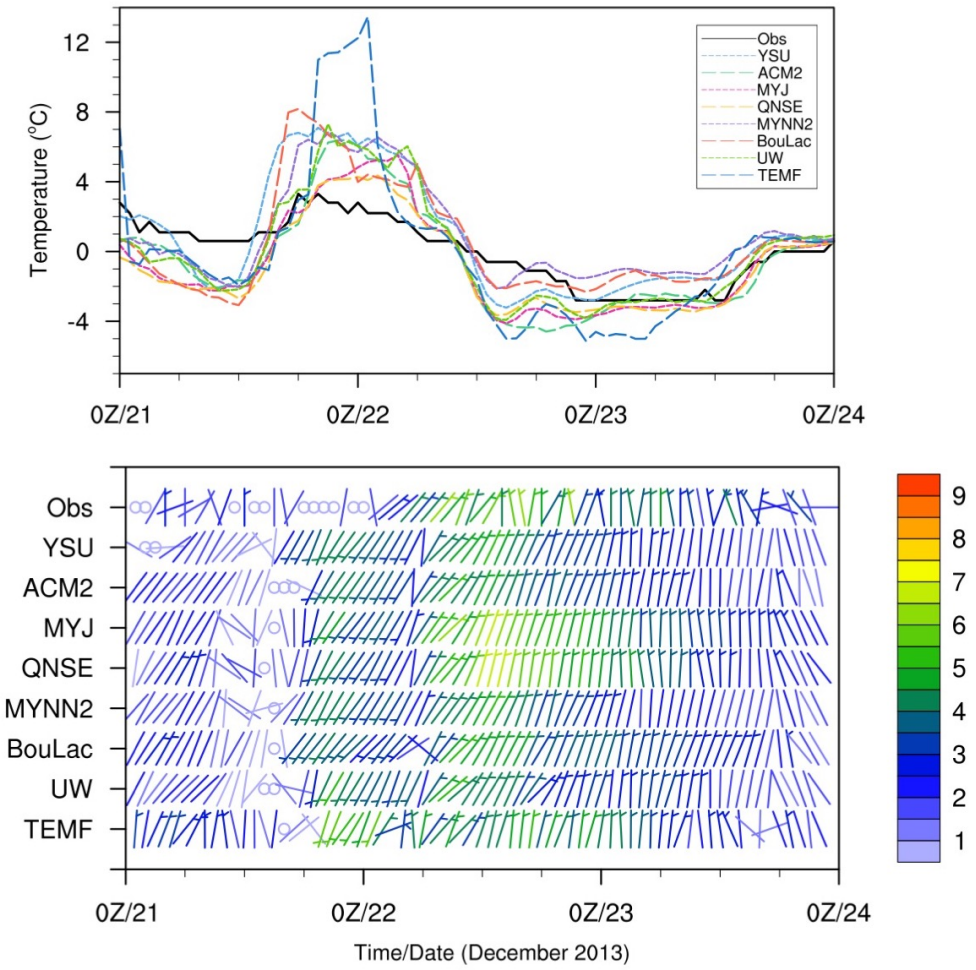

Figure 2.11: Comparison of observed and modeled (PBL simulations) 2-meter temperature (top, in ℃) and 10-meter wind (bottom, in ms^{-1}) time series for Portland, ME.

PBL simulations differ is the exact timing and the magnitude of the warm bias in surface temperatures, which correspond to a simulated wind shift from north/northeast to south/southeast. The same behavior is present at the Augusta, Bangor, and Millinocket surface stations, although the temperature maximum at 0000 UTC 22 December is less pronounced for stations farther north of the front. The only simulation which differs significantly is the TEMF scheme, which exhibits an enhanced surface temperature gradient on 21 December similar in characteristic to the later episode (Fig. 2.12). Winds are substantially stronger within the subfreezing and above freezing air masses and the temperature gradient more pronounced compared to the other PBL simulations. These conditions persist into 22 December, resulting in overestimated temperatures by as much as 10°C up to 700 hPa at the Gray sounding site and enhanced precipitation accumulations compared to the other WRF simulations (Fig. 2.13).

As the temperature gradient strengthens on 22 December, the simulations can be sorted into two groups. The MYJ, QNSE, and ACM2 schemes tend to represent the front with a

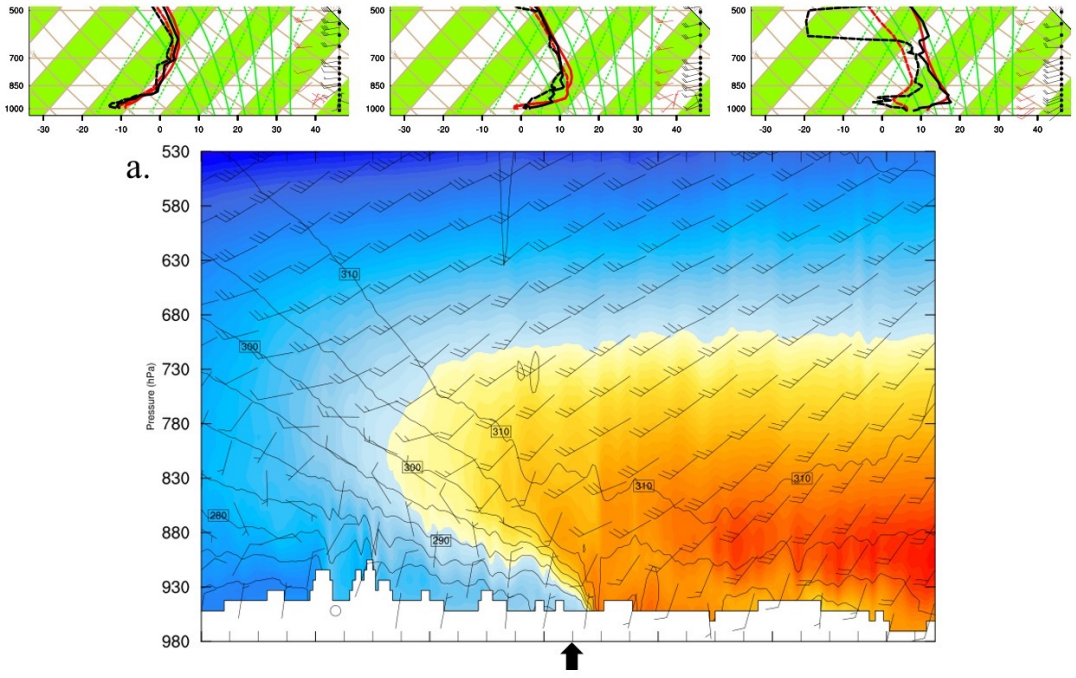

Figure 2.12: Cross sections and soundings at (a) 0000 UTC and (b) 1200 UTC 21 Dec, and (c) 0000 UTC 22 Dec for the TEMF simulation.

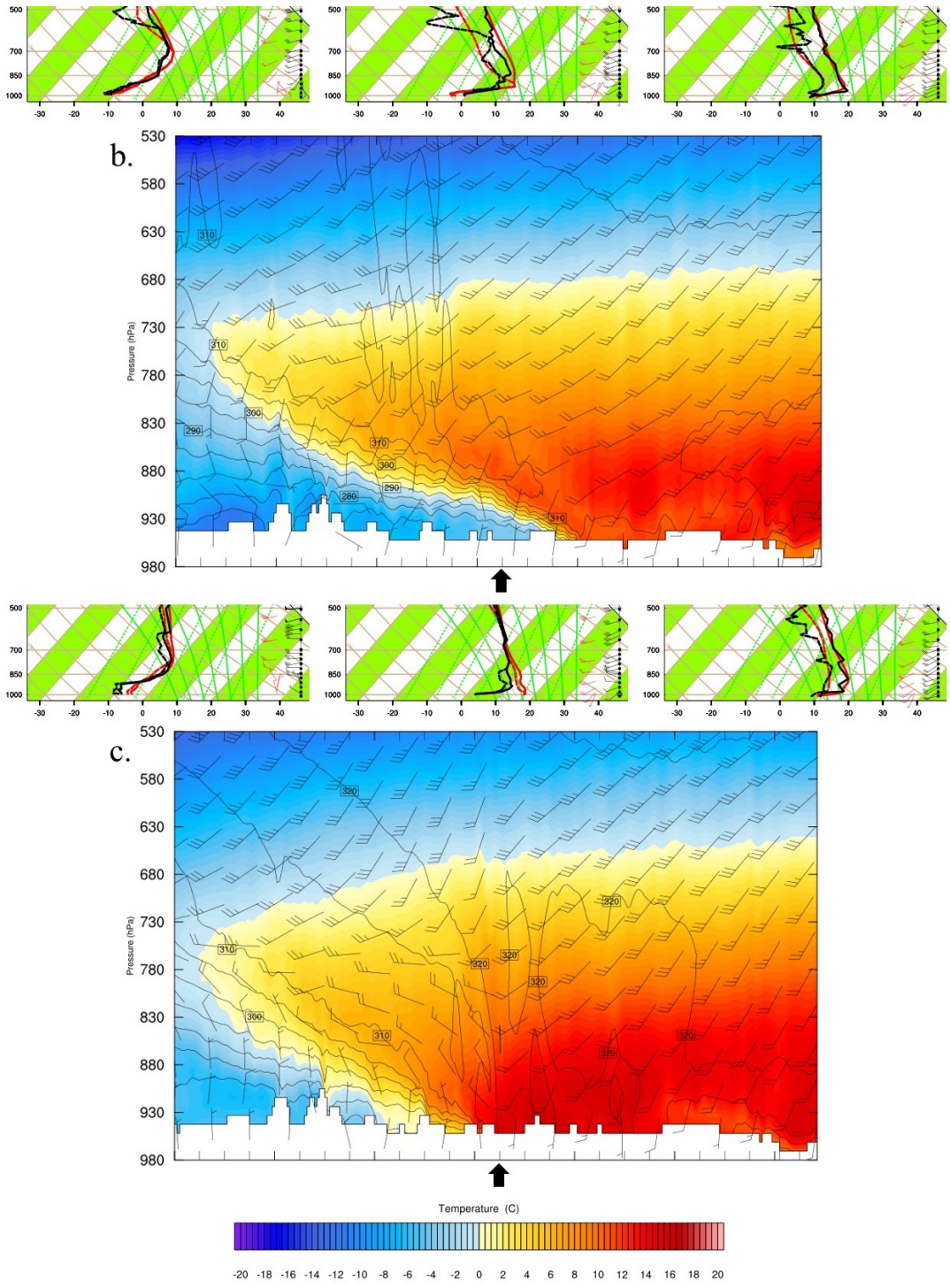

Figure 2.12: Continued.

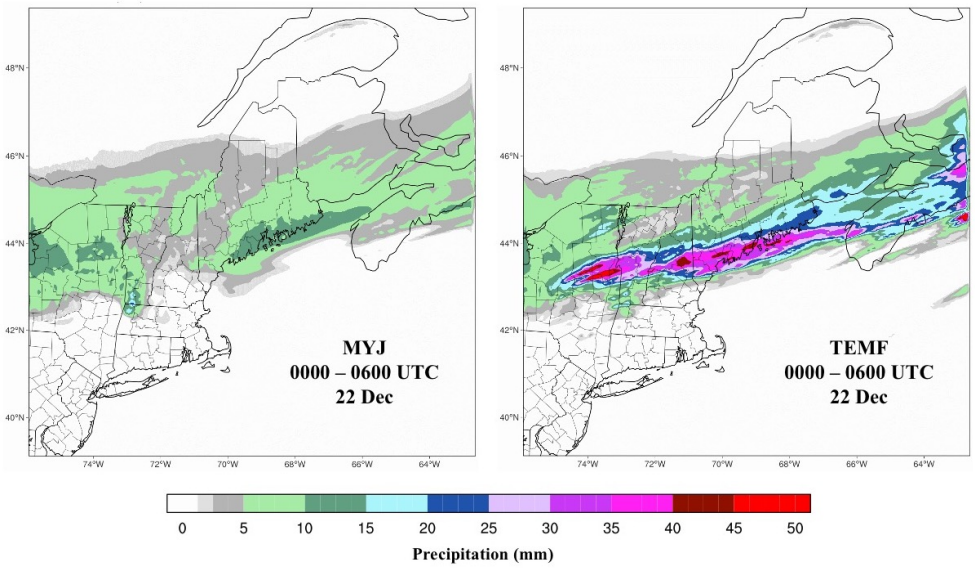

Figure 2.13: Six-hour accumulated precipitation (mm) from 0000 UTC to 0600 UTC 22 Dec for the MYJ (left) and TEMF (right) PBL simulations.

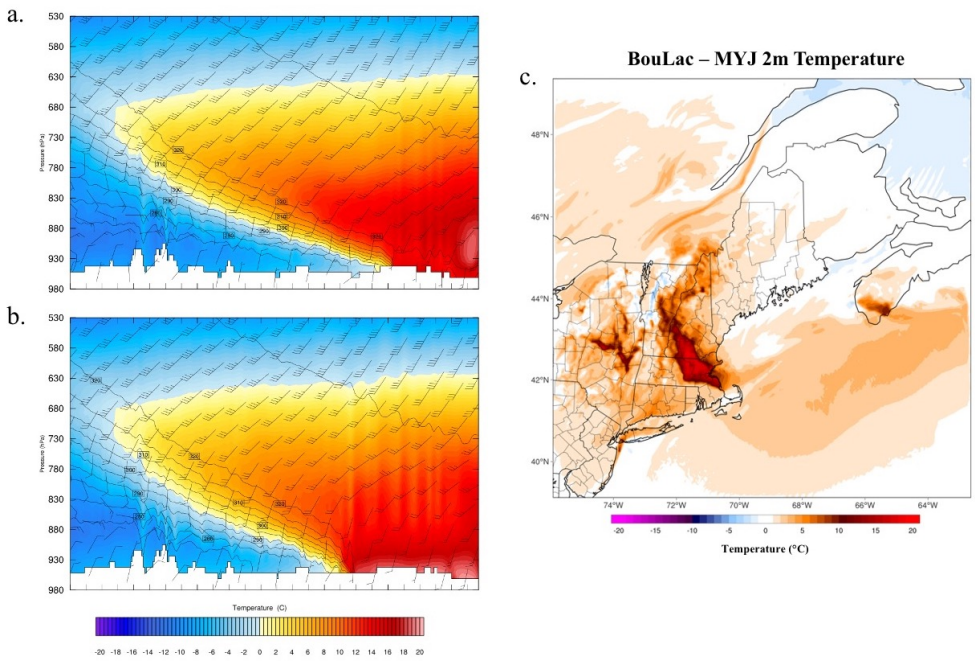

Figure 2.14: Comparison of frontal passage variation between simulations: cross section of the (a) MYJ and (b) BouLac simulations, and (c) 2-meter temperature difference (°C) map between the BouLac and MYJ simulations at 1800 UTC 22 Dec.

shallower slope and the southward advancement of the cold air mass at a uniform rate, while the other PBL simulations show the surface air mass stalling in southern New Hampshire before moving into southern New England. This delay results in extremely overestimated surface temperatures at the southern stations in which the front passes over (Fig. 2.14). To north of the front, the temperature time series for the PBL simulations follow observations but with a spread of 2-3°C between them.

2.4.3 Sensitivity to Reanalysis and Model Setup

This section examines the sensitivity of WRF to other factors besides physics options, in part to pinpoint the source of systematic biases. This group of sensitivity tests focus on several model setup options that were determined through preliminary simulations and kept constant throughout the PBL simulations. The tested setup options include choice of reanalysis, use of grid nudging versus no grid nudging, and the chosen number of vertical levels for the simulation. Three of the simulations are variations of the "control" setup using the ERAI dataset, the MYJ PBL scheme, 36 model levels, and grid nudging: one simulation using 36 model levels and no grid nudging, and two simulations using 46 model levels with and without grid nudging. Four simulations are driven by two other reanalysis datasets (NARR and ERA5), also with and without grid nudging.

Table 2.4 and Table 2.5 show the results of the 3-day domain-wide surface and sounding (surface to 700 hPa) error statistics, respectively, calculated for the model sensitivity simulations. As with the PBL simulations, MAE values are larger for near-surface temperature and wind direction and for wind speed above the surface. These values also vary within a similar range as the PBL error values: 1-2°C for temperature, 1-3 ms^{-1} for wind speed, 20-30 degrees for wind direction, and 1-1.5 mm $(6-h)^{-1}$ for precipitation. Although the NARR simulation without grid nudging shows higher biases and MAE values for temperature and wind, the values are not nearly as extreme as those for the TEMF PBL simulation. R-values are similarly higher for temperature and precipitation compared

Table 2.4: As in Table 2.2, except by model setup simulation. The ERAI 36N simulation corresponds with the MYJ PBL simulation. Tests designated with an N denote grid nudging.

Variable	Test	Bias	MAE	R
T2 (°C)	ERAI 36N	-1.18	1.89	0.97
	ERAI 36	-0.08	2.15	0.94
	ERAI 46N	-0.98	1.81	0.97
	ERAI 46	0.13	2.02	0.95
	ERA5 36N	-1.13	1.88	0.96
	ERA5 36	-0.59	1.77	0.96
	NARR 36N	0.31	2.00	0.94
	NARR 36	1.42	2.64	0.90
WS10 (ms^{-1})	ERAI 36N	0.83	1.52	0.72
	ERAI 36	1.72	2.33	0.53
	ERAI 46N	0.77	1.50	0.71
	ERAI 46	1.60	2.25	0.53
	ERA5 36N	1.09	1.75	0.67
	ERA5 36	1.36	1.94	0.68
	NARR 36N	0.35	1.59	0.63
	NARR 36	2.00	2.71	0.44
WD10 (degrees)	ERAI 36N	4.05	22.42	0.57
	ERAI 36	3.20	31.28	0.50
	ERAI 46N	2.32	22.70	0.56
	ERAI 46	0.59	30.63	0.50
	ERA5 36N	0.79	24.77	0.52
	ERA5 36	3.40	25.51	0.53
	NARR 36N	-0.19	30.61	0.53
	NARR 36	3.66	38.62	0.45
PRE (mm)	ERAI 36N	0.46	0.99	0.80
	ERAI 36	0.84	1.51	0.61
	ERAI 46N	0.48	0.99	0.80
	ERAI 46	1.03	1.63	0.58
	ERA5 36N	0.42	1.06	0.78
	ERA5 36	0.93	1.28	0.80
	NARR 36N	-0.29	1.03	0.59
	NARR 36	0.49	1.04	0.81

to wind speed and direction and are higher for sounding variables compared to those at the surface. The paired t-tests indicate that the values of 2-meter temperature and 10-meter wind speed among the model sensitivity simulations are significantly different ($p<0.01$) except for one pair of simulations (ERA4 36-NARR 36) for 2-meter temperature and two pairs of simulations (ERAI 46N-NARR 36 and ERA4 36-NARR 36) for 10-meter wind

Table 2.5: As in Table 2.3, except by model setup simulation.

Variable	Test	Bias	MAE	R
T (°C)	ERAI 36N	0.18	1.21	0.98
	ERAI 36	0.17	1.43	0.97
	ERAI 46N	0.22	1.25	0.98
	ERAI 46	0.32	1.56	0.96
	ERA5 36N	-0.39	1.32	0.97
	ERA5 36	-0.21	1.35	0.97
	NARR 36N	0.50	1.40	0.97
	NARR 36	0.80	1.90	0.94
WSP (ms^{-1})	ERAI 36N	0.02	2.83	0.91
	ERAI 36	0.92	3.29	0.89
	ERAI 46N	0.10	2.92	0.92
	ERAI 46	1.22	3.53	0.89
	ERA5 36N	-0.45	2.95	0.91
	ERA5 36	0.83	3.08	0.90
	NARR 36N	-1.48	3.46	0.88
	NARR 36	1.38	3.63	0.86
WDR (degrees)	ERAI 36N	0.78	10.10	0.66
	ERAI 36	-1.32	11.02	0.62
	ERAI 46N	0.33	11.02	0.65
	ERAI 46	-0.31	12.80	0.59
	ERA5 36N	-4.09	9.75	0.71
	ERA5 36	-2.74	11.15	0.65
	NARR 36N	-1.53	12.56	0.64
	NARR 36	-0.84	14.17	0.61

speed. Additionally, the modeled values of 10-meter wind direction for 20 of the 28 pairs of simulations, as well as modeled values of 6-hour precipitation for 13 of the 28 pairs, are significantly different. The modeled values of sounding temperatures and wind speeds are also significantly different among the simulations except for three pairs of simulations (ERAI 36N-ERAI 36, ERAI 36-ERAI 46N, and ERAI 46N-ERAI 46) for temperature and four pairs (ERAI 36/46 with ERA5 36 and NARR 36) for wind speed. As for wind direction, only the modeled values for eight pairs of simulations are significantly different.

As with the PBL simulations, the model setup simulations show the same general behaviors, such as the systematic temperature biases during the first episode, but with varying magnitudes. NARR lateral boundary forcing tends to produce higher surface

temperatures than ERAI for northern New England stations, whereas ERA5 tends to have slightly lower surface temperatures. All of the simulations overestimate near-surface temperatures between 1800 UTC 21 December and 0600 UTC December 22, and most tend to underestimate temperatures at 1200 UTC on 21 and 22 December (Fig. 2.15). However, the NARR simulations exhibit higher temperatures than any of the other simulations from 0000 UTC to 1200 UTC 21 December. This behavior is more pronounced at the Augusta and Bangor surface stations, and to a lesser extent farther north at Millinocket. Grid nudging has a clear impact on the timing and the magnitude of the warm bias for the ERAI and NARR simulations but not for those forced by ERA5. Also, the ERAI simulations with grid nudging exhibit the shallow frontal slope and southward movement of

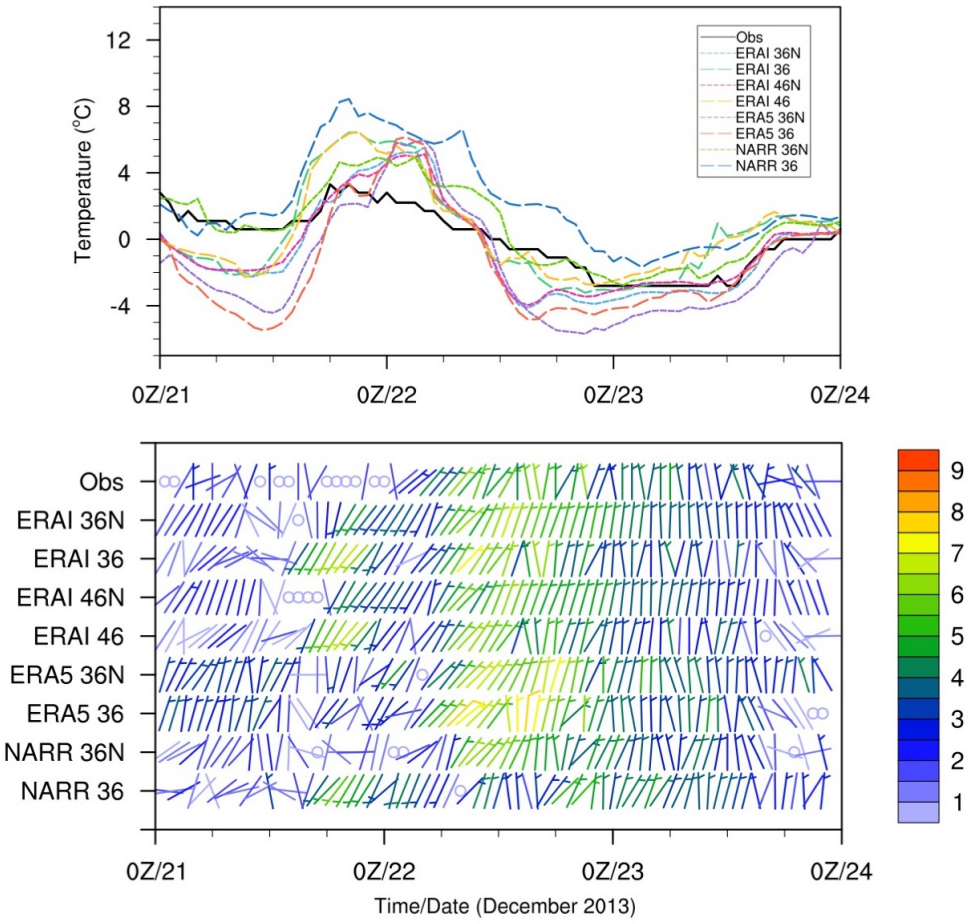

Figure 2.15: As in Fig. 2.11, except for the model setup simulations. The ERAI 36N simulation corresponds to the MYJ PBL simulation.

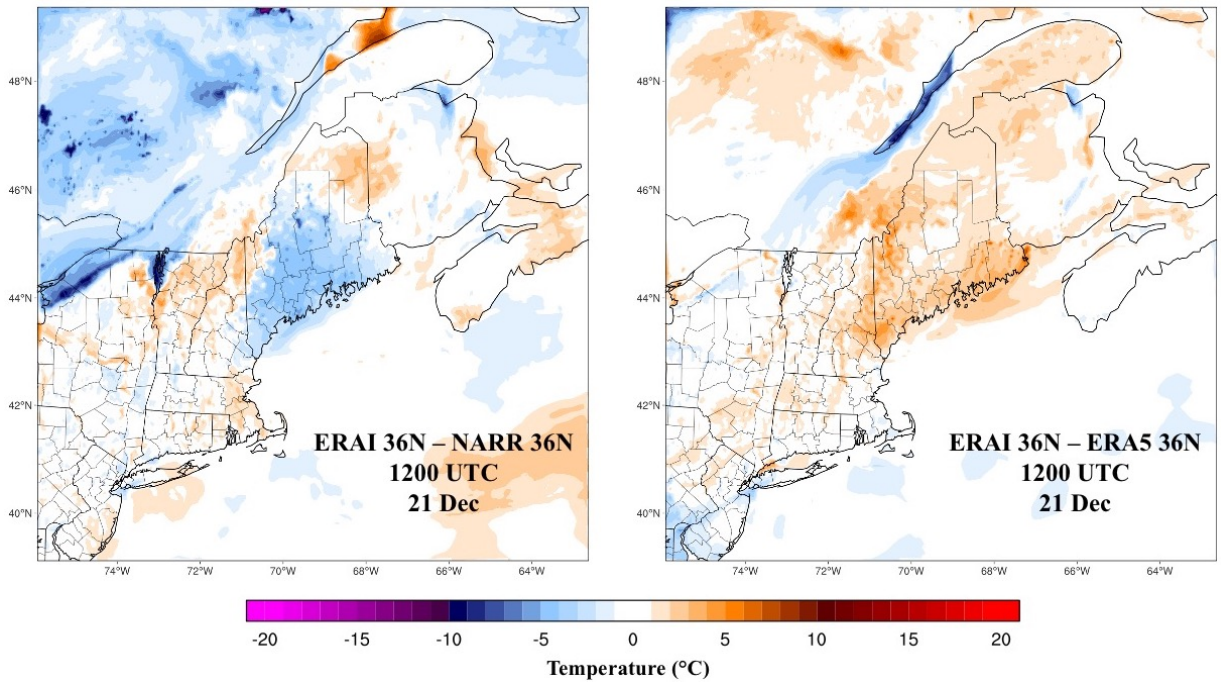

Figure 2.16: Difference in WRF 2-meter temperatures (°C) between ERAI 36N and NARR 36N (left) and ERAI 36N and ERA5 36N (right) simulations at 1200 UTC 21 Dec 2013.

the cold air mass into southern New England as the QNSE and ACM2 schemes, while the simulations without nudging reflect the conditions as shown by the other PBL simulations. The two simulations with 46 vertical levels tend to have slightly higher surface temperatures (< 0.5°C) within the cold dome and slightly lower temperatures to the south and east but are otherwise identical to their 36 level counterpart simulations. All of the model setup simulations generally fall within the same temperature range to the north and south of the frontal boundary during the second episode.

Although the evolution of the ice storm is similar among the model setup simulations, there are notable differences between the simulations which can be traced back to the driving reanalysis dataset. For example, there is an area of persistently cold near-surface temperature anomalies over the St. Lawrence River in the simulations forced by the ERAI reanalysis (Fig. 2.16). These anomalies are due to the relatively coarse resolution of the reanalysis, in which a portion of the river is classified as land while the higher resolution reanalyses categorize the region as water. As a result, surface temperatures are as much as

5°C lower over the river for WRF simulations forced with ERAI and the colder temperatures are advected southeastward into the river valley. Another example of notable temperature anomalies is between the NARR and ECMWF reanalysis simulations due to differences in land surface cover classification over lakes. Near-surface temperatures are often several degrees Celsius higher over open-water lakes than the surrounding area in the NARR simulations. These anomalies are especially prominent over Lake Champlain (Fig. 2.16a) and likely play a substantial role in the differing extent of sub-freezing temperatures within the valley between simulations.

2.4.4 Model Sensitivity and Precipitation Type

For this section, we examine how the differences in modeled surface temperatures between simulations can change the type of precipitation identified. Although the sensitivity simulations show variations in modeled temperature, wind speed and direction, and precipitation values, it is difficult to determine whether the variability would significantly alter precipitation type. WRF does not explicitly identify precipitation type, so previous modeling studies have required the use of outside classification algorithms. However, there are a wide variety of classification algorithms to choose from, each with their own advantages and disadvantages.

As the primary difference between the sensitivity simulations is the modeled temperature values, most prominently at the surface, we chose a simplified "top-down" approach based on the maximum temperature in the warm air mass, which is around 850 hPa, and the surface temperature. The precipitation categories and their respective temperature ranges are listed in Table 2.6. The categories are based on the assumption that cloud temperatures are low enough (typically $<$ -10°C) for the formation of ice crystals that fall into the warm layer, and that the air is saturated in both the warm layer and cold layer when precipitation occurs. Based on the observed and model soundings, as well as the IR images in Figure 2.1, we find this assumption to be valid for the case study

Table 2.6: Temperature thresholds (850 hPa and surface) for precipitation classification. Mixed category includes frozen hydrometeors that result from partially melting (pm) in the warm layer and refreezing (rfrz) within the subfreezing surface layer. Threshold values based on Baumgardt (1999) and UCAR (2005).

Precipitation Type	T850	Tsfc
Snow	< 1°C	< 0°C
Mix	1°C — 3°C (**pm**)	< 0°C
	or	or
	> 3°C (**rfrz**)	$<$ -6°C
Freezing Rain	> 3°C	-6°C — 0°C
Rain	> 3°C	> 0°C

ice storm. The maximum temperature of the warm layer then determines whether the ice crystals completely or partially melt, and the surface temperature determines if refreezing occurs before precipitation reaches the surface. While overly simplistic, this method provides a useful physical representation for each precipitation type: snow indicates the lack of a sufficient melting layer; mixed precipitation signifies partial melting in the warm layer or refreezing in the cold layer; freezing rain represents complete melting within the warm layer and the presence of a shallow subfreezing surface layer; and rain denotes the absence of a subfreezing surface layer.

The sensitivity of precipitation type to model setup depends on the timing of modeled temperature biases in relation to the precipitation field. The underestimated surface temperatures which peak at 1200 UTC 22 December result in minor differences in the transition from freezing rain to mixed precipitation with more noticeable cold biases (Fig. 2.17a,b). However, the impact to precipitation type for underestimated temperatures at 1200 UTC 21 December limited, as modeled precipitation is minimal in regions with high storm total ice accumulations. This is also true for 23 December, as the extent of freezing rain is more isolated than that of the first wave of precipitation (Fig. 2.17c,d). The overestimated modeled surface temperatures shown in all of the simulations around 0000 UTC 22 December have a more substantial effect, resulting in rain throughout Downeast Maine when observations report freezing rain (Fig. 2.17e,f). Simulations which exhibit a

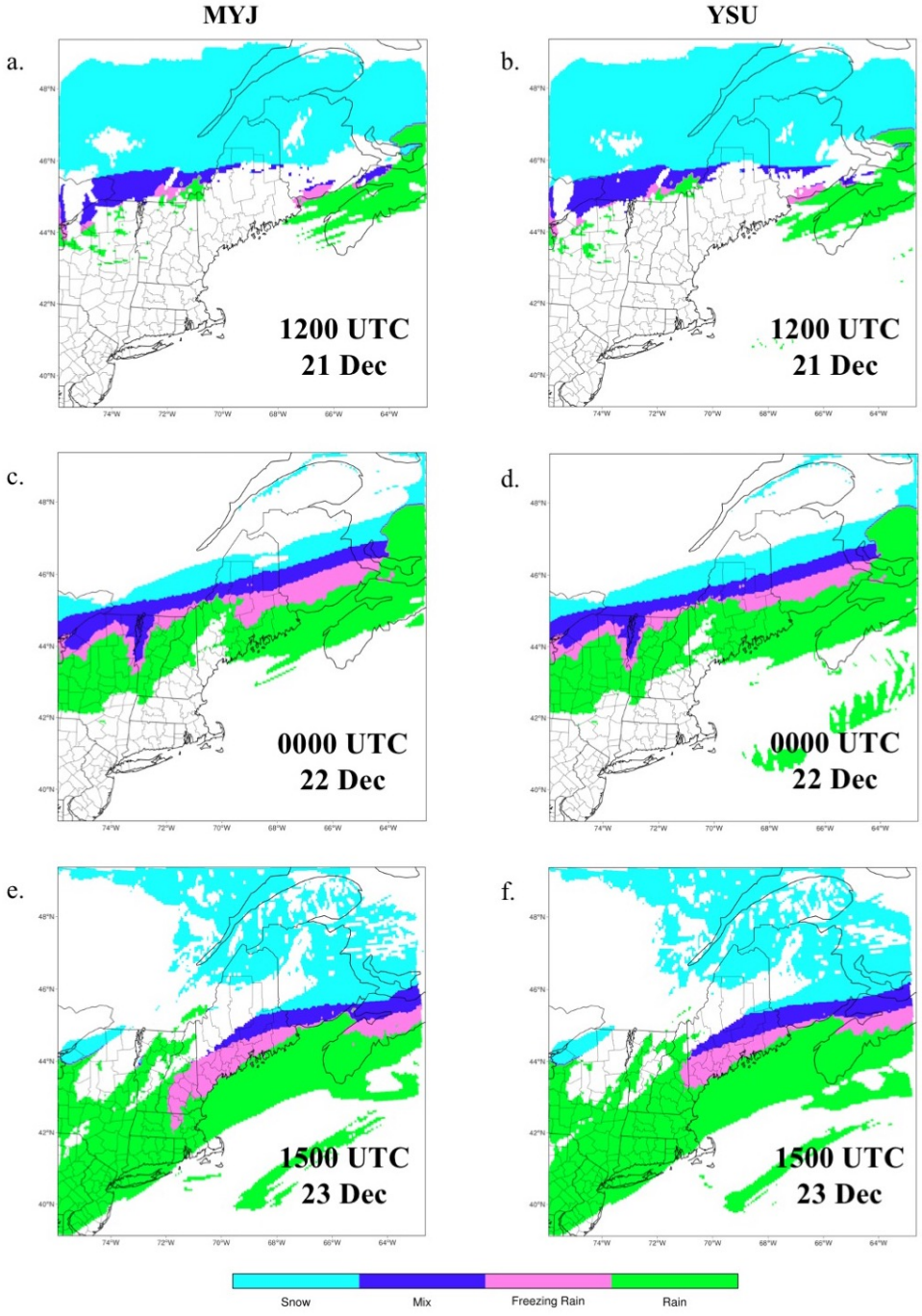

Figure 2.17: Comparison of precipitation type for the MYJ (left) and YSU (right) simulations at 1200 UTC 21 Dec (a, b), 0000 UTC 22 Dec (c, d), and 1500 UTC 23 Dec (e, f).

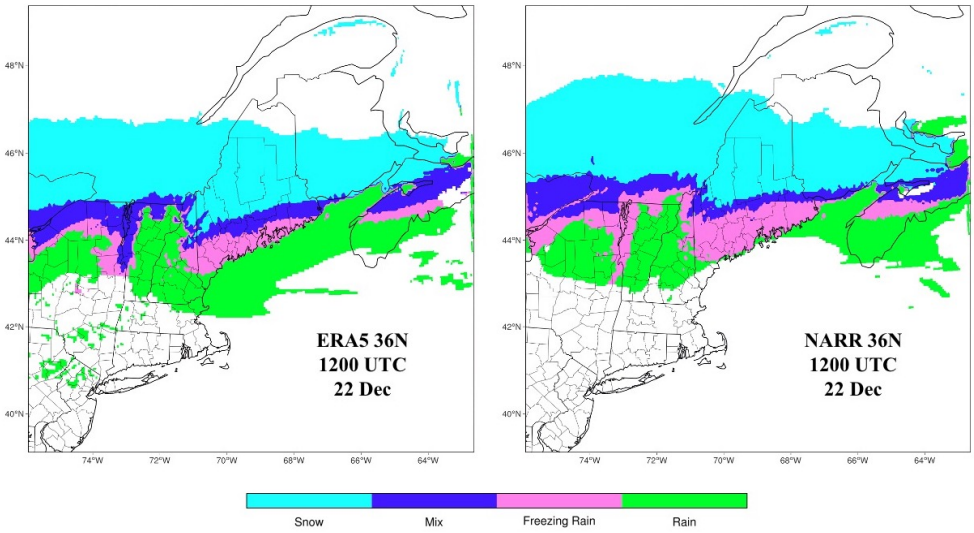

Figure 2.18: Precipitation type at 1200 UTC 22 Dec for the ERA5 36N (left) and NARR 36N (right) simulations.

longer duration of above freezing surface temperatures would result in much lower ice accumulations during this period. Although the spatial extent of precipitation is generally consistent among most of the simulations, there are some distinct differences. For example, the ERA5 and ERAI simulations show a larger expanse of mixed precipitation within the Champlain Valley and in southern Maine while freezing rain is more widespread in the NARR simulations (Fig. 2.18). However, limited observations in this area preclude a more thorough assessment of precipitation classification accuracy.

2.5 Discussion

The sensitivity tests reported here indicate varying confidence in the fidelity of the WRF model solutions. WRF is generally reliable in reproducing the overall meteorological conditions associated with the December 2013 New England ice storm, where the model resolves most temperature inversions, as well as the large-scale movement of the storm system. However, near-surface temperatures close to 0°C are not sufficiently reproduced at the station scale to the precision required for accurate classification of precipitation type. Precipitation type algorithms, such as that used in the HRRR forecast model, and ice

accretion models rely directly on modeled temperature, wind, and precipitation rate to produce icing forecasts. Variability between the simulations are relatively small in plan view, yet not so insignificant as to discount model setup as a factor in assessing forecast accuracy for ice storms. Although the WRF model itself does not explicitly identify precipitation type, we utilize a simplified precipitation classification approach to distinguish regions with a higher probability for freezing rain. Based on the surface temperature biases present, we postulate that the model output would slightly favor the misclassification of freezing rain as sleet or mixed precipitation for simulations that tend to underestimate surface temperatures on 22 and 23 December and that all simulations would favor rain over freezing rain around 0000 UTC 22 December.

It is difficult to identify one simulation that produces an overall robust solution for conditions both inside and outside of the ice storm. Although all of the sensitivity tests produce simulations that follow a similar progression of the ice storm, the model fields are not representative of observations throughout. Some of the simulations produce higher surface temperatures, which minimize the effect of cold biases during the weakly and strongly forced episode at the expense of producing a longer period of abnormally warm temperatures, favoring the identification of rain over freezing rain. Simulations with generally lower surface temperatures similarly favor an earlier transition to mixed precipitation. Our results do not indicate clear differences in the model solution solely by PBL scheme closure or vertical mixing. Only the TEMF scheme stands out as a noticeable outlier, with especially high MAE values for precipitation and near-surface and lower tropospheric temperature. The likely cause of the departures in modeled temperature and precipitation is enhanced frontogenesis on 21 December due to the inclusion of shallow cumulus convection within the TEMF scheme's formulation (Angevine et al., 2010). The NARR forced simulation without grid nudging was similarly an outlier for the model setup simulations, although the greater error values are attributed to systematically higher temperatures as opposed to a marked difference in the overall storm evolution. With the

use of a single case study storm, we cannot determine whether the various model setups tested would perform similarly for another ice storm in this region. Our overall results do not afford a single "best" model configuration; instead, the combined results of the sensitivity tests reflect the interaction among various model components.

Although the scope of this study is limited to a single storm, the extensive validation and analysis of the December 2013 ice storm demonstrates the numerous challenges of modeling ice storms, from both a weather forecasting and research application perspective. Ikeda et al. (2013) note that while current NWP models are better able to predict the areal extent and timing of precipitation associated with large-scale cold season systems compared to warm season convective precipitation, even high resolution forecast models such as the HRRR have difficulty predicting the phase of precipitation for ice storms. As the classification of freezing rain and sleet is more sensitive to model uncertainty compared to rain and snow, the advantage of hindcast case studies is the ability to test a variety of model configurations to identify and minimize systematic model biases. However, previous modeling studies of ice storms using WRF rely on a single model setup and do not examine the ways in which their setup influenced the modeled meteorological conditions, and thus modeled ice accumulations. This and other case study simulations (e.g., Musilek et al., 2009; Pytlak et al., 2010) report similar simulation mean errors in 2-meter temperatures of 1-2°C, and our results indicate several instances in which model setup choices can alter the type of precipitation identified from model output. Furthermore, the WRF results are corroborated solely by a set of surface observations sites, limiting the scope of WRF performance to point locations and not to the large or local-scale features of the individual case study storms. By not addressing the sensitivity of ice forecasting systems to the variable fields they are provided, these systems will require constant modification as NWP models are updated in order to compensate for a variety of uncertainties. These points could hamper the development of generally applicable ice accretion forecasting methods.

2.6 Chapter Summary

This study evaluates the sensitivity of the WRF mesoscale model to several model setup factors in a case study of the New England ice storm of 21-23 December 2013. Simulated values of 6-hour precipitation, as well as near-surface and vertical profiles of temperature, wind speed, and wind direction, are validated against surface station and radiosonde observations. Overall, we find that WRF produces robust depictions of key features of the ice storm, including the large-scale circulation and vertical structure of the atmosphere. The results of the simulations are also consistent with the results of previous ice storm case studies used to develop and run ice accretion models. However, near-surface temperatures vary at the local scale between the suite of sensitivity tests and are not obvious from the simulation average statistical analysis. We find that no single simulation produced high fidelity simulations of the ice storm overall, although the TEMF PBL scheme was clearly unsuitable for the examined weather event. Additional simulations of similar ice storms over New England would be required to determine whether the observed model biases are isolated to this case study. This study underscores the importance of extensive validation and testing to assess the accuracy and realism of the WRF model solution in comparison to observational data, particularly for case studies of weather events as impactful to civil infrastructure as ice storms.

CHAPTER 3

RECENT INCREASES IN GREENLAND BLOCKING AND SUMMERTIME PRECIPITATION ACROSS THE NORTHEASTERN U.S.

3.1 Chapter Introduction

A growing body of literature identifies a trend of increasing annual precipitation over the past 100 years across the northeastern U.S. (USNE) (Brown et al., 2010; Easterling et al., 2017; Frei et al., 2015; Griffiths and Bradley, 2007; Huang et al., 2017; Kunkel et al., 2013a). The most pronounced increase has occurred over the past 20 years, with the rise in total annual precipitation driven in large part by significant seasonal increases in summer and fall (Huang et al., 2017). Extreme events, typically defined as the top 1% of days with precipitation, have also become more frequent and intense across the USNE (Collow et al., 2016; Frei et al., 2015; Hoerling et al., 2016; Howarth et al., 2019; Huang et al., 2018, 2017), where extreme precipitation has increased at a higher rate than any other region in the U.S. (Easterling et al., 2017; Kunkel et al., 2013b).

It is generally thought that the recent increase in extreme precipitation relates to the mid-1990s abrupt shift to positive sea surface temperature anomalies across the North Atlantic associated with multidecadal variability (e.g., Enfield et al., 2001), particularly because of the observed contemporaneous increase in hurricane activity (Goldenberg et al., 2001; Landsea et al., 1999). Rainfall events associated with tropical moisture sources, and land-falling hurricanes and tropical storms, account for 48% of the increase in annual extreme precipitation since 1996 (Huang et al., 2018). Tropical cyclones are responsible for many of the heaviest precipitation events (Barlow, 2011; Howarth et al., 2019); however, only 19% of extreme events from 1979 to 2008 were associated with tropical cyclones (Agel et al., 2015).

The most frequent cause of extreme precipitation annually in the USNE are extratropical cyclones and their associated fronts (Dowdy and Catto, 2017). Substantial

increases in these precipitation events were identified in early summer and late winter, with 25% of the post-1996 extreme precipitation increase attributed to frontal activity in June and July (Huang et al., 2018). Although a causal mechanism for the upsurge in early summer extreme precipitation was not specified, the authors note an associated increase in southerly upper-level winds over the USNE region and northerly winds in the Midwest during this period, consistent with the concomitant weakening of zonal winds and the increased jet stream "waviness" (i.e. higher amplitude tropospheric wave patterns) indicated in other studies (Francis and Vavrus, 2012, 2015; Vavrus et al., 2017). In summer, low-level and mid-level southerly or southwesterly flow promotes greater moisture flux from the Gulf of Mexico and the Atlantic, resulting in heavy rainfall in the USNE (Agel et al., 2019, 2018; Collow et al., 2016; Girardin et al., 2006; Thibeault and Seth, 2014). In contrast, abnormally dry summers are associated with either a more northward-displaced polar jet stream (Klein, 1952) or northerly surface flow linked with ridging to the west (Leathers et al., 2000; Namias, 1966, 1983; Seager et al., 2012), where for both cases the flow of moisture from the Gulf of Mexico and Atlantic into the USNE is reduced.

Although not previously discussed in the literature for the USNE, there are indications that broader circulation changes in the North Atlantic could be related to recent precipitation increases. Previous work has shown that since the 1990s there has been an increasing summertime trend in the Greenland Blocking Index (GBI), a measure of the frequency of high-latitude atmospheric blocking over the North Atlantic basin (Hanna et al., 2016, 2015, 2018a,b). This GBI trend appears to be linked to slower zonal flow and greater meridionality of the North Atlantic jet stream (Francis and Vavrus, 2012, 2015; Overland et al., 2015, 2012). As in other instances of high-latitude blocking, Greenland blocking events tend to divert the prevailing westerly flow equatorward rather than completely block it (Woollings et al., 2008). The resulting southward diversion of the North Atlantic polar jet tends to accompany the negative phase of the North Atlantic Oscillation (NAO) index (Hanna et al., 2015; Overland et al., 2012; Woollings et al., 2010),

which represents fluctuations in the strength of the surface westerlies across the North Atlantic in response to the pressure anomalies across the basin. Previous studies have linked a series of wet summers from 2007 to 2012 in the British Isles and northern Europe to the equatorward shift of storm tracks over the North Atlantic associated with a positive GBI and negative NAO (Blackburn et al., 2008; Folland et al., 2009; Hanna et al., 2016, 2015). Additionally, recent instances of enhanced surface melting of the Greenland Ice Sheet are associated with high GBI index events, where increased southerly flow associated with blocking results in greater transport of subtropical air masses into the region and high pressure promotes sunny and dry conditions (Hanna et al., 2014, 2013; Rowley et al., 2020; Tedesco and Fettweis, 2020).

Identifying mechanisms that contribute to this summertime precipitation surplus will help to clarify the deficiencies of climate projections for the USNE. At present, climate models are unable to skillfully replicate the seasonal cycle and observed historical trends in precipitation across the USNE (Lynch et al., 2016; Rawlins et al., 2012; Thibeault and Seth, 2014, 2015). Current climate projections reflect a continuation of modeled historical precipitation trends – positive trends in winter and spring, contrary to the observed positive trends for the fall and annual average – as well as a phase shift in the seasonal distribution of precipitation, with more annual rainfall occurring during the cold season (November-April) and less during the warm season (May-October) (Lynch et al., 2016). The summer-season contribution to the future annual precipitation signal remains unclear due to differences in the representation of large-scale circulation patterns in the current generation of climate models (Easterling et al., 2017; Karmalkar et al., 2019; Lynch et al., 2016).

Here, we investigate the contribution of increased incidence of high pressure blocking over Greenland and associated shifts in large-scale circulation across the North Atlantic, to recent summer precipitation increases across the USNE. Using atmospheric reanalysis, we highlight circulation features associated with enhanced summertime precipitation in the

USNE. This includes analysis of the upper-level regional and large-scale circulation, as well as low-level and mid-level moisture transport. To examine the association of anomalous circulations with Greenland blocking, we also assess the correlation between the reanalysis circulation features and the GBI. The paper is outlined as follows. Section 3.2 describes the data and methodology employed, which is followed by the results and discussion in Section 3.3 and the conclusions in Section 3.4.

3.2 Data and Methodology

This study utilizes several reanalysis and observational datasets. June-July-August (JJA) precipitation anomaly data for the states of Connecticut, Massachusetts, Maine, New Hampshire, New Jersey, New York, Pennsylvania, Rhode Island, and Vermont are from the U.S. Climate Divisional Database (CDD; Vose et al., 2014) and obtained from NOAA Climate at a Glance (NOAA/NCEI, 2020). The CDD is a 5 km gridded dataset based on station data from the Global Historical Climatological Network-Daily dataset (GHCN-D) and other supplemental data sources. Precipitation anomalies are defined using a 1901-2000 baseline. The GBI is defined as the mean 500 hPa geopotential height averaged from 60°N-80°N, 20°W-80°W (Fang, 2004; Hanna et al., 2015, 2014, 2013; Woollings et al., 2010), calculated using JJA geopotential heights for the period 1948-2019 from the NCEP/NCAR Reanalysis (Kalnay et al., 1996) obtained from the NOAA Physical Sciences Laboratory (NOAA/NCEI, 2019b). Values for the principal component-based NAO index for 1948-2018 were obtained from the NCAR Climate Data Guide (NCAR, 2020). The NAO index is the leading Empirical Orthogonal Function (EOF) of sea-level pressure anomalies over 20°N-80°N, 90°W-40°E from 1899 to present, and is calculated using the NCAR Sea Level Pressure dataset (Hurrell et al., 2020). Reanalysis fields from the ECMWF Reanalysis version 5 (ERA5; Hersbach et al., 2020) and ECMWF Interim Reanalysis (ERAI; Dee et al., 2011) obtained from the Copernicus Climate Change Service (Copernicus Climate Change Service, 2017; ECMWF, 2011) were utilized for circulation

anomaly maps and correlations to the GBI, and the maps were created using the University of Maine Climate Change Institute's Climate Reanalyzer (https://climatereanalyzer.org/). The anomaly maps are used for making comparisons of circulation features for the period of 2003-2019 to a 1979-2002 baseline, focusing on the circulation shifts associated with the summer precipitation changepoint in 2002 identified by Huang et al. (2017).

3.3 Results and Discussion

3.3.1 Key Findings

A comparison of the JJA USNE precipitation anomaly, GBI, and NAO index for the period of 1948-2019 is shown in Figure 3.1. For the full period of 1948-2019, there is a statistically significant ($p < 0.05$) positive trend for USNE precipitation and the GBI, and a negative but not statistically significant trend in the NAO. There is not a statistically significant correlation between USNE precipitation and the GBI/NAO indexes ($r = 0.02$ and $r = 0.04$, respectively). Prior to 2003, summer precipitation in the USNE was generally above average following the drought of the 1960s, with individual years of much higher (+2 in/+50.8 mm) and much lower (-2 in/-50.8 mm) precipitation. This period is characterized by positive and negative trends (not statistically significant) in the GBI and NAO. After 2003, the trends for USNE precipitation and GBI were of the same sign as the previous period and the NAO trend was of the opposite sign (although all are not statistically significant). However, there is a period of especially wet summers and fewer, less intense dry spells corresponding to a period of notably higher GBI years and lower NAO values from 2007 to 2013. Other studies have noted the exceptional nature of these years, such as how seven of the top eleven GBI summer values over the last 165 years occurred after 2007 (Hanna et al., 2016). Similarly, the NAO index was only below -1.25 once between 1950 and 2002, but six times since 2003.

To investigate the circulation patterns associated with the recent wet summers in the USNE, Figure 3.2 compares the fields of several meteorological variables from the ECMWF

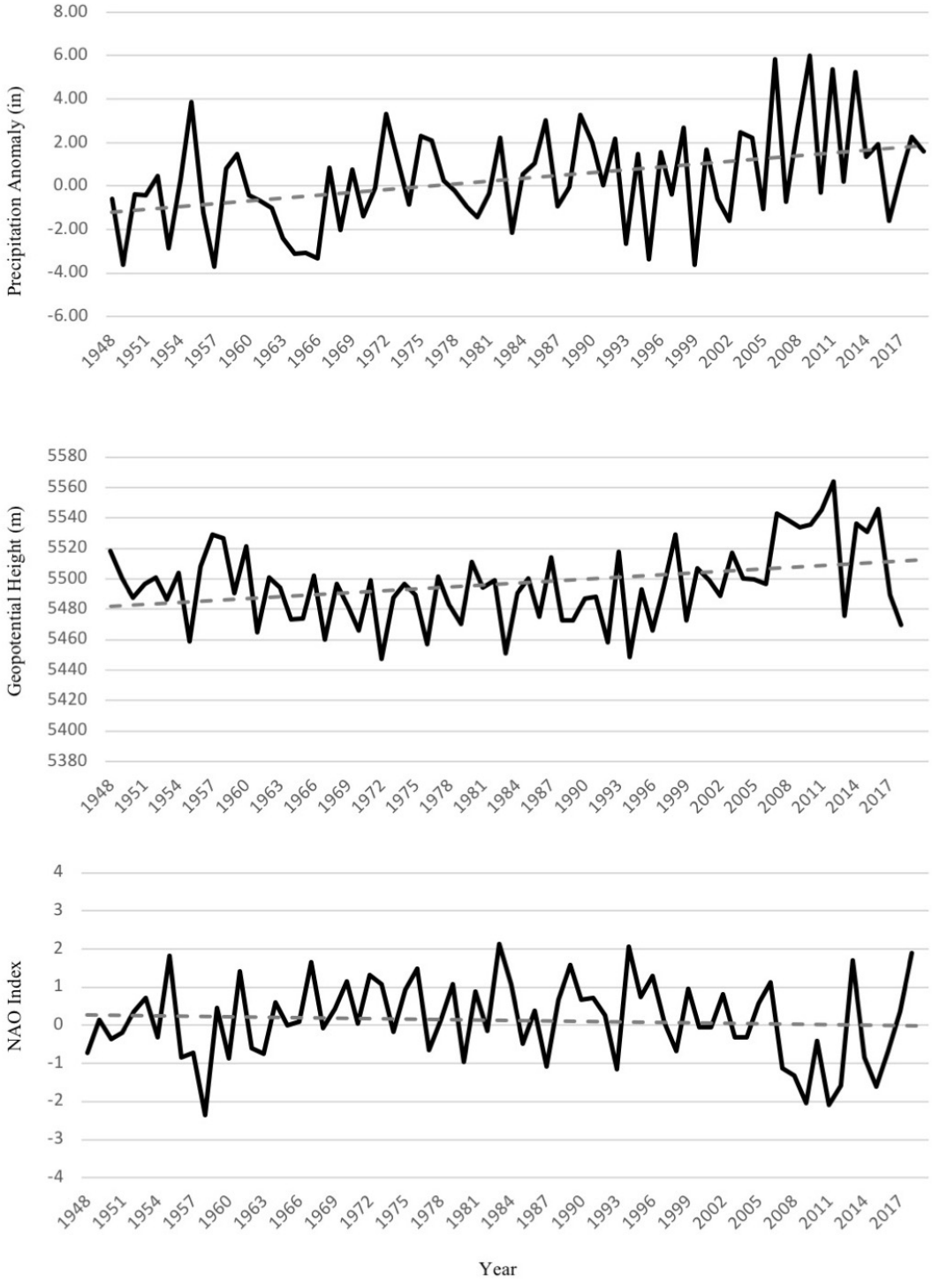

Figure 3.1: Precipitation anomaly (based on 1901-2000 mean, in inches) for the USNE (top), GBI values (middle; in meters), and NAO principal component index (bottom) for JJA. Linear trends are indicated by the dashed lines. The precipitation and GBI trends are statistically significant ($p < 0.05$), the NAO trend is not statistically significant, and the correlation between the GBI and NAO is -0.86.

ERA5 reanalysis for the recent years 2003-2019 compared to a 1979-2002 baseline. Of particular note are the sea-level pressure and upper tropospheric wind anomalies. A surface low-high-low pattern appears over the North Atlantic, with low-pressure centers over the United Kingdom and the eastern U.S. and high pressure over Greenland. At 250 hPa, there are decreased zonal winds over Iceland and the USNE and increased zonal winds to the south of these regions, as well as decreased meridional winds over southern Greenland and increased meridional winds over eastern Canada and the eastern U.S., and the United Kingdom. Increased precipitation over the eastern North Atlantic is coupled with increased 850 hPa moisture transport corresponding with positive zonal and meridional wind anomalies over the region, while increased precipitation over the western North Atlantic and USNE is coupled with increased moisture transport associated only with positive meridional wind anomalies.

Figure 3.3 shows the correlation between several atmospheric variables and the GBI from 1979 to 2015. The correlations with anomalous sea-level pressure are indicative of the summer positive GBI/negative NAO pattern. The upper tropospheric zonal wind anomaly correlations are similarly consistent with a zonal wind pattern corresponding to the positive GBI phase. The upper-level meridional wind anomalies over northeastern Canada and western Greenland also show a statistically significant correlation with the GBI. However, the recent meridional wind anomalies extending farther south over eastern Canada and the eastern U.S., as well as the wind anomalies over the United Kingdom, are not associated with the GBI over the full 37 year period. As for precipitation, only the anomalies over the eastern North Atlantic are correlated with the GBI over the full period.

3.3.2 USNE Impacts from Greenland Blocking and the NAO

Our results suggest that while Greenland blocking and the NAO have exerted substantial influence over the summer precipitation patterns for northern Europe and the United Kingdom since 1979, the higher meridional amplitude pattern associated with more

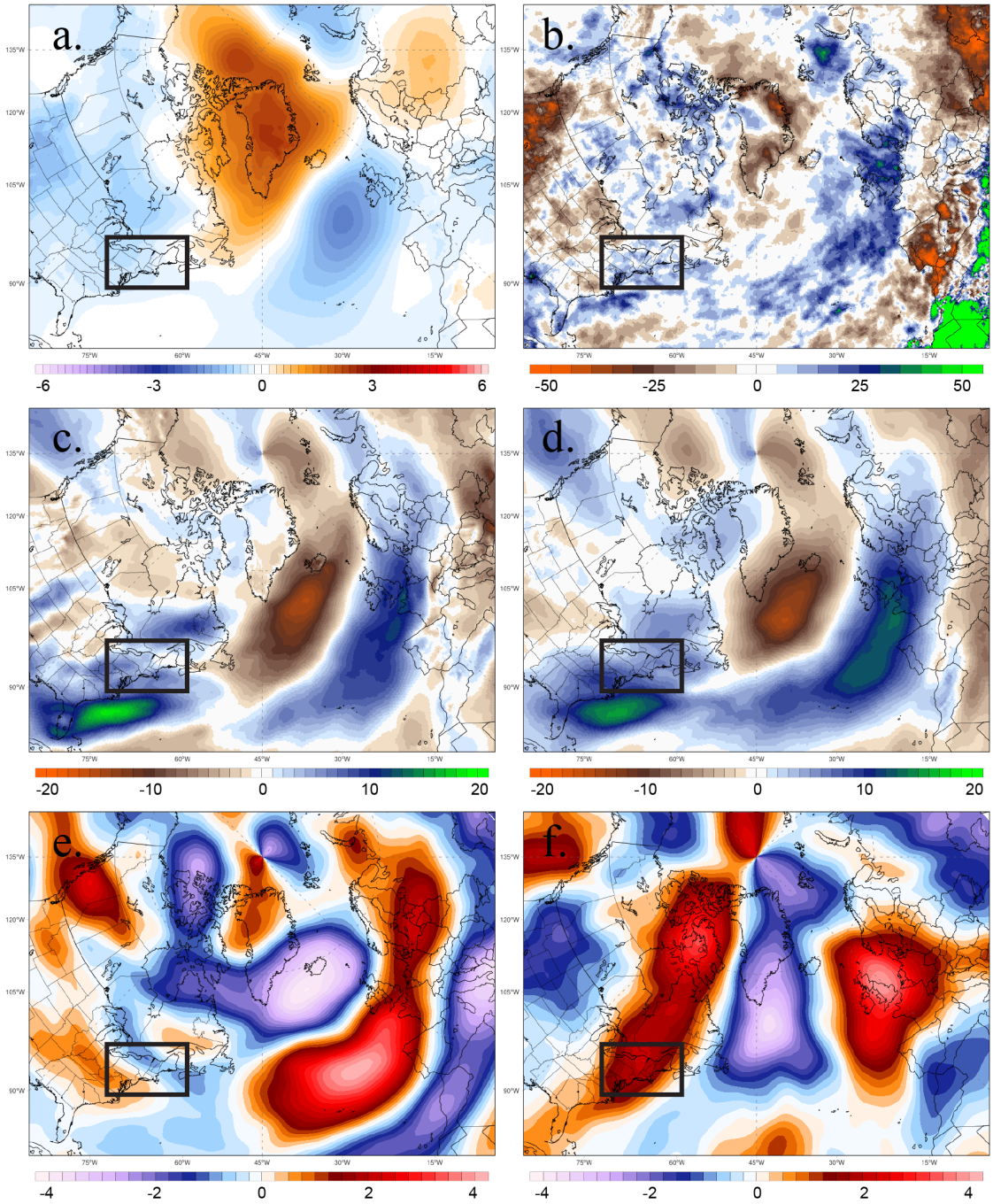

Figure 3.2: Reanalysis anomaly fields (2003-2019 minus 1979-2002) of (a) mean sea-level pressure (hPa), (b) precipitation (% change), (c) 850 hPa moisture transport (kg m^{-1} s^{-1}), (d) 500 hPa moisture transport (kg m^{-1} s^{-1}), (e) 250 hPa u-winds (ms^{-1}), and (f) 250 hPa v-winds (ms^{-1}) for JJA. The USNE region is outlined in black. Maps created using the Climate Reanalyzer and the ECMWF ERA5 reanalysis (Hersbach et al., 2020).

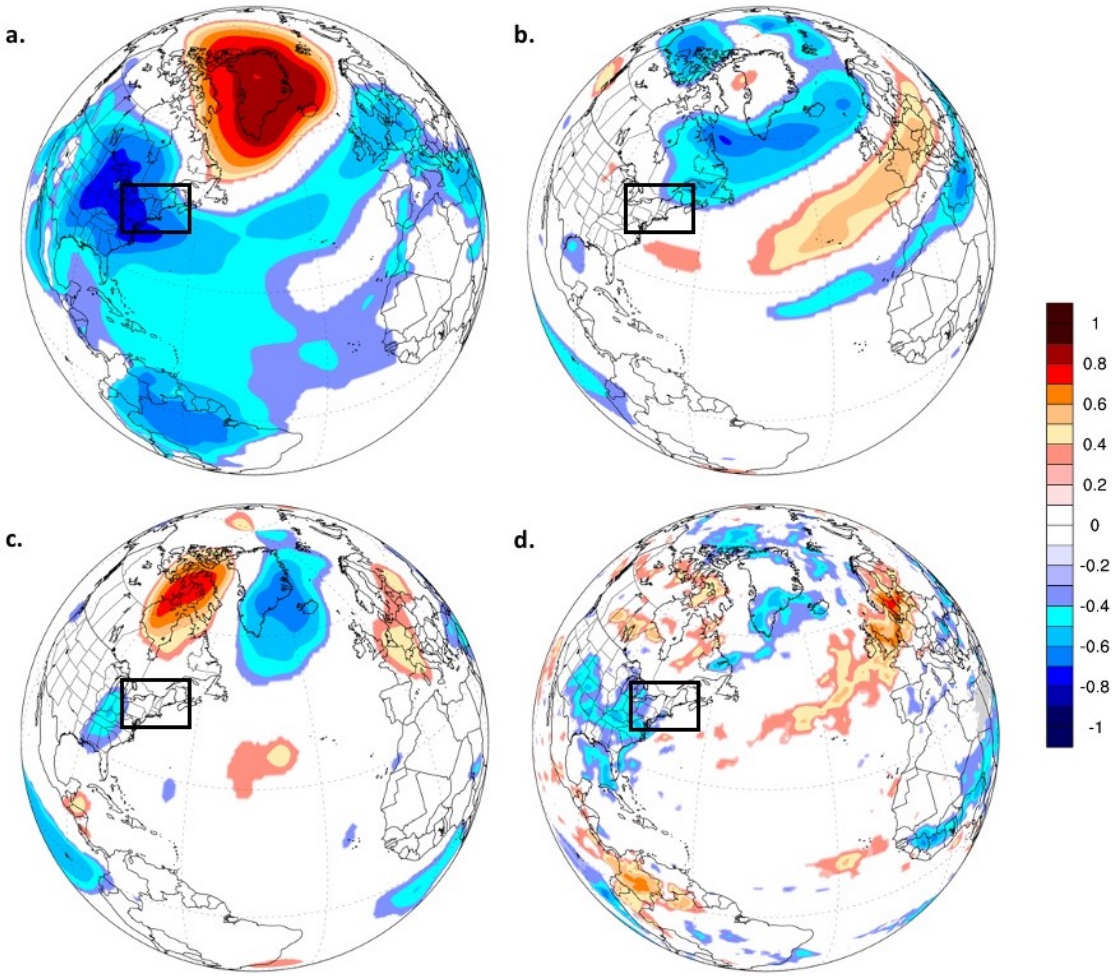

Figure 3.3: Pearson's linear correlation maps of JJA GBI and (a) mean sea-level pressure, (b) 250 hPa u-winds and (c) 250 hPa v-winds, and (d) precipitation for 1979-2015. The USNE region is outlined in black and the plotted correlations are significant at the 95% level. Maps created using the Climate Reanalyzer and the ECMWF ERA-Interim reanalysis (Dee et al., 2011).

frequent Greenland blocking events has impacted summer precipitation in the USNE only in recent years, particularly from 2007 to 2013. The positive precipitation anomalies over the eastern North Atlantic are the result of an equatorward shift in summer extratropical storm tracks, which typically occurs during summers when the GBI is positive and the NAO is negative. In contrast, positive precipitation anomalies over the USNE are more closely associated with the enhanced meridional wave pattern linked to more frequent and persistent blocking over Greenland in recent years. This wave pattern appears to promote

southerly flow over the USNE, which supports oceanic moisture transport into the region and results in heavier rainfall. In studies conducted by Agel et al. (2019, 2018), three summertime large-scale meteorological patterns were identified in connection with extreme precipitation events in the USNE. Two of the patterns (designated by the authors as C1 and C4) are associated with weak synoptic systems or trailing cold fronts from remote cyclones, resulting in widespread light precipitation with localized extremes. Heavy rainfall associated with the third pattern (designated as C5) is likely to be closely related to storms tracks, with inland extreme precipitation forced by weaker storms and trailing cold fronts while coastal extreme precipitation is forced by stronger storms and southerly moisture transport from offshore warm conveyer belts and warm fronts. The circulation features for extreme versus non-extreme events associated with each pattern are similar, but enhanced moisture transport is one key ingredient which accompanies extreme precipitation.

Although previous studies have not highlighted an association between Greenland blocking and recent circulation patterns linked to increased precipitation in the USNE, there is ample evidence to support this linkage. The upper-level u and v-component wind anomaly pattern (Figure 3.2e,f) supports the enhanced trough/ridge couplet over the eastern U.S. and western Atlantic proposed by Huang et al. (2018) as contributing to the increase in early summer extreme precipitation attributed to frontal processes. This circulation pattern is often cited as one which promotes strong vertical ascent of air as well as moisture flux into the USNE from the Gulf of Mexico and the Atlantic (Collow et al., 2016; Leathers et al., 2000; Thibeault and Seth, 2014). Birkel and Mayewski (2018) also linked the North Atlantic high-low configuration to the unusually wet interval 2005-2014 over the U.S. state of Maine. Likewise, long-term precipitation records for Farmington, Maine show a 30% increase in precipitation volume during this wet period, largely due to more 1 inch and 2 inch precipitation events (Fernandez et al., 2020) [the extreme precipitation threshold for this station is 2.26 inches/57.1 mm (Agel et al., 2015)]. Increased summer extreme precipitation in the USNE over the period 1980-2014 is

furthermore associated with decreased sea-level pressure and 500 hPa geopotential heights over the USNE, as well as increased 500 hPa geopotential heights to the northeast of the region (Collow et al., 2016, 2017).

3.3.3 Possible Connection to Arctic Warming and Sea-Ice Loss

While it is unclear what mechanisms produced the recent positive GBI trend, it has been suggested that the increase in occurrence of summer Greenland blocking events is influenced by a number of atmospheric and cryospheric climatic factors. In particular, dramatic warming across the Arctic over the past two decades is argued to be coupled to a weakening of upper-level westerlies in response to weakening of the poleward temperature gradient, and the development of larger amplitude planetary waves, which in turn accompany increased geopotential heights in high latitudes (Francis and Vavrus, 2012; Overland and Wang, 2010). Slower zonal flow of the polar jet stream would then encourage more frequent and intense blocking events (Francis and Vavrus, 2012, 2015; Overland et al., 2015, 2012). The characteristics of the underlying landmass and topography of Greenland also promote ridging and high surface pressure (Scorer, 1988). Additionally, researchers have indicated Greenland blocking could also be influenced by anomalous Rossby wave-train activity originating in the central Pacific, as the circulation anomalies are similar to those associated with the negative phase of the NAO (Ding et al., 2014).

The period of high GBI summers also coincides with a period of record low sea-ice extent in the Arctic (Stroeve et al., 2012a,b). In model simulations, the jet stream displacement and precipitation response to Arctic sea-ice loss closely resembles the spatial pattern for the wet summers in the United Kingdom and northern Europe from 2007 to 2012, indicating that the change in sea-ice extent may have been a contributing driver of the increased summer precipitation in those regions (Screen, 2013). It has also been suggested that the recent rise in summer Greenland blocking may be influenced by the shift towards positive sea surface temperature anomalies in the North Atlantic (indicated

by the positive phase of the Atlantic Multidecadal Oscillation [AMO]), as the response of the polar jet stream to these anomalies is also similar to the negative phase of the summer NAO, and thus a more positive GBI (Folland et al., 2009; Sutton and Dong, 2012). However, it is unclear to what extend each of these factors have contributed to the Greenland blocking trend, as the potential mechanisms listed here result in similar effects on the upper-tropospheric circulation in the North Atlantic.

3.3.4 Climate Model Limitations

This link between regional precipitation and large-scale circulation changes highlights the limitations of current climate projections, which rely on climate model simulations. At present, the literature shows that state-of-the-art climate models do not correctly depict seasonal patterns or trends in precipitation for the USNE. Lynch et al. (2016) found that climate models from the Coupled Model Intercomparison Project version 5 (CMIP5; Taylor et al., 2012) are unable to skillfully replicate the seasonal cycle and observed historical trends in precipitation across the USNE, despite being able to represent key circulation characteristics important to summer precipitation such as moisture convergence associated with southwesterly flow and divergence aloft. In light of the potential teleconnection between shifts in large-scale circulation and precipitation in the USNE, the inadequate representation of key properties of the North Atlantic polar jet stream (e.g., wave amplitude) and blocking patterns over Greenland by the CMIP5 models have implications for interpreting climate projections for the USNE. Hanna et al. (2018a) found that not only do CMIP5 models not show the recent increase in Greenland blocking, they actually indicate a negative trend in blocking in historical simulations that continues in forward projections. Although the authors suggest that internal variability may have contributed to the recent trend, which could result in differing trends between model output and observations, a comparison of the GBI calculated from reanalysis and CMIP5 simulations clearly shows that all of the models are unable to capture the amplitude of the recent

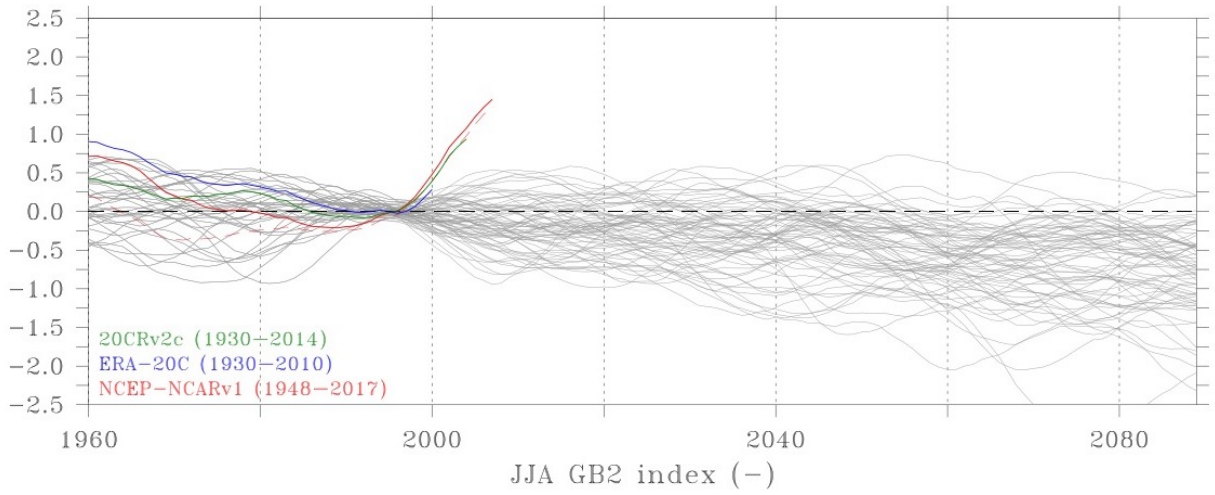

Figure 3.4: Time series of JJA GBI from NCEP/NCAR Reanalysis 1, 20CRv2c reanalysis, and ERA-20C, as well as the historical scenario (1950-2005) and the RCP4.5 and RCP8.5 scenarios from all CMIP5 models. A 20-year moving average was applied to the time series, and the values normalized to the 1986-2005 period. Figure from Hanna et al. (2018a).

change in Greenland blocking (Fig. 3.4). This implication is especially concerning, as the underestimation of blocking in the North Atlantic has persisted in climate models of the last 20 years with little improvement (Davini and D'Andrea, 2016). If the blocking trend is a forced signal and not due to internal climate variability, then climate models could potentially be underestimating an important contribution to summer rainfall in the USNE if the GBI trend continues or Greenland blocking becomes more frequent in the future. It remains to be seen whether these deficiencies will be rectified in the next iteration of CMIP.

3.4 Chapter Summary

This study links recent changes in summer precipitation in the USNE to large-scale atmospheric circulation shifts associated with Greenland blocking, most notably during a span of summers from 2007 to 2013 when exceptionally high GBI and low NAO index values were observed. We show that the recent increase in summer precipitation occurs in conjunction with more frequent blocking over Greenland (increased GBI), which is associated with a negative NAO. Although most previous work has focused on the association of these recent climate trends with an equatorward shift in summer

extratropical storm tracks over the eastern North Atlantic, the accompanying higher amplitude upper level flow over the eastern U.S. is also linked to heavier precipitation through increased southwesterly moisture transport into the USNE.

The results of this study highlight the limitations of the current generation of climate model projections in reproducing outcomes observed over recent decades. While the association between Greenland blocking and precipitation in the USNE needs to be explored further, the inability for models to replicate the amplitude of the Greenland blocking trend undermines confidence in future climate prediction for precipitation across the western North Atlantic region. Many of the potential drivers of the recent trend produce a similar response on circulation patterns in the North Atlantic, and can influence precipitation patterns in surrounding regions. It is therefore crucial that the next generation of climate models strive toward improving the representation of observed large-scale circulations and trends.

CHAPTER 4

HISTORICAL INCIDENCE OF MID-AUTUMN WIND STORMS

4.1 Chapter Introduction

In the past three years, three notable mid-autumn wind storms, defined in this study as high-wind events associated with extratropical cyclones, caused extensive infrastructure damage across New England, primarily from wind gusts in excess of 50 mi/h and in some cases over 70 mi/h. The most impactful of these storms was a nor'easter (coastal storm) "bomb" cyclone [central pressure drop of at least 24 mb in 24 hours at 60° latitude (Sanders and Gyakum, 1980)], that passed over eastern New York and Vermont on 30 October 2017, and resulted in over 1 million outages to the electric grid (Samenow, 2017). In Maine alone, electric utilities registered nearly 484,000 power outages, a number exceeding that resulting from the historic January 1998 ice storm, and over $69 million in damage to the State's electrical power grid (Graham, 2017; Russell, 2018). In 2019, two major wind storms occurred within two weeks of one another: the first occurred on 17 October with heaviest impact over eastern Massachusetts and southern Maine, and the second on 1 November with impacts from central to northern Maine. The 17 October 2019 storm was another nor'easter that underwent rapid intensification and became a bomb cyclone, setting a new record of 975.3 mb for the lowest atmospheric pressure recorded in Boston, MA for the month of October, and causing over 500,000 power outages (Barry, 2019). The 1 November 2019 storm was an extratropical cyclone that developed over the Ohio Valley, and caused more than 800,000 power outages across 14 states in the Great Lakes, Mid-Atlantic, and Northeastern regions (Stanglin, 2019).

Wind storms represent a major hazard to life and property, as well as a potential mechanism for ecosystem disruption. Ashley and Black (2008) examined the number of fatalities as a result of non-convective high-wind events in the U.S. from 1980 to 2005 and found that these wind events can result in greater loss of life than thunderstorm or

hurricane winds. More than 83% of all fatalities from these events are associated with passing extratropical cyclones, particularly in the U.S. Northeast region, and tend to occur across larger spatial and temporal scales than convective wind events. In forested regions that do not frequently experience fires, wind storms are a major disturbance to the local ecosystem. For example, a 1989 wind storm resulted in damage to 35% of the trees in an old growth forest in central New York (Marks et al., 1999). Also, 33% of wind storm fatalities involve felled trees (Ashley and Black, 2008) and the majority of power outages in states with extensive forest cover are the result of tree damage (Li et al., 2014). Autumn wind storms can potentially result in greater tree damage than those in other seasons, as the presence of foliage increases drag and wind stress on a tree, and thus the risk of tree damage or uprooting from high winds (Vollsinger et al., 2005).

Due to the association of high-wind events with the passage of extratropical cyclones (Booth et al., 2015; Lacke et al., 2007; Niziol and Paone, 2000), most previous work examines high-wind events during the cold season (November – April). In the Great Lakes region and the northeastern U.S., high-wind events during the cold season are most often associated with extratropical cyclones that travel from southwest to northeast, passing to the north and west of the Northeast region. This preferred track is not necessarily associated with the strongest cyclones overall, but instead those in which the strongest winds of the cyclone (typically to the south or southeast of the storm center) pass over the region. Projecting changes to high-wind events will thus, in part, depend on how future storm tracks will shift. Although winter extratropical cyclones in the western Atlantic are projected to decrease in frequency (Colle et al., 2013), Booth et al. (2015) note that projected increases in coastal storm track density over the eastern U.S. could result in more frequent nor'easters, which are associated with high winds as well as high storm surges.

The recent damaging wind storms in New England in 2017 and 2019 also incorporated attributes of warm season storms. In the past two decades, heavy precipitation has increased across the northeastern U.S., associated primarily with tropical cyclones and

tropical moisture sources in September and October (Frei et al., 2015; Howarth et al., 2019; Huang et al., 2018, 2017). Major midlatitude cities along the eastern coast of North America such as Washington, D.C., New York City, and Boston are threatened every 2 to 4 years by tropical cyclones or those that have transitioned to extratropical cyclones (Hart and Evans, 2001). Tropical cyclones that transition can re-intensify and bring heavy rainfall and strong winds farther north. One example is Hurricane Sandy in October 2012, which transitioned to a post-tropical storm prior to landfall and brought high winds and waves to New England (Galarneau et al., 2013). Additionally, wind storms originating over the continent can interact with offshore tropical cyclones or their remnants, thereby providing additional moisture and energy for the wind storm. This was the case for the 30 October 2017 wind storm, which absorbed the remnants of Tropical Storm Philippe (NOAA/NCEI, 2017), and the 18-22 October 1996 wind storm, which tapped into moisture advected from Hurricane Lili (McNally et al., 2008). Model projections indicate that a future environment of warmer sea surface temperatures and lower wind shear in the eastern North Atlantic will be more conducive to tropical cyclone development and propagation. There could also be a greater proportion of tropical cyclones undergoing extratropical transition, resulting in extratropical cyclones of greater intensity and which produce heavier precipitation than in the current climate (Jung and Lackmann, 2019; Liu et al., 2017; Michaelis and Lackmann, 2019). Moreover, storm tracks for tropical and extratropical cyclones could shift poleward and closer to the eastern U.S. coast due to a more northerly polar jet and a northward and westward expansion of the subtropical high (Jiang and Perrie, 2007; Liu et al., 2017). These future scenarios imply not only an increase in the number of wind storms originating from the tropics, but also that mid-autumn wind storms, in general, will likely produce more heavy rainfall.

Another question of concern is whether the frequency and intensity of wind storms have changed in response to broader circulation patterns. The three unusually strong wind storms to affect the New England region in 2017 and 2019 occurred during an interval of

unprecedented autumn warmth in the Arctic (Overland et al., 2017, 2019). Previous studies (e.g., Francis and Vavrus, 2012, 2015) have suggested that Arctic Amplification – the disproportionate warming of Arctic surface temperatures compared to lower latitudes due to increased greenhouse gases and associated positive feedbacks from declining sea ice extent and snow cover – results in weakened zonal flow of the westerlies and higher amplitude Rossby waves. A "wavier" jet stream circulation has been linked to atmospheric blocking and increased extreme weather in the middle latitudes (Screen and Simmonds, 2014). However, the underlying dynamics associated with this phenomenon are still uncertain, as other studies have indicated that an increasing wave amplitude trend is sensitive to how atmospheric waves are defined, and the trend is not replicated by climate model simulations (Barnes et al., 2014; Blackport and Screen, 2020; Screen and Simmonds, 2013).

This study examines storm characteristics and changes in the frequency and intensity of mid-autumn (October – November) wind storms in New England to help inform future climate projections for the region. We first develop a climatology of wind storms using reanalysis data, gridded precipitation data, and surface station observations. We then identify trends in wind storm frequency and intensity (as measured sustained wind speeds and gusts), as well as other properties of the events such as the central sea-level pressure, sea-level pressure tendency, and the sea-level pressure gradient of the accompanying extratropical cyclone, and daily precipitation. In addition, we assess and compare the characteristics of stronger and weaker wind storms. These include the distribution of of the sea-level pressure tendencies (i.e., intensification/deintensification rates of associated extratropical cyclones), composite analyses of sea-level pressure and maximum 10-meter wind gusts for stronger and weaker wind storms, preferential storm tracks, and the prevailing wind direction of wind gusts. Section 4.2 details the methodology. The analysis results are described and discussed in Sections 4.3 and 4.4. A summary of our major conclusions is presented in Section 4.5.

4.2 Data and Methodology

This study utilizes two gridded datasets and one station observation dataset. Atmospheric data were extracted from the ECMWF Reanalysis version 5 (ERA5; ECMWF, 2019; Hersbach et al., 2020), a fifth generation reanalysis product and the successor to the ERA-Interim reanalysis. This reanalysis was chosen for its high spatial and temporal resolutions, with global variables available at 31 km grid cell resolution and hourly time outputs. Data were acquired for sea-level pressure (SLP), 10-meter maximum wind gusts, 10-meter zonal (u) and meridional (v) winds, and precipitation for October and November from 1979 to 2019. Maximum wind gusts in the reanalysis are derived from instantaneous model calculations within the preceding forecast integration. Precipitation data were obtained from the Parameter-Elevation Regressions on Independent Slopes Model (PRISM; Daly et al., 2008, 1994) time series dataset, a set of spatial climate data products for temperature, dew point temperature, vapor pressure, and precipitation. PRISM interpolates estimates of climate data to a 30 sec 2.5 min (~4km) resolution grid using station data, a digital elevation model, and other spatial data sets. Daily precipitation totals were used from 1981 to 2018. Surface observation data was obtained from NOAA's Integrated Surface Database (ISD; Smith et al., 2011) daily summaries database. The ISD consists of houly and synoptic weather observations from more than 35,000 stations worldwide, with some locations having data as far back as 1901. The daily summaries subset includes various daily mean and maximum values (based on Greenwich Mean Time), such as sea-level and station pressures, 10-meter sustained wind and gusts, temperature, and precipitation. Station data for daily maximum wind gusts, maximum sustained winds, and total accumulated precipitation were obtained for 15 stations in the states of Maine, New Hampshire, Vermont, Massachusetts, Rhode Island, and Connecticut (Fig. 4.1).

For this study, we identify wind storms using wind gust and sustained wind speed thresholds corresponding to the National Weather Service (NWS) Wind Advisory and High Wind Warning criteria (https://www.weather.gov/box/criteria). Wind storms were defined

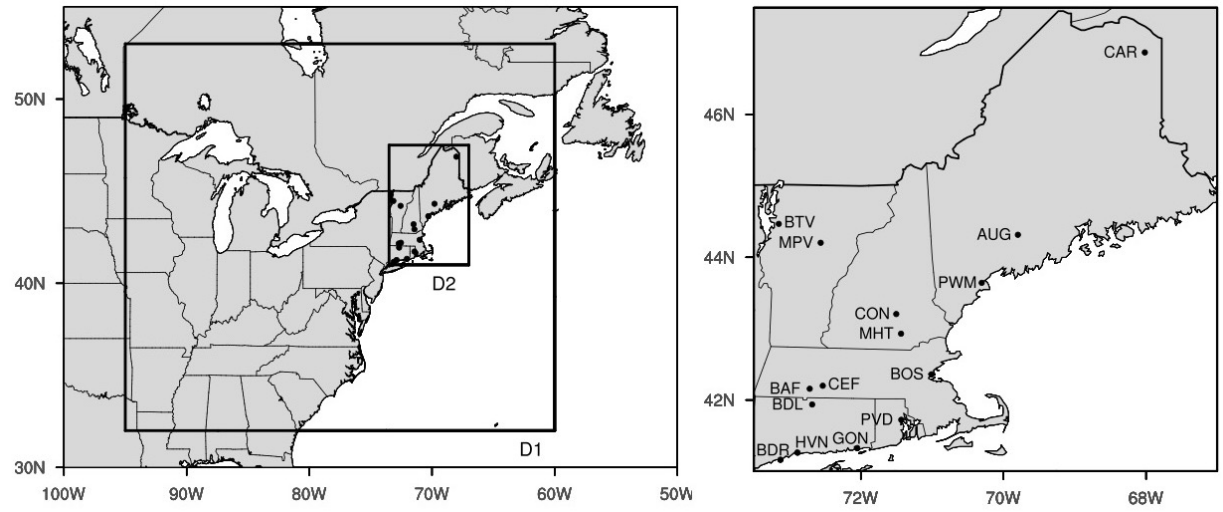

Figure 4.1: Domains for sea-level pressure (D1, left) and 10-meter wind gusts (D2, right) with the locations of observation stations. Surface stations include Augusta, ME (AUG); Barnes, MA (BAF), Hartford-Bradley, CT (BDL); Bridgeport, CT (BDR); Boston, MA (BOS); Burlington, VT (BTV); Caribou, ME (CAR); Chicopee Falls, MA (CEF); Concord, NH (CON); Groton-New London, CT (GON); New Haven, CT (HVN); Manchester, NH (MHT); Montpelier, VT (MPV); Providence, RI (PVD); and Portland, ME (PWM).

using the Wind Advisory Criteria as when the daily maximum wind gust was at or above 21 ms^{-1} (46 mph) or the daily maximum sustained wind speed (maximum observed 2-minute average wind speed) was at or above 14 ms^{-1} (31 mph). For observation-based wind storms, the criteria must be met at three or more stations. A subset of strong wind storms was defined using the NWS High Wind Warning criteria as days with maximum wind gusts of at least 26 ms^{-1} (58 mph) or maximum 2-minute sustained winds of at least 18 ms^{-1} (40 mph). Both the wind gust and sustained wind speed criteria were used for observations in order to produce a more complete climatology of events, as wind gusts are only recorded when wind speeds rapidly fluctuate by 10 knots (5.1 ms^{-1}) or more, but a wind storm event only needs to satisfy the threshold for at least one of the wind variables.

Two wind storm climatologies were created using the ERA5 reanalysis and PRISM precipitation datasets. For the first climatology, wind storms were identified using 3-hourly SLP and maximum wind gust fields over two domains (D1 and D2, Fig. 4.1). Within the larger domain, low-pressure centers were isolated by comparing the SLP of a given grid cell

with the eight grid cells surrounding it to see if the pressure of the central cell is lower than its neighbors, a commonly used approach (Ulbrich et al., 2009). Additional criteria were applied in order to isolate high-wind events over land that are associated with synoptic-scale features, as opposed to short-lived events or high winds confined to elevated terrain. A low center was designated as a wind storm if the maximum wind gusts for more than 20 grid cells within the inner domain were at or above the advisory or warning criteria. A land-sea mask was used to exclude wind values over water, and wind storms lasting < 12 hours were also excluded. Although these restrictions produce a smaller sample of wind storms (the number of identified approximately doubles using a 10 grid cell criteria), the additional "events" typically involve a few grid cells, often localized over mountain peaks, with maximum wind gusts just above the minimum criteria, and would unlikely result in substantial wind damage in the region. A second reanalysis climatology was created by applying the wind gust criteria to the grid cells corresponding to the approximate locations of the ISD surface stations. As with the observation-based climatology, the wind criteria must be met at three or more station locations.

The statistical analysis for the reanalysis- and observation-based wind storm climatologies consisted of assessing the frequency and intensity of wind storms for the period 1 October – 30 November inclusive, as well as the two months separately. Wind storm frequency was determined by counting the number of storms that occurred during the specified time period. Although wind storm intensity was defined by sustained winds and gusts, other storm characteristics were also assessed, including the central SLP of the low-pressure center, the 24-h normalized SLP tendency, the SLP gradient, and the average daily accumulated precipitation within the inner domain for the domain-level reanalysis-based climatology, and the daily total precipitation for the two station-level climatologies. SLP tendencies were calculated over a 24-h period centered on the time of maximum wind gusts, then normalized to a reference latitude of 46°N following Roebber (1989):

$$\Delta P_{46} = \frac{\Delta P_{\phi} sin46^{\circ}}{sin\phi}$$

where ΔP_{46} is the normalized, 24-h SLP tendency, ΔP_{φ} is the SLP tendency, and φ is the mean latitude of the low during the 24 h period. At 46°N, the threshold for a bomb cyclone is a drop in central pressure of at least 20 mb over 24 hours. SLP gradients were calculated by choosing the maximum difference between the central SLP value from the SLP 10 grid squares from the low in the four cardinal directions, which are normalized to 1000 km. The trends in these individual variables were identified using the ordinary linear regression slope and the Theil-Sen slope estimator (Sen, 1968; Theil, 1950), and the statistical significance of the trends were assessed at the 95% level using the Student's t-test and the Mann-Kendall trend test (Kendall, 1948; Mann, 1945). The Theil-Sen slope estimator represents how the median of the data changes linearly with time, and is a nonparametric alternative to the least squares regression – which represents how the mean of the data changes with time. The Mann-Kendall test is a commonly used non-parametric test for detecting statistically significant linear or non-linear trends in hydrological and meteorological time series (Romanić et al., 2015; Tabari et al., 2011). The null hypothesis is that there is no trend, while the alternative hypotheses are that there is a negative, positive, or non-null trend. This test is based on the ranks of observations and compares the relative magnitudes of data points as opposed to the data values themselves (Gilbert, 1987). The advantage of the Mann-Kendall test is that it is not affected by the distribution of the data and is less sensitive to outliers. The statistical analysis was performed using the NCAR Command Language (NCL) functions for linear regression and Mann-Kendall/Theil-Sen (NCAR, 2019).

4.3 Results

4.3.1 Trends

For the 1979-2019 study period, 44 wind storms are identified from the reanalysis in connection with a low-pressure system in proximity to New England. Wind storms more often occur in November, and the majority of October wind storms occur near the end of the month (Fig. 4.2). A greater number of wind storms are identified at the station-level from the reanalysis (82) and a smaller number from observations (35), likely due to stronger reanalysis wind gusts at surface stations along the coast. As a result, the number of strong storms, which correspond to the NWS's High Wind Warning criteria (wind gusts greater than 26 ms^{-1} or sustained winds greater than 18 ms^{-1}), constitutes less than half (45%) of all wind storms included in the station-level reanalysis-based climatology, while the number of strong storms are similarly dispersed among the domain-level reanalysis based (61%) and the station-level observation-based (54%) climatologies (Table 4.1). Thirteen wind storms from the domain-level climatology meet the criteria for a bomb cyclone, with seven of those storms resulting in wind gusts greater than 26 ms^{-1} over New England, indicating that the majority of wind storms in the region are not associated with bomb cyclones.

For the reanalysis- and observation-based climatologies, there are no significant positive or negative trends in overall wind storm frequency (Table 4.1). The lack of a significant positive or negative trend in the number of wind storms over time is partly reflective of the relatively small sample of events for the 41-year study period, with the number of storms generally ranges between zero and two during the two month period (Fig. 4.3). In examining the full length of the record, there appears to be greater year-to-year variability in the number of wind storms in the past two decades compared to the two decades prior. However, there is not a similarly marked difference in the frequency of bomb cyclones between the first half of the study period compared to the latter half.

The results of the storm intensity (sustained winds and wind gusts) and storm characteristic metrics (SLP, normalized SLP tendency, SLP gradient, precipitation)

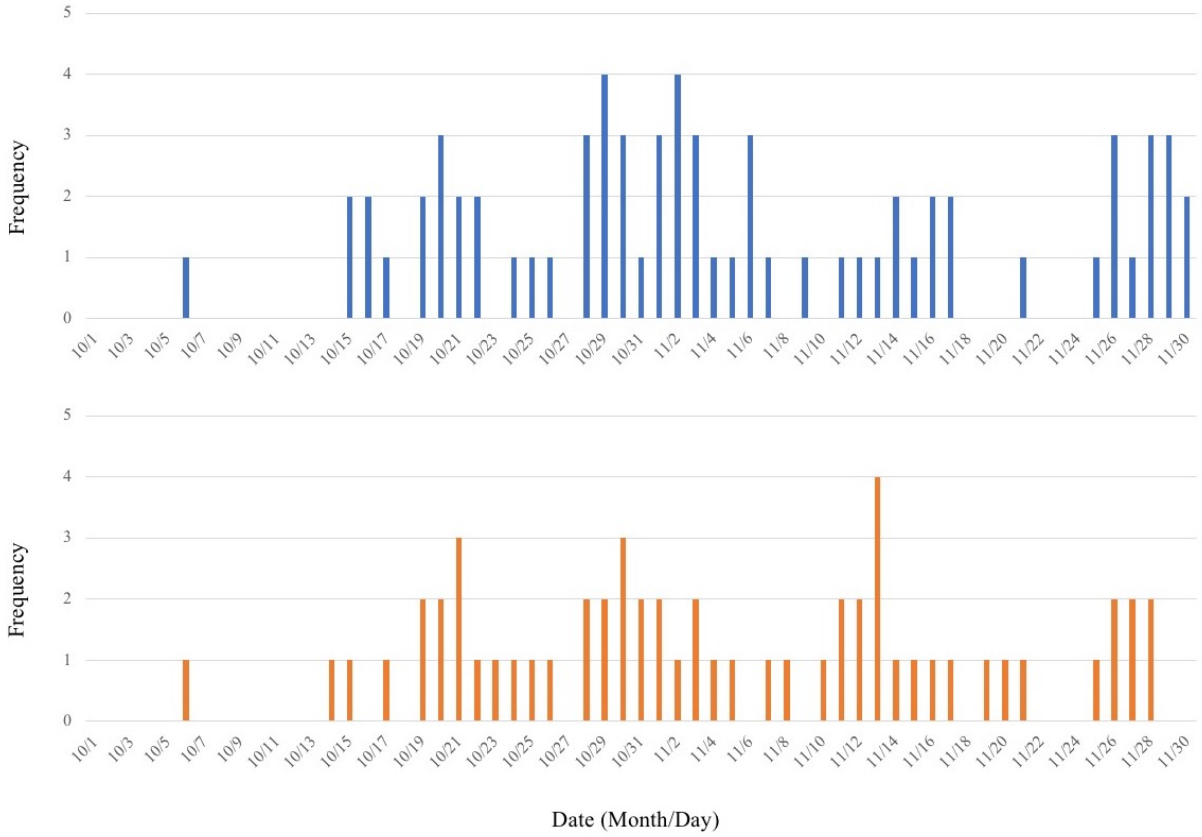

Figure 4.2: Distribution of all wind storms from the domain-level reanalysis-based climatology (top) and the station-level observation-based climatology (bottom).

indicate that there are few statistically significant trends present in more than one of the climatologies. There are no statistically significant trends in the domain-level reanalysis-based climatology (Table 4.2). However, there are statistically significant trends in precipitation identified from the two station-level climatologies. For the station-level reanalysis-based climatology, statistically significant positive trends are present for daily precipitation from strong October wind storms (Table 4.3). From the observation-based climatology, there are statistically significant positive precipitation trends for both categories of October wind storms as well as for the two month period overall for strong wind storms (Table 4.4).

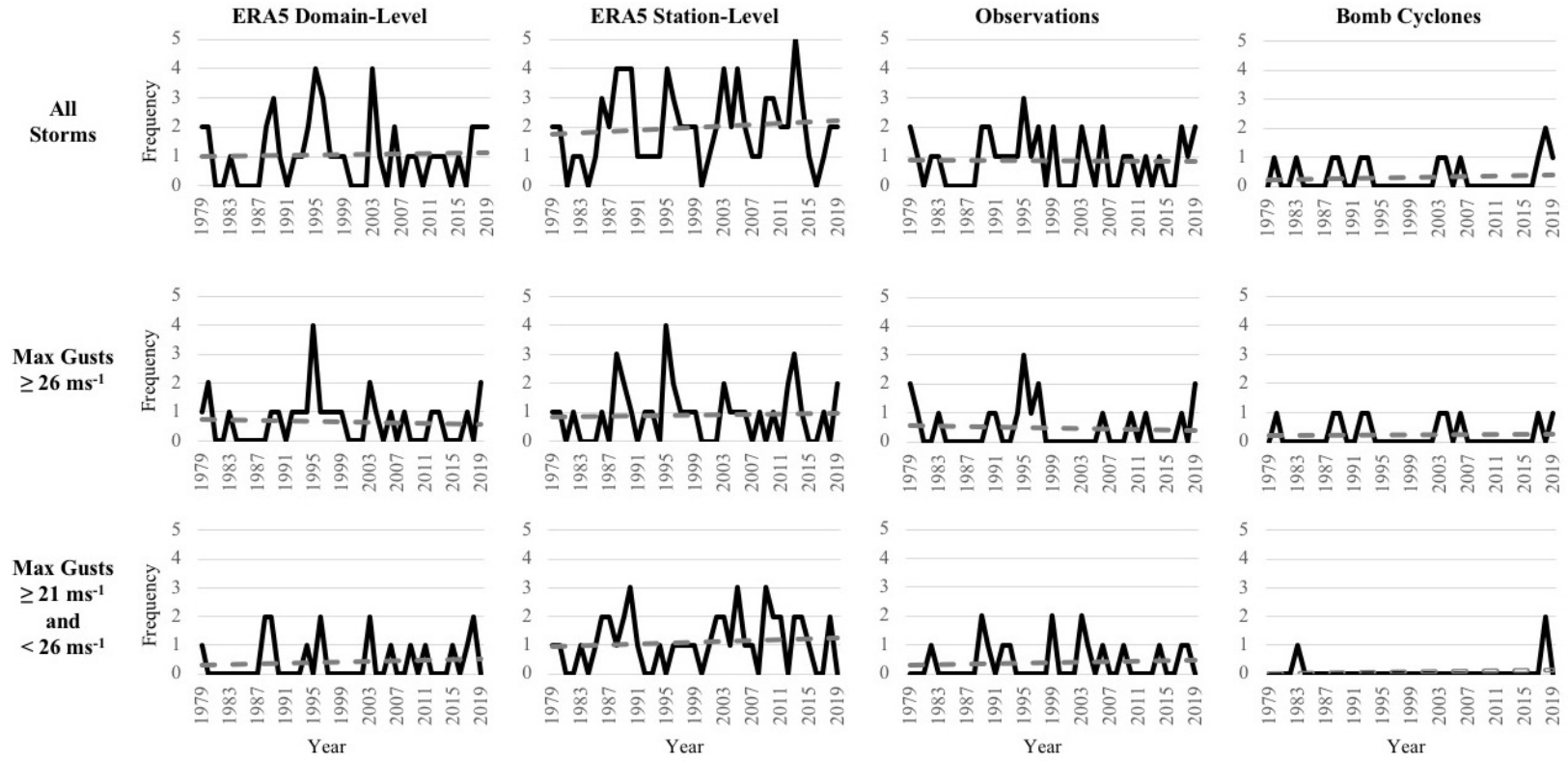

Figure 4.3: The frequency of wind storms over time for 1979-2019 from the domain-level reanalysis-based climatology (far left), the station-level reanalysis-based climatology (center left), the observation-based climatology (center right), and the number of wind storms classified as bomb cyclones from the domain-level reanalysis-based climatology (far right). The linear regression line is indicated in gray in each plot.

Table 4.1: Statistical analysis of wind-storm frequency (storms $year^{-1}$) for the reanalysis-based and station-based wind storm climatologies. Strong storms are those in which maximum wind gusts greater than 21 ms^{-1} (58 mi/h) or maximum sustained winds greater than 18 ms^{-1} (40 mi/h) are present. Bomb cyclones (BC) are wind storms where the 24-h SLP tendency is -20 hPa or lower. Statistically significant trends at the 95% level are bolded.

			Total	Linear Slope	Theil-Sen Slope
ERA5 Domain-Level	All	2 month	44	0.02	0.00
		Oct	18	0.02	0.00
		Nov	26	0.00	0.00
		BC	13	0.00	0.00
	Strong	2 month	27	0.01	0.00
		Oct	10	0.02	0.00
		Nov	17	0.00	0.00
		BC	10	0.00	0.00
ERA5 Station-Level	All	2 month	82	0.01	0.00
		Oct	35	0.02	0.00
		Nov	47	-0.01	0.00
	Strong	2 month	37	0.00	0.00
		Oct	16	0.01	0.00
		Nov	21	-0.01	0.00
ISD Station-Level	All	2 month	35	0.00	0.00
		Oct	15	0.00	0.00
		Nov	20	0.00	0.00
	Strong	2 month	19	-0.01	0.00
		Oct	11	0.00	0.00
		Nov	8	0.00	0.00

4.3.2 Storm Characteristics

In this section, the characteristics of winds storms included in the domain-level reanalysis-based climatology are examined, as well as how storm characteristics differ between the first half of the study period (1979-1999) and the second half (2000-2019), and between weak and strong wind storms. These characteristics include the intensification/deintensification rates of the extratropical cyclones, the composite SLP and wind gust fields for weak and strong wind storms, the spatial distribution of storm tracks, and the prevailing direction of high winds.

Table 4.2: Statistical analysis of wind-storm intensity for the domain-level reanalysis-based climatology. Statistical significance designated as in Table 4.1. Units are hPa $year^{-1}$ for sea-level pressure, hPa $(24h)^{-1}$ $year^{-1}$ for normalized sea-level pressure tendency, hPa $(1000km)^{-1}$ $year^{-1}$ for pressure gradient, ms^{-1} $year^{-1}$ for 10-meter wind gusts, and mm $year^{-1}$ for precipitation.

		Variable	Linear Slope	Theil-Sen Slope
All	2 month	SLP	0.02	0.07
		SLPtend	0.02	0.02
		SLPgrad	0.02	-0.15
		Max Gust	-0.01	-0.02
		PRE	0.03	0.00
	Oct	SLP	-0.16	-0.20
		SLPtend	-0.01	0.00
		SLPgrad	0.14	0.00
		Max Gust	0.04	0.17
		PRE	0.01	-0.30
	Nov	SLP	0.15	0.21
		SLPtend	0.10	0.07
		SLPgrad	-0.01	0.35
		Max Gust	-0.05	-0.08
		PRE	0.01	-0.08
Strong	2 month	SLP	-0.34	0.00
		SLPtend	0.02	0.04
		SLPgrad	0.04	-0.27
		Max Gust	-0.02	0.00
		PRE	-0.17	0.00
	Oct	SLP	-0.14	-0.33
		SLPtend	0.00	0.00
		SLPgrad	0.02	0.00
		Max Gust	-0.04	-0.03
		PRE	0.20	-0.57
	Nov	SLP	0.04	0.23
		SLPtend	0.03	0.01
		SLPgrad	-0.04	0.63
		Max Gust	-0.02	0.02
		PRE	-0.21	-0.24

Table 4.3: As in Table 4.2, only for the station-level reanalysis-based climatology.

		Variable	Linear Slope	Theil-Sen Slope
All	2 month	Max Gust	0.00	-0.02
		Max Wind	0.00	0.01
		PRE	-0.06	-0.14
	Oct	Max Gust	0.00	0.00
		Max Wind	0.01	0.04
		PRE	0.22	0.32
	Nov	Max Gust	-0.01	-0.02
		Max Wind	0.03	0.04
		PRE	-0.35	-0.51
Strong	2 month	Max Gust	0.03	0.04
		Max Wind	0.00	0.00
		PRE	0.44	-0.07
	Oct	Max Gust	0.03	0.18
		Max Wind	-0.05	0.09
		PRE	0.30	**0.25**
	Nov	Max Gust	0.05	0.08
		Max Wind	0.02	0.14
		PRE	-0.52	-0.67

Table 4.4: As in Table 4.2, only for the station-level observation-based climatology.

		Variable	Linear Slope	Theil-Sen Slope
All	2 month	Max Gust	0.01	0.00
		Max Wind	-0.01	-0.01
		PRE	0.38	0.65
	Oct	Max Gust	0.01	**0.01**
		Max Wind	-0.01	-0.07
		PRE	**0.68**	2.47
	Nov	Max Gust	0.00	0.01
		Max Wind	-0.01	-0.01
		PRE	0.05	0.19
Strong	2 month	Max Gust	-0.05	-0.13
		Max Wind	-0.02	-0.02
		PRE	**0.65**	1.77
	Oct	Max Gust	-0.04	-0.23
		Max Wind	0.01	-0.07
		PRE	**0.71**	3.56
	Nov	Max Gust	-0.01	-0.02
		Max Wind	-0.06	-0.01
		PRE	0.24	0.00

The first storm characteristic is the intensification (and deintensification) rates for the extratropical cyclones associated with wind storms. The distributions of normalized 24-h SLP tendency, which is calculated over a 24-hour period centered on the time of maximum wind gusts, are shown in Figure 4.4. Overall, the low-pressure systems tend to intensify during high-wind events in New England. The distribution for SLP tendencies for all wind storms has two peaks, with a higher peak at weakly negative or zero tendencies and a lower peak at negative tendencies falling within the criteria for bomb cyclones. The average 24-h SLP tendency for the sample of strong wind storms is -13.6 hPa and -8.3 hPa for the sample of weaker wind storms. The peak SLP tendency for strong wind storms is one category to the left of the peak SLP tendency for weak wind storms; however, the SLP tendencies for weak wind storms are concentrated towards less negative and more positive values while SLP tendencies for strong storms are more evenly distributed across highly negative, less negative, and positive tendencies. When examining the SLP tendency distributions for the first and second half of the study period (Fig. 4.5), the general pattern is a shift towards lower SLP tendencies, and thus higher intensification rates, for all wind storms. Also, the number of bomb cyclones stays the same or slightly increases for both weak and strong wind storms, despite a decrease in the overall number of wind storms between the first and second half of the study period.

The second storm characteristic is the average, or composite, SLP and wind fields associated with stronger and weaker wind storms. Figure 4.6 shows the composites for strong wind storms and all other wind storms, respectively, at the time of maximum wind gusts, as well as twelve hours before and after. The average storm track for both wind storm categories is similar, with the center of the low approaching New England from the southwest and then passing to the north of the region, which is consistent with previous studies (e.g., Booth et al., 2015; Niziol and Paone, 2000). The strongest surface winds across New England tend to be out of the south or southeast, and the strongest wind gusts occur to the southeast of the low center. Notable differences between the two sets of

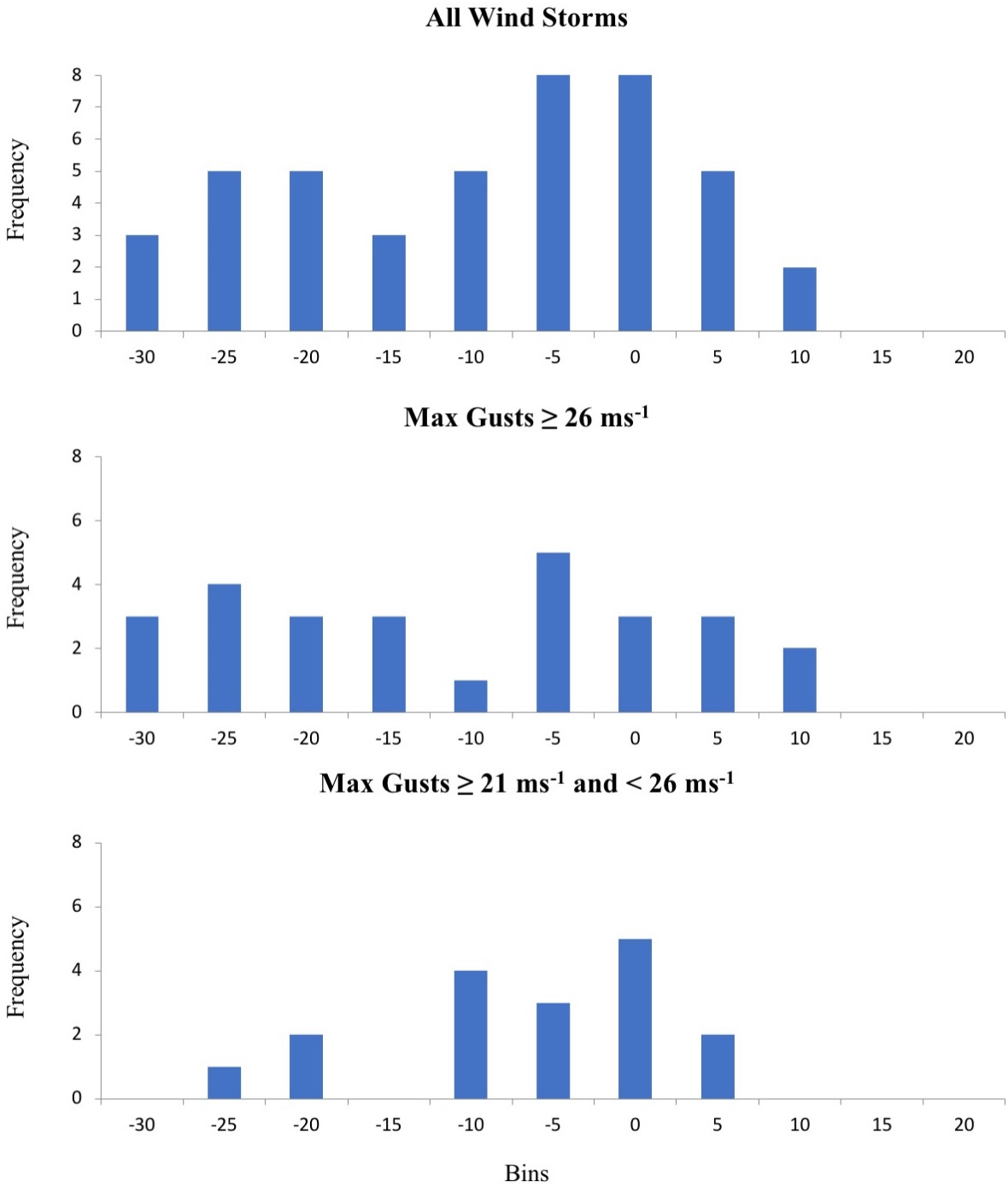

Figure 4.4: Normalized 24-h sea-level pressure tendency distributions for wind storms from the domain-level reanalysis-based climatology. Bins are at intervals of 5 hPa $(24\,h)^{-1}$ with the upper bounds labeled (i.e. $<$ -30, -30 to -25, -25 to -20, etc.).

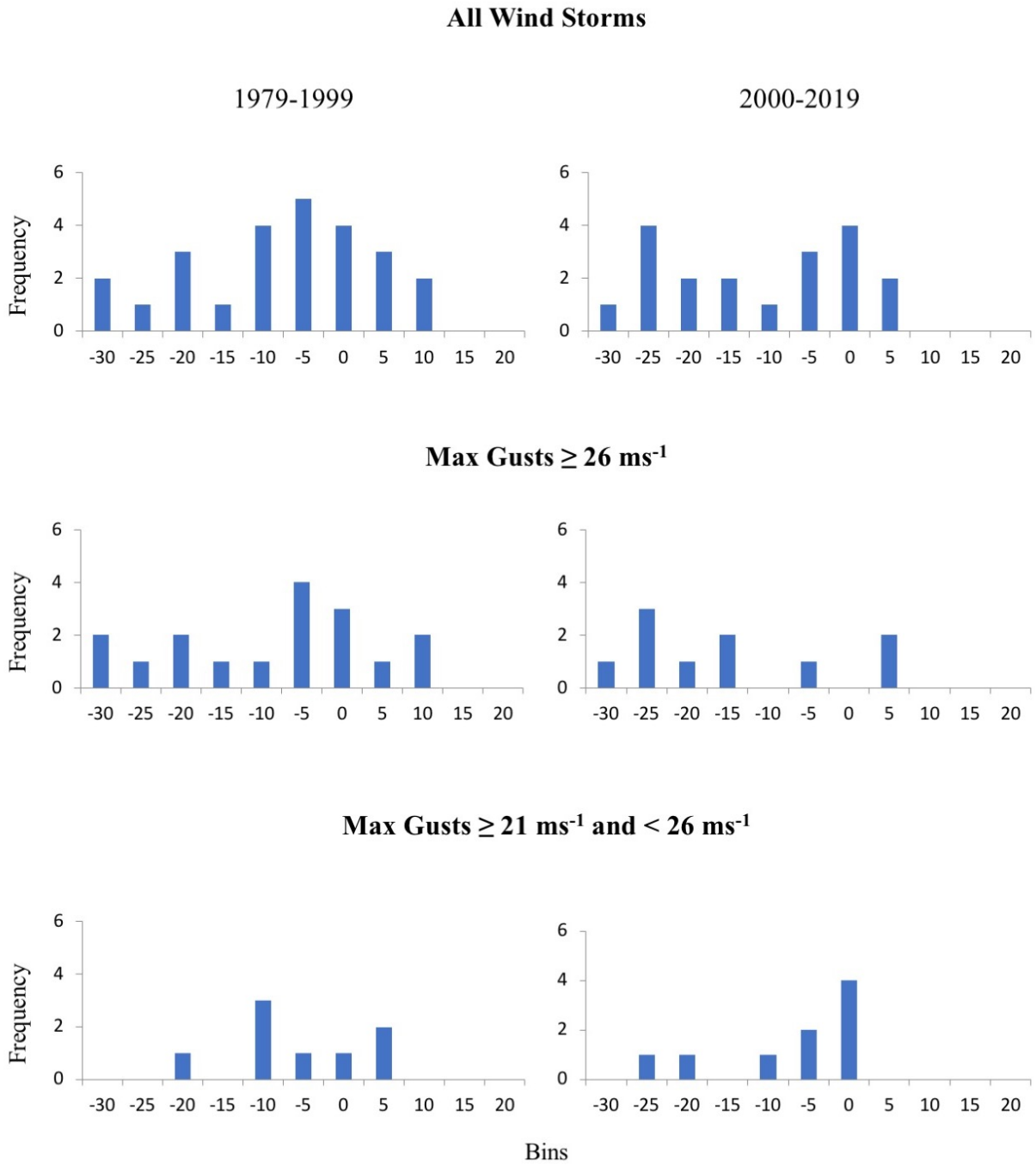

Figure 4.5: As in Figure 4.4 for the first half (1979-1999) and second half (2000-2019) of the study period.

composites are that the average low system associated with strong wind storms tends to be more compact and have a lower central SLP value.

The third storm characteristic is the preferred storm tracks of wind storms. Although the composites indicate a prevalent southwest-to-northeast path over the Great Lakes, it is also important to consider other major storm tracks. From the domain-level climatology, we identify three categories of storm tracks. The first category is the southwest-to-northeast track over the Great Lakes previously shown in the composites (Fig. 4.7a), the second category includes lows originating in closer proximity to the East Coast, such as nor'easters (Fig. 4.7b), and the third category includes tracks over the western Great Lakes with more south-to-north trajectories towards Hudson Bay (Fig. 4.7c). The first two categories each account for approximately a third (15 and 14 winds storms, respectively) of all wind storms, while the third category accounts for 22% (10) of wind storms. Four storms had paths that did not fit any of the categories. Bomb cyclones are more common in the second (7) and the first storm track categories (6) than the third category (2).

The last storm characteristic is the prevailing direction of maximum wind gusts in the region. Although these high-wind events are associated with an extratropical cyclone, previous studies and the composite analysis show that the highest winds are more closely tied to the location of a frontal boundary. To examine the prevailing wind direction during the wind storms, wind rose for several station locations are shown in Figure 4.8. While the direction of wind gusts varies for some stations along the southern New England coast and southern New Hampshire, the strongest wind gusts, as well as event winds overall, tend to be out of the south or southeast (wind a lesser fraction out of the east or northeast). The prevailing wind directions indicated by the wind rose and the composites are consistent with previous studies indicating that the highest winds are located in the southeast quadrant of the low ahead of a cold front.

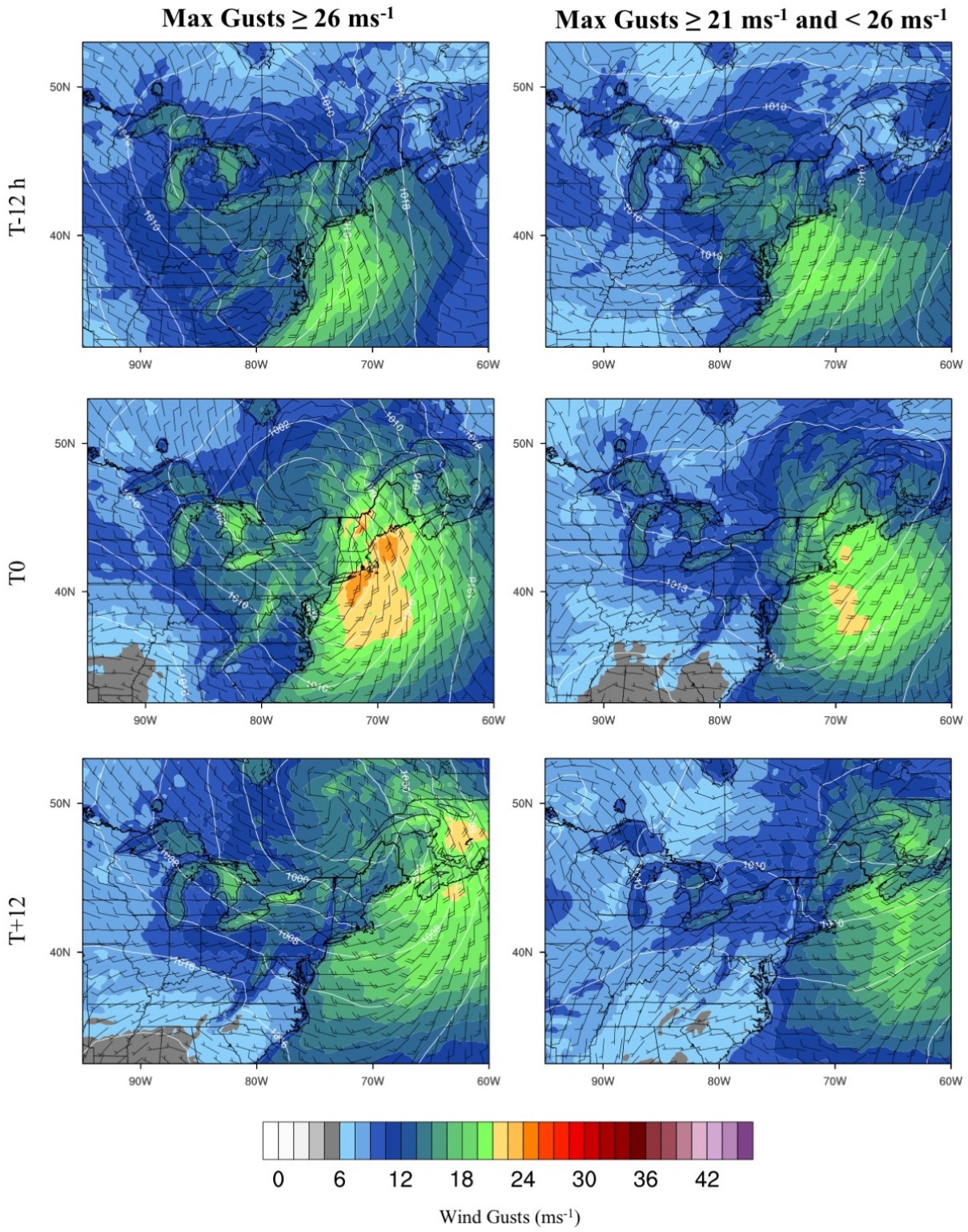

Figure 4.6: Sea-level pressure (in hPa) and maximum 10-meter wind gust (in ms^{-1}) composite analysis of strong wind storms (left, 27 total) and all other wind storms (right, 17 total) from the domain-level reanalysis-based climatology. Composites are shown for the time of the maximum wind gusts within the New England domain (T0), and for twelve hours before (T-12) and after (T+12).

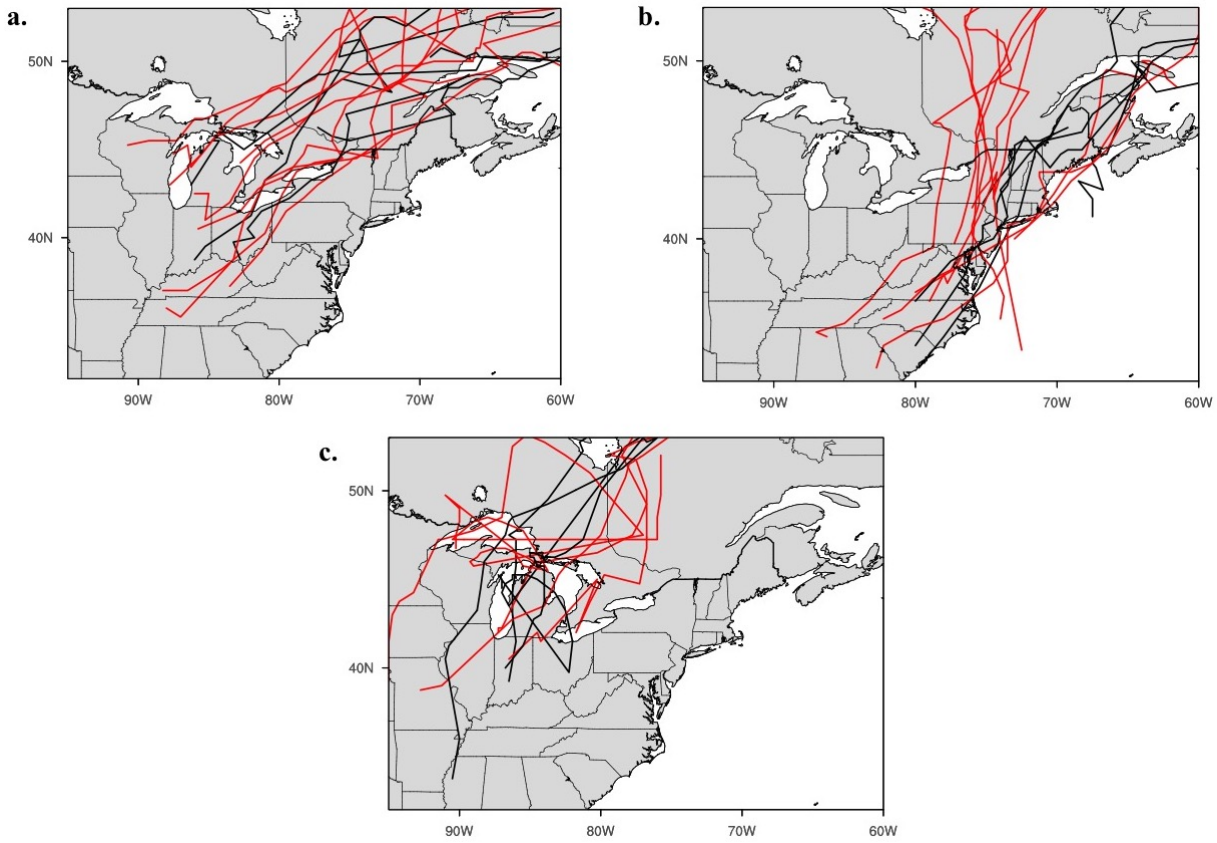

Figure 4.7: Storm tracks organized by category: (a) type 1, (b) type 2, and (c) type 3. Tracks for strong wind storms are in red, all other tracks are in black.

4.4 Discussion

The results of this study support and expand upon the findings from previous studies on the characteristics of high-wind events associated with extratropical cyclones in the region. The composite analysis shows that high-wind events in New England associated with extratropical cyclones typically approach from the southwest and pass to the north of the region, and the wind rose indicate that the strongest winds tend to be out of the south or southeast. This storm track and prevailing wind direction are consistent with the results of previous wind storm studies (e.g., Booth et al., 2015), which indicate that the southeast quadrant of a low is where the strongest winds are located. However, there are many examples of wind storms that have characteristics differing from the composite. Low-pressure systems with more coastal storm tracks (such as nor'easters) occur at an

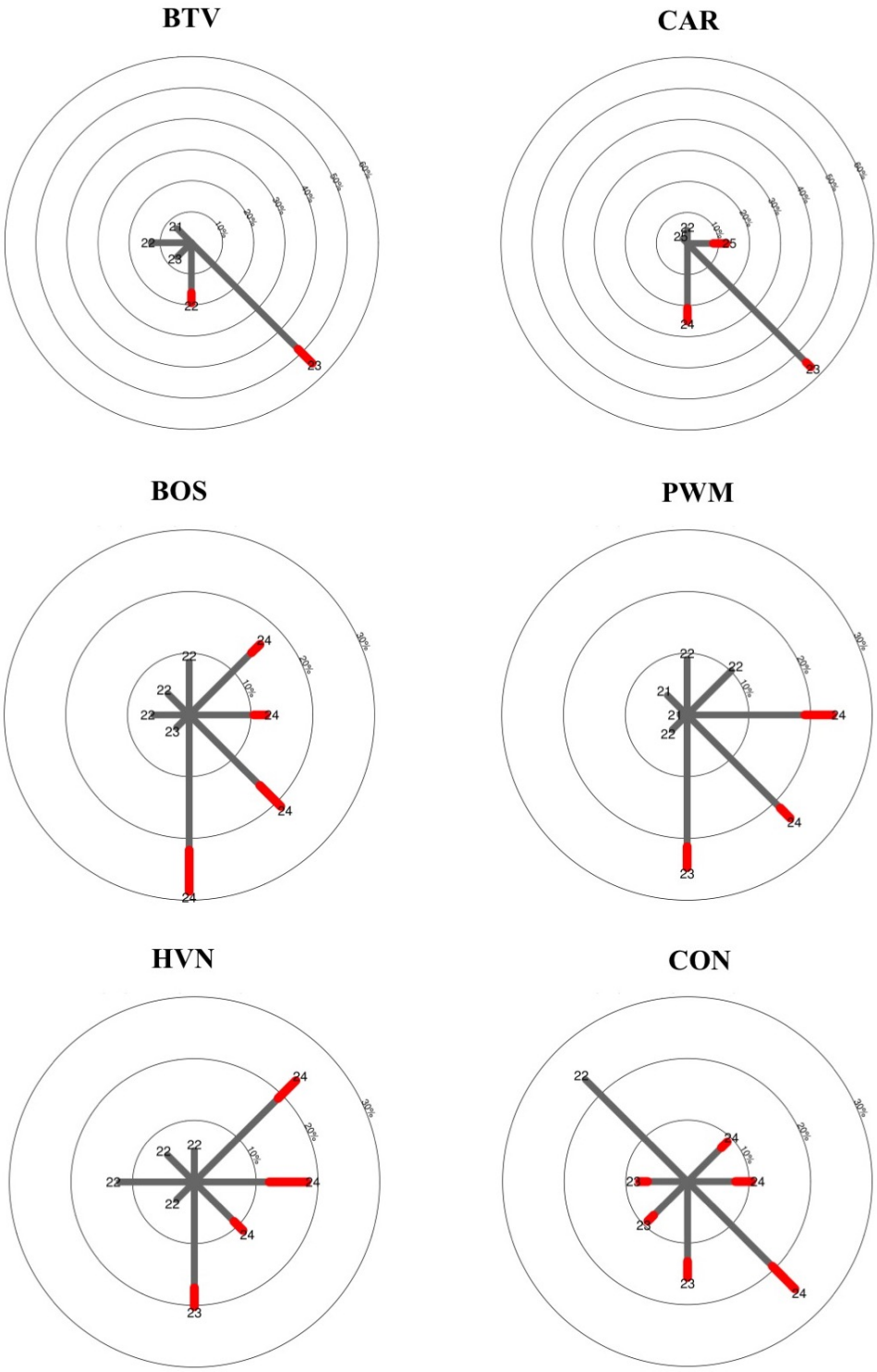

Figure 4.8: Wind rose for Burlington, VT (BTV); Caribou, ME (CAR); Boston, MA (BOS); Portland, ME (PWM); New Haven, CT (HVN); and Concord, NH (CON). Concentric circles indicate the frequency (%) of wind gusts during wind storms, with the average wind gust (in ms^{-1}) for each direction labeled at the end of the "petal". The frequency of wind gusts between 21 ms^{-1} and 26 ms^{-1} are indicated in gray, and the frequency of wind gusts at or above 26 ms^{-1} are indicated in red.

equal frequency as the Great Lakes storm track indicated by the composite, although the lows tend to pass to the north of the region as well. The majority of wind storms that fall within the third storm track category are considered strong wind storms, and yet the lows do not approach New England at all. Additionally, the strongest wind storms are not always associated with very low central pressures or bomb cyclones. Other factors, such as the pressure gradient, are also important.

It is difficult to determine whether changes large-scale circulation patterns have had a detectable effect on wind storms in New England, as our results overall do not indicate a statistically significant change in wind storm frequency or intensity. This outcome could relate to the relative brevity of the record, as the small sample of storms makes identifying a statistically significant trend from interannual variability difficult. Despite the lack of statistically significant temporal trends in overall wind storm frequency or wind intensity, this study illuminates other aspects which could be important when projecting damage from future wind storms. There are indications that at the surface stations used in this analysis, strong wind storms (i.e., events which meet NWS High Wind Warning criteria) in October are associated with higher rainfall accumulations than at the beginning of the study period. Although high winds are the main characteristic of wind storms, heavy rainfall can also occur with these events. As previous studies (e.g., Howarth et al., 2019; Huang et al., 2018) have shown that tropical cyclones and their remnants have substantially contributed to a rise in extreme precipitation in the northeastern U.S, we cross-referenced dates from the wind storm climatologies with the National Hurricane Center's North Atlantic hurricane database version 2 (HURDAT2; Landsea and Franklin, 2013) to identify wind storms with tropical origins. Only three wind storms from the domain-level climatology were associated with tropical cyclones which transitioned to extratropical cyclones before reaching New England: Josephine (8 October 1996), Noel (3 November 2007), and Sandy (29-30 October 2012). However, tropical cyclones can also help strengthen wind storms of extratropical origin. At least two wind storms, occurring on

30 October 2017 and between 18-22 October 1996, interacted with offshore tropical systems and resulted in heavy rainfall in New England. Additionally, future shifts in storm tracks could result in additional damage from storm surges associated with wind storms. Extratropical cyclones with coastal storm tracks, such as nor'easters, can cause substantial coastal flooding and beach erosion (Dolan and Davis, 1992). This storm track is a common one for New England wind storms, and a projected increase in storms following this path could not only result in more high-wind events for the region, but also greater damage along the coast. Future work is suggested to more thoroughly examine the roles of tropical moisture sources and storm tracks in projections of New England wind storms.

There are challenges associated with the study of wind storms and predictions for storm damage in the future. One major difficulty is developing a single, precise definition for "wind storm". In this study we apply wind criteria used by the NWS, an approach commonly used by other studies (Booth et al., 2015; Lacke et al., 2007; Niziol and Paone, 2000). However, it is difficult to determine how to apply the wind criteria spatially and temporally, and do to so uniformly at both the station level and at the domain level. For the domain-level reanalysis climatology, additional criteria are utilized in order to isolate high-wind events that are associated with synoptic-scale features and not local topographical features. Although the criteria limit the number of identified wind storms, the additional "events" often involve a few grid cells with maximum wind gusts just above the minimum criteria, and would unlikely result in substantial wind damage in the region. Similar criteria are more difficult to apply to station observations, as the values are for daily maximum values and long-term automated weather variables are available for a limited number of locations in New England. The requirement that sustained winds and gusts must meet the criteria at multiple stations has a similar effect on the sample size as the grid cell criteria, although the location and density of surface stations has a notable effect on how many and which wind storms are included in the dataset.

Another major challenge is predicting how changes in extratropical cyclone intensity translates into wind damage. Although the central pressure is a common measure of extratropical cyclone intensity, it is a combination of factors (central SLP, SLP gradient, storm track) that result in high-wind events over a given location. For example, Booth et al. (2015) noted that extratropical cyclones associated with the strongest winter winds in the northeastern U.S. are not necessarily the strongest overall. Instead, it is important to consider the location of the strongest winds associated with the low with respect to the region of interest. Furthermore, high sustained winds or wind gusts do not guarantee that wind damage will occur (although the risk of damage increases), and wind damage can occur at wind speeds below the criteria used by the NWS. Modeling studies show that forest damage can begin at wind speeds as low as 10 ms^{-1} (Gardiner et al., 2000; Peltola et al., 1999). Other studies have used wind reports to compare damaging and non-damaging extratropical cyclones (Angel and Isard, 1998), or to produce wind storm climatologies (Lacke et al., 2007); however, this method has its own limitations, such as the lack of wind reports outside of population centers as well changing reporting methods over time and among NWS offices (Doswell et al., 2005). Additionally, other factors can increase the risk of wind damage that are only attributable to wind storms. Heavy rainfall from tropical and extratropical cyclones not associated with high winds during these months increases the risk of flooding and tree damage due to windthrow. Other environmental stresses such as drought, heat, disease, and insect infestations can weaken trees and increase the risk of wind damage. For example, drought conditions across Maine were a contributing factor to the large number of downed trees during the 30 October 2017 wind storm (Whittle, 2017). The combination of weather, climate, and environmental factors ultimately determines the resulting damage from these events.

4.5 Chapter Summary

This study examines the frequency and intensity of mid-autumn wind storms in New England and their characteristics. Wind storms are identified separately from the ERA5 reanalysis and ISD observation dataset using the NWS's Wind Advisory and High Wind Warning criteria. From the trend analysis, we find little evidence that wind storms have become stronger in terms of central surface pressure or wind speeds, although there are indications that strong October wind storms in the past two decades are associated with more precipitation than October storms from earlier in the record. The increased precipitation could be connected to the increased moisture transport associated with tropical cyclones and their remnant circulations, although to what degree is beyond the scope of this study. Our results also show that extratropical cyclones associated with mid-autumn high-wind events in New England typically travel from southwest-to-northeast with three preferred storm tracks. Although strong wind storms are often characterized by lower surface pressure or rapidly intensifying bomb cyclones, the intensity of an extratropical cyclone itself is not the only predictor of a high-wind event in the New England region, and the damage that they produce is a function of many factors. These include the local climatology, such as the frequency of heavy rainfall events, and the presence of environmental factors such as drought and heat stress. All such factors can increase the risk of damage from wind storms, and highlight the various ways in which climate change can impact storm severity.

CHAPTER 5

SUMMARY

Extratropical cyclones and the frontal processes associated with them are a substantial instigator of severe weather events in the USNE. These weather phenomena provide an array of challenges to a many stakeholders in the region: homeowners, business owners, farmers, forest managers, utility companies, and policy makers. This dissertation focuses on three topics pertaining to the investigation and effects of severe weather associated with extratropical cyclones.

In Chapter 2, the sensitivity of the WRF mesoscale model to several model setup factors is evaluated for a case study of the New England ice storm of 21-23 December 2013. The results show that, while the spatially and temporally averaged statistics for near-surface variables (2-meter temperature, 10-meter wind speed and direction, precipitation) are consistent with those of select ice-storm case studies, these variables are highly sensitive to the model configuration when examined at the station level. No single model configuration produces the most robust solution for all variables or station locations, although the TEMF scheme generally yields model output with the least realism. In all, the main finding is that careful model sensitivity testing and extensive validation are necessary components for minimizing model-based biases in simulations of ice storms.

In Chapter 3, it is shown that the recent increase in summer precipitation amount occurs in conjunction with more frequent high pressure blocking over Greenland (increased GBI) and an associated increasingly negative NAO, particularly during a period of exceptionally high GBI and low NAO values from 2007 to 2013. The occurrence of these patterns in summer has been previously identified in connection with southward shifted storm tracks and wet conditions across the eastern North Atlantic. Over the western North Atlantic and USNE, the circulation shifts are shown to be related to enhanced rainfall due to southerly wind anomalies and increased moisture transport into the USNE. This link

highlights the importance of adequately depicting circulation changes within climate models, as the current generation of models are unable to skillfully replicate the seasonal cycle and observed historical trends in precipitation across the USNE, as well as trends in Greenland blocking.

In Chapter 4, recent wind storm frequency and intensity are explored by utilizing reanalysis and station-based meteorological observations onward from 1979. The results do not show a statistically significant increase in the overall frequency of mid-autumn wind storms, nor their intensity with respect to central pressure or surface wind speeds. However, there is a statistically significant trend toward increasing precipitation accompanying wind storms with maximum 10-meter wind gusts greater than 26 ms-1 (58 mph). While stronger high-wind events tend to be associated with lower central sea-level pressure values and substantial intensification rates, the intensity of the event is not solely predicated on the intensity of the associated extratropical cyclone. Other characteristics of the cyclones, such as the storm track and the pressure gradient, as well as the local climatology and environmental factors (e.g., drought) could potentially increase the risk of wind damage in a warming world.

The results of this dissertation highlight the complexities of forecasting precipitation and storm damage, both in the short-term and long-term. Although this work examines several types of weather events and at different time scales, there are common themes among the topics. A recurring theme is the importance of spatial scale in weather and climate predictions. State-of-the-art dynamical models are able to replicate the general circulation patterns at the global scale; however, forecasting at the regional and local scale is more challenging due to a greater sensitivity to changes in large-scale circulation as well as the effects of sub-grid scale processes. This is especially difficult for predictions that require high precision, as well as spatial and temporal resolution. As computer models are heavily relied upon for weather forecasting and as a tool for studying past, present, and

future climate, it is important to recognize their limitations and to view model output critically.

The findings of this dissertation lend to multiple research avenues that could be further pursued. First, additional WRF simulations could investigate whether the observed model tendencies for the December 2013 case study also occur in other ice storm simulations. These subsequent tests can include other physics parameterizations, such as radiation and cloud microphysics, as well as other case study storms. Second, subsequent research could further examine the teleconnection between Greenland blocking and summer precipitation in the USNE by comparing summer circulation and precipitation patterns over the North Atlantic for high and low GBI years, both prior to and following the 2003 precipitation rise. And finally, additional inquiry into New England wind storms could concentrate on extending the reanalysis-based climatology (e.g., ERA5 is expected to be extended to 1950) or further investigate the role of tropical moisture sources and extratropical transition, as well as coastal flooding and storm surges, in the extent of storm damage for recent wind storms.

REFERENCES

Agel, L., Barlow, M., Colby, F., Binder, H., Catto, J. L., Hoell, A., & Cohen, J. (2019). Dynamical analysis of extreme precipitation in the US northeast based on large-scale meteorological patterns. *Climate Dynamics*, *52*(3), 1739–1760. https://doi.org/10.1007/s00382-018-4223-2

Agel, L., Barlow, M., Feldstein, S. B., & Gutowski, W. J. (2018). Identification of large-scale meteorological patterns associated with extreme precipitation in the US northeast. *Climate Dynamics*, *50*(5), 1819–1839. https://doi.org/10.1007/s00382-017-3724-8

Agel, L., Barlow, M., Qian, J.-H., Colby, F., Douglas, E., & Eichler, T. (2015). Climatology of daily precipitation and extreme precipitation events in the northeast united states. *Journal of Hydrometeorology*, *16*(6), 2537–2557. https://doi.org/10.1175/JHM-D-14-0147.1

Angel, J. R., & Isard, S. A. (1998). The frequency and intensity of great lake cyclones. *Journal of Climate*, *11*(1), 61–71. https://doi.org/10.1175/1520-0442(1998)011<0061:TFAIOG>2.0.CO;2

Angevine, W. M., Jiang, H., & Mauritsen, T. (2010). Performance of an eddy diffusivity–mass flux scheme for shallow cumulus boundary layers. *Monthly Weather Review*, *138*(7), 2895–2912. https://doi.org/10.1175/2010MWR3142.1

Arnold, D. (2009). *An ice accretion and wind load forecasting system for power transmission networks using numerical weather prediction* (Master's Thesis). University of Alberta. Edmonton, Alberta. Retrieved from ProQuest Dissertations Theses Global. (305059006).

Ashley, W. S., & Black, A. W. (2008). Fatalities associated with nonconvective high-wind events in the united states. *Journal of Applied Meteorology and Climatology*, *47*(2), 717–725. https://doi.org/10.1175/2007JAMC1689.1

Banks, R. F., Tiana-Alsina, J., Baldasano, J. M., Rocadenbosch, F., Papayannis, A., Solomos, S., & Tzanis, C. G. (2016). Sensitivity of boundary-layer variables to PBL schemes in the WRF model based on surface meteorological observations, lidar, and radiosondes during the HygrA-CD campaign. *Atmospheric Research*, *176-177*, 185–201. https://doi.org/10.1016/j.atmosres.2016.02.024

Barlow, M. (2011). Influence of hurricane-related activity on north american extreme precipitation. *Geophysical Research Letters*, *38*(4). https://doi.org/10.1029/2010GL046258

Barnes, E. A., Dunn-Sigouin, E., Masato, G., & Woollings, T. (2014). Exploring recent trends in northern hemisphere blocking. *Geophysical Research Letters*, 638–644. https://doi.org/10.1002/2013GL058745

Barry, E. (2019). Northeast 'bomb cyclone': Powerful winds knock out power to 500,000. *The New York Times*. Retrieved March 17, 2020, from https://www.nytimes.com/2019/10/17/us/northeast-bomb-cyclone.html

Baumgardt, D. (1999). *Wintertime cloud microphysics review*. National Weather Service, La Crosse, WI. http://www.crh.noaa.gov/arx/micrope.html

Birkel, S. D., & Mayewski, P. A. (2018). *Coastal maine climate futures*. Climate Change Institute, University of Maine. Orono, ME. https://climatechange.umaine.edu/2018/11/08/coastal-maine-climate-futures-s-birkel/

Blackburn, M., Methven, J., & Roberts, N. (2008). Large-scale context for the UK floods in summer 2007. *Weather*, *63*(9), 280–288. https://doi.org/10.1002/wea.322

Blackport, R., & Screen, J. A. (2020). Insignificant effect of arctic amplification on the amplitude of midlatitude atmospheric waves. *Science Advances*, *6*(8), eaay2880. https://doi.org/10.1126/sciadv.aay2880

Booth, J. F., Rieder, H. E., Lee, D. E., & Kushnir, Y. (2015). The paths of extratropical cyclones associated with wintertime high-wind events in the northeastern united states. *Journal of Applied Meteorology and Climatology*, *54*(9), 1871–1885. https://doi.org/10.1175/JAMC-D-14-0320.1

Brogan, B. (2014). FEMA denies disaster funding to maine for december 2013 ice storm. *Bangor Daily News*. Retrieved July 2, 2018, from https://bangordailynews.com/2014/04/03/business/fema-denies-disaster-funding-to-maine-for-december-2013-ice-storm/

Brown, P. J., Bradley, R. S., & Keimig, F. T. (2010). Changes in extreme climate indices for the northeastern united states, 1870–2005. *Journal of Climate*, *23*(24), 6555–6572. https://doi.org/10.1175/2010JCLI3363.1

Carvalho, D., Rocha, A., Gómez-Gesteira, M., & Santos, C. (2012). A sensitivity study of the WRF model in wind simulation for an area of high wind energy. *Environmental Modelling & Software*, *33*, 23–34. https://doi.org/10.1016/j.envsoft.2012.01.019

Chou, M.-D., & Suarez, M. J. (1999). *A solar radiation parameterization for atmospheric studies*. NASA Tech. Memo. 104606. https://ntrs.nasa.gov/archive/nasa/casi.ntrs.nasa.gov/19990060930.pdf

Cohen, A. E., Cavallo, S. M., Coniglio, M. C., & Brooks, H. E. (2015). A review of planetary boundary layer parameterization schemes and their sensitivity in simulating southeastern u.s. cold season severe weather environments. *Weather and Forecasting*, *30*(3), 591–612. https://doi.org/10.1175/WAF-D-14-00105.1

Colle, B. A., Zhang, Z., Lombardo, K. A., Chang, E., Liu, P., & Zhang, M. (2013). Historical evaluation and future prediction of eastern north american and western atlantic extratropical cyclones in the CMIP5 models during the cool season. *Journal of Climate*, *26*(18), 6882–6903. https://doi.org/10.1175/JCLI-D-12-00498.1

Collow, A. B., Bosilovich, M. G., & Koster, R. D. (2016). Large-scale influences on summertime extreme precipitation in the northeastern united states. *Journal of Hydrometeorology*, *17*(12), 3045–3061. https://doi.org/10.1175/JHM-D-16-0091.1

Collow, A. B., Bosilovich, M. G., & Koster, R. D. (2017). *Synoptic scale influences on increasing summertime extreme precipitation events in the northeastern united states*. NASA GMAO Research Brief. https://gmao.gsfc.nasa.gov/researchbriefs/Summertime-extreme-precipitation/Summertime-extreme-precipitation.pdf

Computational And Information Systems Laboratory. (2016). *Yellowstone: IBM iDataPlex system (university community computing)*. National Center for Atmospheric Research, Boulder, CO. http://n2t.net/ark:/85065/d7wd3xhc

Computational And Information Systems Laboratory. (2017). *Cheyenne: HPE/SGI ICE XA system (university community computing)*. National Center for Atmospheric Research, Boulder, CO. https://doi.org/10.5065/D6RX99HX

Copernicus Climate Change Service. (2017). *Fifth generation of ecmwf atmospheric reanalyses of the global climate*. Copernicus Climate Change Service Climate Data Store (CDS). Retrieved January 28, 2020, from https://cds.climate.copernicus.eu/cdsapp#!/home

Daly, C., Halbleib, M., Smith, J. I., Gibson, W. P., Doggett, M. K., Taylor, G. H., Curtis, J., & Pasteris, P. P. (2008). Physiographically sensitive mapping of climatological temperature and precipitation across the conterminous united states. *International Journal of Climatology*, *28*(15), 2031–2064. https://doi.org/10.1002/joc.1688

Daly, C., Neilson, R. P., & Phillips, D. L. (1994). A statistical-topographic model for mapping climatological precipitation over mountainous terrain. *Journal of Applied Meteorology*, *33*(2), 140–158. https://doi.org/10.1175/1520-0450(1994)033<0140:ASTMFM>2.0.CO;2

Davini, P., & D'Andrea, F. (2016). Northern hemisphere atmospheric blocking representation in global climate models: Twenty years of improvements? *Journal of Climate*, *29*(24), 8823–8840. https://doi.org/10.1175/JCLI-D-16-0242.1

Davis, N., Hahmann, A. N., Clausen, N.-E., & Žagar, M. (2013). Forecast of icing events at a wind farm in sweden. *Journal of Applied Meteorology and Climatology*, *53*(2), 262–281. https://doi.org/10.1175/JAMC-D-13-09.1

Dee, D. P., Uppala, S. M., Simmons, A. J., Berrisford, P., Poli, P., Kobayashi, S., Andrae, U., Balmaseda, M. A., Balsamo, G., Bauer, P., Bechtold, P., Beljaars, A. C. M., van de Berg, L., Bidlot, J., Bormann, N., Delsol, C., Dragani, R., Fuentes, M., Geer, A. J., ... Vitart, F. (2011). The ERA-interim reanalysis: Configuration and performance of the data assimilation system. *Quarterly Journal of the Royal Meteorological Society*, *137*(656), 553–597. https://doi.org/10.1002/qj.828

DeGaetano, A. T., Belcher, B. N., & Spier, P. L. (2008). Short-term ice accretion forecasts for electric utilities using the weather research and forecasting model and a modified precipitation-type algorithm. *Weather and Forecasting*, *23*(5), 838–853. https://doi.org/10.1175/2008WAF2006106.1

Ding, Q., Wallace, J. M., Battisti, D. S., Steig, E. J., Gallant, A. J. E., Kim, H.-J., & Geng, L. (2014). Tropical forcing of the recent rapid arctic warming in northeastern canada and greenland. *Nature*, *509*(7499), 209–212. https://doi.org/10.1038/nature13260

Dolan, R., & Davis, R. E. (1992). An intensity scale for atlantic coast northeast storms. *Journal of Coastal Research*, *8*(4), 840–853.

Doswell, C. A., Brooks, H. E., & Kay, M. P. (2005). Climatological estimates of daily local nontornadic severe thunderstorm probability for the united states. *Weather and Forecasting*, *20*(4), 577–595. https://doi.org/10.1175/WAF866.1

Dowdy, A. J., & Catto, J. L. (2017). Extreme weather caused by concurrent cyclone, front and thunderstorm occurrences. *Scientific Reports*, *7*, 40359. https://doi.org/10.1038/srep40359

Easterling, D., Arnold, J., Knutson, T., Kunkel, K., LeGrande, A., Leung, L., Vose, R., Waliser, D., & Wehner, M. (2017). *Ch. 7: Precipitation change in the united states. climate science special report: Fourth national climate assessment, volume i*. U.S. Global Change Research Program. https://doi.org/10.7930/J0H993CC

ECMWF. (2009). *ERA-interim project* [Accessed August 1, 2017]. Research Data Archive at the National Center for Atmospheric Research, Computational and Information Systems Laboratory, Boulder, CO. https://doi.org/10.5065/D6CR5RD9

ECMWF. (2011). *The era-interim reanalysis dataset*. Copernicus Climate Change Service (C3S). Retrieved January 28, 2020, from https://www.ecmwf.int/en/forecasts/datasets/archive-datasets/reanalysis-datasets/era-interim

ECMWF. (2017). *ERA5 reanalysis* [Accessed March 27, 2019]. Research Data Archive at the National Center for Atmospheric Research, Computational and Information Systems Laboratory, Boulder, CO. https://doi.org/10.5065/D6X34W69

ECMWF. (2019). *ERA5 reanalysis (0.25 degree latitude-longitude grid)* [Accessed June 23, 2020]. Research Data Archive at the National Center for Atmospheric Research, Computational and Information Systems Laboratory, Boulder, CO. https://doi.org/10.5065/BH6N-5N20

Enfield, D. B., Mestas-Nuñez, A. M., & Trimble, P. J. (2001). The atlantic multidecadal oscillation and its relation to rainfall and river flows in the continental u.s. *Geophysical Research Letters*, *28*(10), 2077–2080. https://doi.org/10.1029/2000GL012745

Fang, Z.-F. (2004). Statistical relationship between the northern hemisphere sea ice and atmospheric circulation during wintertime, In *Observation, theory and modeling of atmospheric variability*. World Scientific. https://doi.org/10.1142/9789812791139_0006

Fernandez, I., Birkel, S., Schmitt, C., Simonson, J., Lyon, B., Pershing, A., Stancioff, E., Jacobson, G., & Mayewski, P. (2020). *Maine's climate future 2020 update*. Climate Change Institute, University of Maine. Orono, ME. https://climatechange.umaine.edu/climate-matters/maines-climate-future/

Folland, C. K., Knight, J., Linderholm, H. W., Fereday, D., Ineson, S., & Hurrell, J. W. (2009). The summer north atlantic oscillation: Past, present, and future. *Journal of Climate*, *22*(5), 1082–1103. https://doi.org/10.1175/2008JCLI2459.1

Forbes, G. S., Thomson, D. W., & Anthes, R. A. (1987). Synoptic and mesoscale aspects of an appalachian ice storm associated with cold-air damming. *Monthly Weather Review*, *115*(2), 564–591. https://doi.org/10.1175/1520-0493(1987)115<0564:SAMAOA>2.0.CO;2

Francis, J. A., & Vavrus, S. J. (2012). Evidence linking arctic amplification to extreme weather in mid-latitudes. *Geophysical Research Letters*, *39*(6). https://doi.org/10.1029/2012GL051000

Francis, J. A., & Vavrus, S. J. (2015). Evidence for a wavier jet stream in response to rapid arctic warming. *Environmental Research Letters*, *10*(1), 014005. https://doi.org/10.1088/1748-9326/10/1/014005

Frei, A., Kunkel, K. E., & Matonse, A. (2015). The seasonal nature of extreme hydrological events in the northeastern united states. *Journal of Hydrometeorology*, *16*(5), 2065–2085. https://doi.org/10.1175/JHM-D-14-0237.1

Galarneau, T. J., Davis, C. A., & Shapiro, M. A. (2013). Intensification of hurricane sandy (2012) through extratropical warm core seclusion. *Monthly Weather Review*, *141*(12), 4296–4321. https://doi.org/10.1175/MWR-D-13-00181.1

Gardiner, B., Peltola, H., & Kellomäki, S. (2000). Comparison of two models for predicting the critical wind speeds required to damage coniferous trees. *Ecological Modelling*, *129*(1), 1–23. https://doi.org/10.1016/S0304-3800(00)00220-9

Gilbert, R. O. (1987). *Statistical methods for environmental pollution monitoring*. New York, Van Nostran Reinhold.

Girardin, M.-P., Tardif, J. C., Flannigan, M. D., & Bergeron, Y. (2006). Synoptic-scale atmospheric circulation and boreal canada summer drought variability of the past three centuries. *Journal of Climate*, *19*(10), 1922–1947. https://doi.org/10.1175/JCLI3716.1

Goldenberg, S. B., Landsea, C. W., Mestas-Nuñez, A. M., & Gray, W. M. (2001). The recent increase in atlantic hurricane activity: Causes and implications. *Science*, *293*(5529), 474–479. https://doi.org/10.1126/science.1060040

Graham, G. (2017). Raging winds, rain leave 484,000 customers without power. *Portland Press Herald*, A1.

Griffiths, M. L., & Bradley, R. S. (2007). Variations of twentieth-century temperature and precipitation extreme indicators in the northeast united states. *Journal of Climate*, *20*(21), 5401–5417. https://doi.org/10.1175/2007JCLI1594.1

Gyakum, J. R., & Roebber, P. J. (2001). The 1998 ice storm—analysis of a planetary-scale event. *Monthly Weather Review*, *129*(12), 2983–2997. https://doi.org/10.1175/1520-0493(2001)129<2983:TISAOA>2.0.CO;2

Hanna, E., Cropper, T. E., Hall, R. J., & Cappelen, J. (2016). Greenland blocking index 1851-2015: A regional climate change signal. *International Journal of Climatology*, *36*(15), 4847–4861. https://doi.org/10.1002/joc.4673

Hanna, E., Cropper, T. E., Jones, P. D., Scaife, A. A., & Allan, R. (2015). Recent seasonal asymmetric changes in the NAO (a marked summer decline and increased winter variability) and associated changes in the AO and greenland blocking index. *International Journal of Climatology*, *35*(9), 2540–2554. https://doi.org/10.1002/joc.4157

Hanna, E., Fettweis, X., & Hall, R. J. (2018a). Brief communication: Recent changes in summer greenland blocking captured by none of the CMIP5 models. *The Cryosphere*, *12*(10), 3287–3292. https://doi.org/10.5194/tc-12-3287-2018

Hanna, E., Fettweis, X., Mernild, S. H., Cappelen, J., Ribergaard, M. H., Shuman, C. A., Steffen, K., Wood, L., & Mote, T. L. (2014). Atmospheric and oceanic climate forcing of the exceptional greenland ice sheet surface melt in summer 2012. *International Journal of Climatology*, *34*(4), 1022–1037. https://doi.org/10.1002/joc.3743

Hanna, E., Hall, R. J., Cropper, T. E., Ballinger, T. J., Wake, L., Mote, T., & Cappelen, J. (2018b). Greenland blocking index daily series 1851-2015: Analysis of changes in extremes and links with north atlantic and UK climate variability and change. *International Journal of Climatology*, *38*(9), 3546–3564. https://doi.org/10.1002/joc.5516

Hanna, E., Jones, J. M., Cappelen, J., Mernild, S. H., Wood, L., Steffen, K., & Huybrechts, P. (2013). The influence of north atlantic atmospheric and oceanic forcing effects on 1900-2010 greenland summer climate and ice melt/runoff. *International Journal of Climatology*, *33*(4), 862–880. https://doi.org/10.1002/joc.3475

Hart, R. E., & Evans, J. L. (2001). A climatology of the extratropical transition of atlantic tropical cyclones. *Journal of Climate*, *14*(4), 546–564. https://doi.org/10.1175/1520-0442(2001)014<0546:ACOTET>2.0.CO;2

Hersbach, H., Bell, B., Berrisford, P., Hirahara, S., Horányi, A., Muñoz-Sabater, J., Nicolas, J., Peubey, C., Radu, R., Schepers, D., Simmons, A., Soci, C., Abdalla, S., Abellan, X., Balsamo, G., Bechtold, P., Biavati, G., Bidlot, J., Bonavita, M., ... Thépaut, J. (2020). The ERA5 global reanalysis. *Quarterly Journal of the Royal Meteorological Society*, qj.3803. https://doi.org/10.1002/qj.3803

Hoerling, M., Eischeid, J., Perlwitz, J., Quan, X.-W., Wolter, K., & Cheng, L. (2016). Characterizing recent trends in u.s. heavy precipitation. *Journal of Climate*, *29*(7), 2313–2332. https://doi.org/10.1175/JCLI-D-15-0441.1

Hong, S.-Y., & Lim, J.-O. (2006). The WRF single-moment 6-class microphysics scheme (WSM6). *Journal of the Korean Meteorological Society*, *42*, 129–151.

Hosek, J., Musilek, P., Lozowski, E., & Pytlak, P. (2011). Forecasting severe ice storms using numerical weather prediction: The march 2010 newfoundland event. *Natural Hazards and Earth System Science*, *11*(2), 587–595. https://doi.org/10.5194/nhess-11-587-2011

Howarth, M. E., Thorncroft, C. D., & Bosart, L. F. (2019). Changes in extreme precipitation in the northeast united states: 1979–2014. *Journal of Hydrometeorology*, *20*(4), 673–689. https://doi.org/10.1175/JHM-D-18-0155.1

Huang, H., Winter, J. M., & Osterberg, E. C. (2018). Mechanisms of abrupt extreme precipitation change over the northeastern united states. *Journal of Geophysical Research: Atmospheres*, *123*(14), 7179–7192. https://doi.org/10.1029/2017JD028136

Huang, H., Winter, J. M., Osterberg, E. C., Horton, R. M., & Beckage, B. (2017). Total and extreme precipitation changes over the northeastern united states. *Journal of Hydrometeorology*, *18*(6), 1783–1798. https://doi.org/10.1175/JHM-D-16-0195.1

Hurrell, J., Trenberth, K., & National Center for Atmospheric Research Staff. (2020). *The climate data guide: Ncar sea level pressure*. National Center for Atmospheric Research. Retrieved June 5, 2020, from https://climatedataguide.ucar.edu/climate-data/ncar-sea-level-pressure

Iacono, M. J., Delamere, J. S., Mlawer, E. J., Shephard, M. W., Clough, S. A., & Collins, W. D. (2008). Radiative forcing by long-lived greenhouse gases: Calculations with the AER radiative transfer models. *Journal of Geophysical Research*, *113*. https://doi.org/10.1029/2008JD009944

Ikeda, K., Steiner, M., Pinto, J., & Alexander, C. (2013). Evaluation of cold-season precipitation forecasts generated by the hourly updating high-resolution rapid refresh model. *Weather and Forecasting*, *28*(4), 921–939. https://doi.org/10.1175/WAF-D-12-00085.1

Ikeda, K., Steiner, M., & Thompson, G. (2017). Examination of mixed-phase precipitation forecasts from the high-resolution rapid refresh model using surface observations and sounding data. *Weather and Forecasting*, *32*(3), 949–967. https://doi.org/10.1175/WAF-D-16-0171.1

Janić, Z. I. (2001). Nonsingular implementation of the mellor-yamada level 2.5 scheme in the NCEP meso model. *NCEP Office Note*, *436*. https://repository.library.noaa.gov/view/noaa/11409

Jiang, J., & Perrie, W. (2007). The impacts of climate change on autumn north atlantic midlatitude cyclones. *Journal of Climate*, *20*(7), 1174–1187. https://doi.org/10.1175/JCLI4058.1

Jiménez, P. A., Dudhia, J., González-Rouco, J. F., Navarro, J., Montávez, J. P., & García-Bustamante, E. (2011). A revised scheme for the WRF surface layer formulation. *Monthly Weather Review*, *140*(3), 898–918. https://doi.org/10.1175/MWR-D-11-00056.1

Jung, C., & Lackmann, G. M. (2019). Extratropical transition of hurricane irene (2011) in a changing climate. *Journal of Climate*, *32*(15), 4847–4871. https://doi.org/10.1175/JCLI-D-18-0558.1

Kain, J. S. (2004). The kain–fritsch convective parameterization: An update. *Journal of Applied Meteorology*, *43*(1), 170–181. https://doi.org/10.1175/1520-0450(2004)043<0170:TKCPAU>2.0.CO;2

Kalnay, E., Kanamitsu, M., Kistler, R., Collins, W., Deaven, D., Gandin, L., Iredell, M., Saha, S., White, G., Woollen, J., Zhu, Y., Chelliah, M., Ebisuzaki, W., Higgins, W., Janowiak, J., Mo, K. C., Ropelewski, C., Wang, J., Leetmaa, A., … Joseph, D. (1996). The NCEP/NCAR 40-year reanalysis project. *Bulletin of the American Meteorological Society*, *77*(3), 437–472. https://doi.org/10.1175/1520-0477(1996)077<0437:TNYRP>2.0.CO;2

Karmalkar, A. V., Thibeault, J. M., Bryan, A. M., & Seth, A. (2019). Identifying credible and diverse GCMs for regional climate change studies—case study: Northeastern united states. *Climatic Change*, *154*(3), 367–386. https://doi.org/10.1007/s10584-019-02411-y

Kendall, M. G. (1948). *Rank correlation methods.* Charles Griffin & Co. Ltd., London.

Klein, W. H. (1952). The weather and circulation of june 1952: A month with a record heat wave. *Monthly Weather Review*, *80*(6), 99–104.

Kunkel, K. E., Easterling, D. R., Kristovich, D. A. R., Gleason, B., Stoecker, L., & Smith, R. (2012). Meteorological causes of the secular variations in observed extreme precipitation events for the conterminous united states. *Journal of Hydrometeorology*, *13*(3), 1131–1141. https://doi.org/10.1175/JHM-D-11-0108.1

Kunkel, K. E., Karl, T. R., Brooks, H., Kossin, J., Lawrimore, J. H., Arndt, D., Bosart, L., Changnon, D., Cutter, S. L., Doesken, N., Emanuel, K., Groisman, P. Y., Katz, R. W., Knutson, T., O'Brien, J., Paciorek, C. J., Peterson, T. C., Redmond, K., Robinson, D., ... Wuebbles, D. (2013a). Monitoring and understanding trends in extreme storms: State of knowledge. *Bulletin of the American Meteorological Society*, *94*(4), 499–514. https://doi.org/10.1175/BAMS-D-11-00262.1

Kunkel, K. E., Stevens, L. E., Stevens, S. E., Sun, L., Janssen, E., Wuebbles, D., Rennells, J., DeGaetano, A., & Dobson, J. G. (2013b). *Regional climate trends and scenarios for the u.s. national climate assessment: Part 1. climate of the northeast u.s.* NOAA Technical Report 143-1. https://www.nesdis.noaa.gov/sites/default/files/asset/document/NOAA_NESDIS_Tech_Report_142-1-Climate_of_the_Northeast_US.pdf

Lacke, M. C., Knox, J. A., Frye, J. D., Stewart, A. E., Durkee, J. D., Fuhrmann, C. M., & Dillingham, S. M. (2007). A climatology of cold-season nonconvective wind events in the great lakes region. *Journal of Climate*, *20*(24), 6012–6022. https://doi.org/10.1175/2007JCLI1750.1

Landsea, C. W., & Franklin, J. L. (2013). Atlantic hurricane database uncertainty and presentation of a new database format. *Monthly Weather Review*, *141*(10), 3576–3592. https://doi.org/10.1175/MWR-D-12-00254.1

Landsea, C. W., Pielke, R. A., Mestas-Nuñez, A. M., & Knaff, J. A. (1999). Atlantic basin hurricanes: Indices of climatic changes. *Climatic Change*, *42*(1), 89–129. https://doi.org/10.1023/A:1005416332322

Leathers, D., Grundstein, A., & Ellis, A. (2000). Growing season moisture deficits across the northeastern united states. *Climate Research*, *14*, 43–55. https://doi.org/10.3354/cr014043

Li, G., Zhang, P., Luh, P. B., Li, W., Bie, Z., Serna, C., & Zhao, Z. (2014). Risk analysis for distribution systems in the northeast u.s. under wind storms. *IEEE Transactions on Power Systems*, *29*(2), 889–898. https://doi.org/10.1109/TPWRS.2013.2286171

Liu, M., Vecchi, G. A., Smith, J. A., & Murakami, H. (2017). The present-day simulation and twenty-first-century projection of the climatology of extratropical transition in the north atlantic. *Journal of Climate*, *30*(8), 2739–2756. https://doi.org/10.1175/JCLI-D-16-0352.1

Lott, N., & Ross, T. (2006). Tracking and evaluating u.s. billion dollar weather disasters, 1980-2005. AMS Forum: Environmental Risk and Impacts on Society: Successes and Challenges, Atlanta, GA, Amer. Meteor. Soc. http://ams.confex.com/ams/pdfpapers/100686.pdf

Lynch, C., Seth, A., & Thibeault, J. (2016). Recent and projected annual cycles of temperature and precipitation in the northeast united states from CMIP5. *Journal of Climate*, *29*(1), 347–365. https://doi.org/10.1175/JCLI-D-14-00781.1

Mann, H. B. (1945). Nonparametric tests against trend. *Econometrica*, *13*(3), 245–259. https://doi.org/10.2307/1907187

Marks, P. L., Gardescu, S., & Hitzhusen, G. E. (1999). Windstorm damage and age structure in an old growth forest in central new york. *Northeastern Naturalist*, *6*(2), 165–176. https://doi.org/10.2307/3858347

McNally, L. K., Maasch, K. A., & Zuill, K. A. (2008). The use of ships' protests for reconstruction of synoptic-scale weather and tropical storm identification in the late eighteenth century. *Weather*, *63*(7), 208. https://doi.org/10.1002/wea.272

Mesinger, F., DiMego, G., Kalnay, E., Mitchell, K., Shafran, P. C., Ebisuzaki, W., Jović, D., Woollen, J., Rogers, E., Berbery, E. H., Ek, M. B., Fan, Y., Grumbine, R., Higgins, W., Li, H., Lin, Y., Manikin, G., Parrish, D., & Shi, W. (2006). North american regional reanalysis. *Bulletin of the American Meteorological Society*, *87*(3), 343–360. https://doi.org/10.1175/BAMS-87-3-343

Michaelis, A. C., & Lackmann, G. M. (2019). Climatological changes in the extratropical transition of tropical cyclones in high-resolution global simulations. *Journal of Climate*, *32*(24), 8733–8753. https://doi.org/10.1175/JCLI-D-19-0259.1

Mullens, E. D., Leslie, L. M., & Lamb, P. J. (2016). Impacts of gulf of mexico SST anomalies on southern plains freezing precipitation: ARW sensitivity study of the 28–30 january 2010 winter storm. *Journal of Applied Meteorology and Climatology*, *55*(1), 119–143. https://doi.org/10.1175/JAMC-D-14-0289.1

Musilek, P., Arnold, D., & Lozowski, E. P. (2009). An ice accretion forecasting system (IAFS) for power transmission lines using numerical weather prediction. *SOLA*, *5*, 25–28. https://doi.org/10.2151/sola.2009-007

Namias, J. (1966). Nature and possible causes of the northeastern united states drought during 1962-65. *Monthly Weather Review*, *94*(9), 543–554.

Namias, J. (1983). Some causes of united states drought. *Journal of Climate and Applied Meteorology*, *22*(1), 30–39. https://doi.org/10.1175/1520-0450(1983)022<0030:SCOUSD>2.0.CO;2

NCAR. (2017). *The NCAR command language* [Version 6.4.0]. UCAR/NCAR/CISL/TDD, Boulder, CO. https://doi.org/10.5065/D6WD3XH5

NCAR. (2019). *The NCAR command language* [Version 6.6.2]. UCAR/NCAR/CISL/TDD, Boulder, CO. https://doi.org/10.5065/D6WD3XH5

NCAR. (2020). *The climate data guide: Hurrell north atlantic oscillation (nao) index (pc-based)*. National Center for Atmospheric Research. Retrieved January 29, 2020, from https://climatedataguide.ucar.edu/climate-data/hurrell-north-atlantic-oscillation-nao-index-pc-based

NCDC. (2014). Storm data and unusual weather. *Storm Data*, *55*(12).

NCEP. (2005). *Ncep north american regional reanalysis (narr)*. Research Data Archive at the National Center for Atmospheric Research, Computational and Information Systems Laboratory, Boulder, CO. Retrieved March 27, 2019, from http://rda.ucar.edu/datasets/ds608.0/

Niziol, T. A., & Paone, T. J. (2000). *A climatology of non-convective high wind events in western new york state*. NOAA Tech. Memo. NWS ER-91. https://repository.library.noaa.gov/view/noaa/6402

NOAA. (2018). *Wpc's surface analysis archive*. Weather Prediction Center. Retrieved January 24, 2018, from http://www.wpc.ncep.noaa.gov/archives/web_pages/sfc/sfc_archive.php

NOAA. (2019a). *Spc hourly mesoscal analysis*. Storm Prediction Center. Retrieved May 16, 2019, from http://www.spc.noaa.gov/exper/ma_archive/

NOAA. (2019b). *Storm total maps*. National Weather Service, Caribou, ME. Retrieved March 27, 2019, from https://www.weather.gov/car/StormTotalMaps

NOAA/NCEI. (2014). *State of the climate: National climate report for december 2013*. National Centers for Environmental Information. Retrieved July 5, 2018, from https://www.ncdc.noaa.gov/sotc/national/201312

NOAA/NCEI. (2017). *State of the climate: National climate report for october 2017*. National Centers for Environmental Information. Retrieved March 17, 2020, from https://www.ncdc.noaa.gov/sotc/national/201710

NOAA/NCEI. (2019a). *National digital guidance database: Real-time mesoscale analysis*. National Centers for Environmental Information. Retrieved August 12, 2019, from https://www.ncdc.noaa.gov/data-access/model-data/model-datasets/national-digital-guidance-database-ndgd

NOAA/NCEI. (2019b). *Ncep/ncar reanalysis 1*. National Centers for Environmental Information. Retrieved December 2, 2019, from https://psl.noaa.gov/data/gridded/data.ncep.reanalysis.html

NOAA/NCEI. (2020). *Climate at a glance: National time series*. National Centers for Environmental Information. Retrieved April 14, 2020, from https://www.ncdc.noaa.gov/cag/

Nygaard, B. E. K., Kristjánsson, J. E., & Makkonen, L. (2011). Prediction of in-cloud icing conditions at ground level using the WRF model. *Journal of Applied Meteorology and Climatology*, *50*(12), 2445–2459. https://doi.org/10.1175/JAMC-D-11-054.1

Overland, J. E., Hanna, E., Hanssen-Bauer, I., Kim, S.-J., Walsh, J. E., Wang, M., Bhatt, U., & Thoman, R. (2017). Surface air temperature (J. Richter-Menge, J. E. Overland, J. T. Mathis, & E. Osborne, Eds.). *Arctic Report Card 2017*. https://arctic.noaa.gov/Report-Card/Report-Card-2017

Overland, J. E., Hanna, E., Hanssen-Bauer, I., Kim, S.-J., Walsh, J. E., Wang, M., Bhatt, U., Thoman, R., & Ballinger, T. J. (2019). Surface air temperature (J. Richter-Menge, M. L. Druckenmiller, & M. Jeffries, Eds.). *Arctic Report Card 2019*. https://arctic.noaa.gov/Report-Card/Report-Card-2019

Overland, J. E., Francis, J. A., Hall, R. J., Hanna, E., Kim, S.-J., & Vihma, T. (2015). The melting arctic and midlatitude weather patterns: Are they connected? *Journal of Climate*, *28*(20), 7917–7932. https://doi.org/10.1175/JCLI-D-14-00822.1

Overland, J. E., Francis, J. A., Hanna, E., & Wang, M. (2012). The recent shift in early summer arctic atmospheric circulation. *Geophysical Research Letters*, *39*(19). https://doi.org/10.1029/2012GL053268

Overland, J. E., & Wang, M. (2010). Large-scale atmospheric circulation changes are associated with the recent loss of arctic sea ice. *Tellus A: Dynamic Meteorology and Oceanography*, *62*(1), 1–9. https://doi.org/10.1111/j.1600-0870.2009.00421.x

Peltola, H, Kellomäki, S, Väisänen, H, & Ikonen, V. P. (1999). A mechanistic model for assessing the risk of wind and snow damage to single trees and stands of scots pine, norway spruce, and birch. *Canadian Journal of Forest Research*, *29*(6), 647–661. https://doi.org/10.1139/x99-029

Pytlak, P., Musilek, P., Lozowski, E., & Arnold, D. (2010). Evolutionary optimization of an ice accretion forecasting system. *Monthly Weather Review*, *138*(7), 2913–2929. https://doi.org/10.1175/2010MWR3130.1

Pytlak, P. M. (2012). *Intelligent methods for evaluating the impact of weather on power transmission infrastructure* (Ph.D. Thesis). University of Alberta. Edmonton, Alberta. https://era.library.ualberta.ca/items/92bdf897-dc03-43c4-9435-a0a9c7753a02

Rawlins, M. A., Bradley, R. S., & Diaz, H. F. (2012). Assessment of regional climate model simulation estimates over the northeast united states. *Journal of Geophysical Research: Atmospheres*, *117*. https://doi.org/10.1029/2012JD018137

Reeves, H. D., Elmore, K. L., Ryzhkov, A., Schuur, T., & Krause, J. (2014). Sources of uncertainty in precipitation-type forecasting. *Weather and Forecasting*, *29*(4), 936–953. https://doi.org/10.1175/WAF-D-14-00007.1

Roebber, P. J. (1989). On the statistical analysis of cyclone deepening rates. *Monthly Weather Review*, *117*(10), 2293–2298. https://doi.org/10.1175/1520-0493(1989)117<2293:OTSAOC>2.0.CO;2

Roebber, P. J., & Gyakum, J. R. (2003). Orographic influences on the mesoscale structure of the 1998 ice storm. *Monthly Weather Review*, *131*(1), 27–50. https://doi.org/10.1175/1520-0493(2003)131<0027:OIOTMS>2.0.CO;2

Romanić, D., Ćurić, M., Jovičić, I., & Lompar, M. (2015). Long-term trends of the 'koshava' wind during the period 1949–2010. *International Journal of Climatology*, *35*(2), 288–302. https://doi.org/10.1002/joc.3981

Rowley, N. A., Carleton, A. M., & Fegyveresi, J. (2020). Relationships of west greenland supraglacial melt-lakes with local climate and regional atmospheric circulation. *International Journal of Climatology*, *40*(2), 1164–1177. https://doi.org/10.1002/joc.6262

Russell, E. (2018). CMP says october windstorm cost it $69 million, and customers will help pay the cost. *Portland Press Herald*. Retrieved March 17, 2020, from https://www.pressherald.com/2018/01/18/unprecedented-october-storm-cost-central-maine-power-69-million/

Samenow, J. (2017). More than 1 million power outages in the northeast after blockbuster fall storm. *Washington Post*. Retrieved March 17, 2020, from https://www.washingtonpost.com/news/capital-weather-gang/wp/2017/10/30/over-one-million-power-outages-in-the-northeast-after-blockbuster-fall-storm/

Sanders, F., & Gyakum, J. R. (1980). Synoptic-dynamic climatology of the "bomb". *Monthly Weather Review*, *108*(10), 1589–1606. https://doi.org/10.1175/1520-0493(1980)108<1589:SDCOT>2.0.CO;2

Scorer, R. S. (1988). Sunny greenland. *Quarterly Journal of the Royal Meteorological Society*, *114*(479), 3–29. https://doi.org/10.1002/qj.49711447902

Screen, J. A. (2013). Influence of arctic sea ice on european summer precipitation. *Environmental Research Letters*, *8*(4), 044015. https://doi.org/10.1088/1748-9326/8/4/044015

Screen, J. A., & Simmonds, I. (2013). Exploring links between arctic amplification and mid-latitude weather. *Geophysical Research Letters*, *40*(5), 959–964. https://doi.org/10.1002/grl.50174

Screen, J. A., & Simmonds, I. (2014). Amplified mid-latitude planetary waves favour particular regional weather extremes. *Nature Climate Change*, *4*(8), 704–709. https://doi.org/10.1038/nclimate2271

Seager, R., Pederson, N., Kushnir, Y., Nakamura, J., & Jurburg, S. (2012). The 1960s drought and the subsequent shift to a wetter climate in the catskill mountains region of the new york city watershed*. *Journal of Climate*, *25*(19), 6721–6742. https://doi.org/10.1175/JCLI-D-11-00518.1

Sen, P. K. (1968). Estimates of the regression coefficient based on kendall's tau. *Journal of the American Statistical Association*, *63*(324), 1379–1389. https://doi.org/10.1080/01621459.1968.10480934

Skamarock, W., Klemp, J., Dudhia, J., Gill, D., Barker, D., Wang, W., Huang, X.-Y., Duda, M., & Powers, J. (2008). *A description of the advanced research WRF version 3* [(No. NCAR/TN-475+STR)]. University Corporation for Atmospheric Research. (No. NCAR/TN-475+STR). https://doi.org/10.5065/D68S4MVH

Smith, A., Lott, N., & Vose, R. (2011). The integrated surface database: Recent developments and partnerships. *Bulletin of the American Meteorological Society*, *92*(6), 704–708. https://doi.org/10.1175/2011BAMS3015.1

Stanglin, D. (2019). Almost 1 million lose power after intense halloween storm rolls through eastern US. *USA TODAY*. Retrieved March 17, 2020, from https://www.usatoday.com/story/news/nation/2019/11/01/power-outages-halloween-storm-maine-new-york-connecticut-vermont/4120890002/

Stauffer, D. R., & Seaman, N. L. (1994). Multiscale four-dimensional data assimilation. *Journal of Applied Meteorology*, *33*(3), 416–434. https://doi.org/10.1175/1520-0450(1994)033<0416:MFDDA>2.0.CO;2

Stewart, R. E., & King, P. (1987). Freezing precipitation in winter storms. *Monthly Weather Review*, *115*(7), 1270–1280. https://doi.org/10.1175/1520-0493(1987)115<1270:FPIWS>2.0.CO;2

Stroeve, J. C., Kattsov, V., Barrett, A., Serreze, M., Pavlova, T., Holland, M., & Meier, W. N. (2012a). Trends in arctic sea ice extent from CMIP5, CMIP3 and observations. *Geophysical Research Letters*, *39*(16). https://doi.org/10.1029/2012GL052676

Stroeve, J. C., Serreze, M. C., Holland, M. M., Kay, J. E., Malanik, J., & Barrett, A. P. (2012b). The arctic's rapidly shrinking sea ice cover: A research synthesis. *Climatic Change*, *110*(3), 1005–1027. https://doi.org/10.1007/s10584-011-0101-1

Sutton, R. T., & Dong, B. (2012). Atlantic ocean influence on a shift in european climate in the 1990s. *Nature Geoscience*, *5*(11), 788–792. https://doi.org/10.1038/ngeo1595

Tabari, H., Somee, B. S., & Zadeh, M. R. (2011). Testing for long-term trends in climatic variables in iran. *Atmospheric Research*, *100*(1), 132–140. https://doi.org/10.1016/j.atmosres.2011.01.005

Taber, B. (2015). *The major north country ice storm of december 2013* (The Four Seasons No. 2). NWS Burlington, VT. https://www.weather.gov/media/btv/Newsletter/Letter%20-%20The%20Four%20Seasons-%20WINTER%202014-2015.pdf

Taylor, K. E., Stouffer, R. J., & Meehl, G. A. (2012). An overview of CMIP5 and the experiment design. *Bulletin of the American Meteorological Society*, *93*(4), 485–498. https://doi.org/10.1175/BAMS-D-11-00094.1

Tedesco, M., & Fettweis, X. (2020). Unprecedented atmospheric conditions (1948-2019) drive the 2019 exceptional melting season over the greenland ice sheet. *The Cryosphere*, *14*(4), 1209–1223. https://doi.org/10.5194/tc-14-1209-2020

Tewari, M., Chen, F, Wang, W, Dudhia, J., LeMone, M., Mitchell, K., Ek, M, Gayno, G, Wegiel, J., Cuenca, R. Et al. (2004). Implementation and verification of the unified noah land surface model in the wrf model, In *20th conference on weather analysis and forecasting/16th conference on numerical weather prediction*. American Meteorological Society, Seattle, WA.

Theil, H. (1950). A rank-invariant method of linear and polynomial regression analysis, part 3. *Proceedings of Koninalijke Nederlandse Akademie van Weinenschatpen A*, *53*, 1397–1412.

Thibeault, J. M., & Seth, A. (2014). A framework for evaluating model credibility for warm-season precipitation in northeastern north america: A case study of CMIP5 simulations and projections. *Journal of Climate*, *27*(2), 493–510. https://doi.org/10.1175/JCLI-D-12-00846.1

Thibeault, J. M., & Seth, A. (2015). Toward the credibility of northeast united states summer precipitation projections in CMIP5 and NARCCAP simulations. *Journal of Geophysical Research: Atmospheres*, *120*(19), 10,050–10,073. https://doi.org/10.1002/2015JD023177

Thériault, J. M., Stewart, R. E., & Henson, W. (2010). On the dependence of winter precipitation types on temperature, precipitation rate, and associated features. *Journal of Applied Meteorology and Climatology*, *49*(7), 1429–1442. https://doi.org/10.1175/2010JAMC2321.1

UCAR. (2005). *Topics in precipitation type forecasting: Top-down method*. COMET MetED. Retrieved August 24, 2019, from https://www.meted.ucar.edu/norlat/snow/preciptype/preciptype_topdown.htm

Ulbrich, U., Leckebusch, G. C., & Pinto, J. G. (2009). Extra-tropical cyclones in the present and future climate: A review. *Theoretical and Applied Climatology*, *96*(1), 117–131. https://doi.org/10.1007/s00704-008-0083-8

Vavrus, S. J., Wang, F., Martin, J. E., Francis, J. A., Peings, Y., & Cattiaux, J. (2017). Changes in north american atmospheric circulation and extreme weather: Influence of arctic amplification and northern hemisphere snow cover. *Journal of Climate*, *30*(11), 4317–4333. https://doi.org/10.1175/JCLI-D-16-0762.1

Vollsinger, S., Mitchell, S. J., Byrne, K. E., Novak, M. D., & Rudnicki, M. (2005). Wind tunnel measurements of crown streamlining and drag relationships for several hardwood species. *Canadian Journal of Forest Research*, *35*(5), 1238–1249. https://doi.org/10.1139/x05-051

Vose, R. S., Applequist, S., Squires, M., Durre, I., Menne, M. J., Williams, C. N., Fenimore, C., Gleason, K., & Arndt, D. (2014). Improved historical temperature and precipitation time series for u.s. climate divisions. *Journal of Applied Meteorology and Climatology*, *53*(5), 1232–1251. https://doi.org/10.1175/JAMC-D-13-0248.1

Whittle, P. (2017). Drought fueled wind damage from storm that walloped maine, officials say. *Bangor Daily News*. Retrieved March 12, 2020, from https://bangordailynews.com/2017/11/01/outdoors/weather/drought-aided-wind-damage-from-storm-that-walloped-maine-officials-say/

Wilks, D. S. (2011). *Statistical methods in the atmospheric sciences* (3rd ed, Vol. 100). San Diego, CA, Academic Press.

Woollings, T., Hannachi, A., Hoskins, B., & Turner, A. (2010). A regime view of the north atlantic oscillation and its response to anthropogenic forcing. *Journal of Climate*, *23*(6), 1291–1307. https://doi.org/10.1175/2009JCLI3087.1

Woollings, T., Hoskins, B., Blackburn, M., & Berrisford, P. (2008). A new rossby wave–breaking interpretation of the north atlantic oscillation. *Journal of the Atmospheric Sciences*, *65*(2), 609–626. https://doi.org/10.1175/2007JAS2347.1

Young, W. R. (1978). *Freezing precipitation in the southeastern united states* (Master's Thesis). Texas A&M University. College Station, TX. http://hdl.handle.net/1969.1/ETD-TAMU-1978-THESIS-Y78

Zarnani, A., Musilek, P., Shi, X., Ke, X., He, H., & Greiner, R. (2012). Learning to predict ice accretion on electric power lines. *Engineering Applications of Artificial Intelligence*, *25*(3), 609–617. https://doi.org/10.1016/j.engappai.2011.11.004

Zerr, R. J. (1997). Freezing rain: An observational and theoretical study. *Journal of Applied Meteorology*, *36*(12), 1647–1661. https://doi.org/10.1175/1520-0450(1997)036<1647:FRAOAT>2.0.CO;2

BIOGRAPHY OF THE AUTHOR

Julia Simonson was born in Red Wing, Minnesota on December 19, 1991. She was raised in her hometown and graduated from Red Wing High School in 2010. She attended the University of North Dakota and graduated in 2014 with a Bachelor's degree in Atmospheric Sciences. She then attended the University of Nebraska-Lincoln and graduated in 2016 with a Master's degree in Earth and Atmospheric Sciences with a specialization in Meteorology/Climatology. She entered the Earth and Climate Sciences graduate program at the University of Maine in the fall of 2016.

Julia Simonson is a candidate for the Doctor of Philosophy degree in Earth and Climate Sciences from the University of Maine in August 2020.